Electronic properties and applications of Nanodiamond

Aysha Nasreen Chaudhary

This thesis is submitted for the degree Doctor of Philosophy.

Department of Electronic and Electrical Engineering
University College London
February 2012

Declaration

The work in this thesis is the result of research carried out at University College London, London Centre for Nanotechnology, Diamond Electronics Group. I declare it to be my own work unless referenced to the contrary in the text.

Acknowledgements

This thesis is dedicated to my parents, for all their efforts throughout my life and the emphasis they placed on our religion and the pursuit of knowledge. Thank you for everything you have done to help me reach this point, from ensuring my success throughout my school years to the home cooked meals I am still relying on today. To Abubakar, my husband and best friend, for his support and patience. To my siblings (Yaqub, Sajida, Ishaque, Ismaiel and Yusuf) for just being themselves, always keeping the mood light-hearted and asking me when I am going to finish my "puh-hud". My warm thoughts extend to Dr. "Aunty" Nusrat, who herself was on a scholarship from Pakistan to study for a PhD in Mathematics, when I was a young girl. As far as I can remember, following in your footsteps was my earliest ambition.

I would like to extend my deepest gratitude to my supervisor, Prof. Richard Jackman for giving me the opportunity not only to study for this PhD but for believing in my abilities when others would not have. Thank you for the lab based teaching sessions and ensuring results flowed forth! Not to mention the opportunities given to attend some great conferences and the general fun-times had. Thanks to Dr. Stephane Curat for supervising my undergraduate project, which lead me back to the UCL Diamond Electronics Group.

The past four years have been filled with ups and downs as is the nature of research work but the former far outweigh the latter, thanks to the dynamics of the DEG and all my wonderful colleagues, past and present. I would like to thank the 'old' Diamond Group, Dr. Niall Tumilty, Dr. Mose Bevilacqua and Dr. Rezal Ahmad, for all the interesting, amusing and candid lunch-time discussions. For lifting equipment and tightening nuts for me (thanks to Joe too)! Probably now forgotten, but we endured some difficult times together and made it out of the other end. A big thank you to the 'new' diamond group, Dr. Robert Edgington, Joseph Welch, Ana Carolina Parada and Fang Zhao; it has been great fun working together and here's to 'it' not ending too soon.

Special thanks to all the people whose assistance made the experimental work possible. Thank you to Dr. Steve Hudziak for helping to obtain countless AFM images of nanodiamond particles in all their glory. Most of the images did not make the final cut but we know only too well how many there were. Thank you to Mark Turmain and Dr. Steve Firth with their help in obtaining the SEM images and Raman spectra presented throughout this thesis. Thank you to Dr. Oliver Williams for his advice and assistance on all things nanodiamond.

My sincere thanks and gratitude go to Gert Nutzel and Pascal Lavoute, our collaborators from Photonis SAS. France, for the project conception, financial support and intellectual input from which the last few chapters of this thesis were born.

Abstract

Detonation nanodiamonds were first produced by shock wave synthesis in the 1960's. In recent years advances in the processing and purification of detonation nanodiamond has renewed interest into their research, from the basic properties of detonation nanodiamonds to their applications in areas from electronics to biology. Using a colloid of mono dispersed detonation nanodiamonds, it is possible to coat various substrate materials. Diamond possess negative electron affinity as well as excellent thermal conductivity and chemical stability. It this therefore an attractive material for applications such as electron multipliers by secondary electron emission with high yields. This thesis reports on the suitability and enhancement of nanodiamond coatings for such applications. Atomic force microscopy is used to investigate the deposition of nanodiamond particles on the substrate material. The electrical characteristics of mono-dispersed nanodiamond layers are investigated using impedance spectroscopy, establishing that the layers have high quality dielectric characteristics. Hydrogen terminated CVD diamond is known to have a negative electron affinity (NEA), making it a suitable material for secondary electron emission. This thesis investigates using and optimising nanodiamond coatings on micro channel plates (MCPs) to increase the secondary electron yield of these devices, thereby improving the performance of image intensifiers. The as-received nanodiamond is covered with surface functional groups dependent on post detonation treatments for cleaning and deaggregation. Treatments have been designed which modify the surface groups for homogeneity, followed by an oxidation treatment to provide a platform for metallisation, notably caesium oxide which is known to give a stable and high NEA surface thus further improving the secondary electron yield. Fourier transform infra-red spectroscopy and has been used to investigate the presence of functional groups. A comprehensive study of the secondary electron emission yield of nanodiamond coatings after various surface treatments is presented. The most effective treatment is found to be a low temperature chemical vapour deposition process which is compatible with the fragile MCP structure. SEM and Raman spectroscopy have been used to provide an insight into the changes of the material, which remains nanodiamond-like. These are the first such results from nanodiamond material.

Table of Contents

Chapter 1 Introduction

Natural diamonds, with their exceptional brilliance, have been treasured as gemstones for millennia. This allotrope of carbon has an array of remarkable properties making it suitable for extreme applications; eighty percent of mined diamonds are destined for industrial use. Diamond's hardness and thermal conductivity, the greatest of any bulk material, have leant themselves to diamond being widely used in industry for cutting and polishing tools. Diamond also has the lowest coefficient of thermal expansion, is chemically inert, has high thermal conductivity, is electrically insulating and optically transparent from the ultra-violet (UV) to the far infrared (IR).

It is therefore not surprising that there are many potential applications for diamond as an engineering material. The relative scarcity of natural diamond and other restrictions such as quality, reproducibility and functionality have lead to the synthetic diamond industry. The first commercially successful, reproducible synthesis of diamond was made in 1954 by a team at GE. This original process used HPTP (High Pressure High Temperature) in which diamond is crystallised from a metal solvated carbon at high pressure and high temperature. This so-called 'industrial diamond', widely used due to its low cost, has been synthesised commercially for over 30 years using HPHT techniques.

Research into diamond as a semiconductor material really started after the emergence of a second technique; chemical vapour deposition (CVD). Chemical vapour deposition is a method of growing diamond from a hydrocarbon gas mixture. Since the early 1980s, this method has been the subject of intensive worldwide research. Whereas the mass-production of high-quality diamond crystals make the HPHT process the more suitable choice for industrial applications, the flexibility and simplicity of CVD setups explain the popularity of CVD growth in laboratory research. The advantages of CVD diamond growth include the ability to grow diamond over large areas and on foreign substrates, and the fine control over the chemical impurities and thus properties of the diamond produced.

A third method, known as detonation synthesis, entered the diamond market in the late 1990s. Detonation nanodiamonds were first produced by shock wave synthesis performed in USSR in 1963. One of the critical problems with material produced by detonation synthesis is the tendency of the core particles to aggregate into larger agglomerates that are difficult to disperse in solution. The purification of nanodiamond particles is an active and complex research area which determines the applications of such particles. In recent years, advances in this area have renewed interest and allowed researchers to investigate the use of nanodiamonds in a diverse range of applications, such as biological cell attachment and growth,[1.1] carriers for in-vivo drug delivery,[1.2] fluorescent markers within biological systems,[1.3] additives to oil-based compounds for friction reduction[1.4] electrodes for electrochemistry,[1.5] and for cold-cathode fabrication through electron field-emission.[1.6] They are also of critical importance as seeds for the deposition of nanodiamond films.[1.7]

There is great interest in thin films of high quality diamond, with one of the reasons being cost. The growth of diamond using CVD or HPHT methods is still a relatively expensive process and any reduction of growth duration is a real cost saving measure. If the majority of the extreme properties of diamond or simply those that are required for a specific application can be exploited by a thin film, the expense and complexity of growing bulk diamond is unnecessary. There are also many applications where bulk diamond is inappropriate, such as micro electromechanical systems (MEM) and tribological coatings. This thesis investigates the use of nanodiamond coatings for electronic applications, from fundamental research into their electronic characteristics to the use of nanodiamond coatings on multichannel plates.

Chapter 2 reports on the growth, properties and electronic applications of synthetic diamond and the more recently pursued area of detonation nanodiamond research. This chapter focuses on the growth of diamond films using microwave plasma chemical vapour deposition. A review of the synthesis, processing and applications of nanodiamond particles is also presented. Chapter 3 presents the theory behind image intensifiers, specifically the microchannel plate

component. A review of diamond as a secondary electron emission material, with a view to its application in microchannel plates is presented. The experimental methods and techniques used in this thesis are explained in chapter 4.

Chapter 5 presents an investigation into the process of producing nanodiamond coatings. An important requirement for the various electronic applications of nanodiamonds is the ability to coat substrate materials with the required density of particles. The Raman spectrum of as-received nanodiamonds is also presented and discussed. In chapter 6, an impedance spectroscopy study of nanodiamond coatings is reported, yielding an insight into the electronic properties of such layers. Chapter 7 presents an investigation into the surface modifications of nanodiamond particles using various treatments. FTIR has proven to be a useful tool to analyse the presence of surface functional groups and is therefore the chosen analytical method.

Chapter 8 utilises the knowledge and results gained from the previous three chapters to investigate the secondary electron emission (SEE) yields of nanodiamond layers for their potential application as a coating for microchannel plates. This is the first study of its kind from nanodiamond layers. The chapter begins with an investigation into the SEE yield characteristics from nanodiamond layers with surface modifications using the methods described in chapter 7, to the results after low temperature CVD processing. SEM imaging and Raman spectroscopy are extensively employed to characterise the processed material.

References

1.1 A. Thalhammer, R. J. Edgington, L. A. Cingolani, R. Schoepfer, and R. B. Jackman*, Biomaterials*, 31, 2097 (2010).

1.2 K. V. Purtov, A. I. Petunin, A. E. Burov, A. P. Puzyr, and V. S. Bondar, *Nanoscale Research Letters*, 5, 631 (2010).

1.3 L. C. L. Huang and H. C. Chang*, Langmuir*, 20, 5879 (2004).

1.4 V. Yu. Dolmatov, *Journal of Superhard Materials,* 32, 14, (2010).

1.5 J. B. Zang, Y. H. Wang, S. Z. Zhao, L. Y. Bian, and J. Lu, *Diamond and Related Materials,* 16 16 (2007).

1.6 D. He, L. Shao, W. Gong, E. Xie, K. Xu, and G. Chen, *Diamond and Related Materials*, 9. 1600 (2000).

1.7 O.A. Williams, O. Douheret, M. Daenen, K. Haenen, E. Osawa, M. Takahashi, *Chemical Physics Letters*, 445 (4–6) 255 (2007).

Chapter 2 Diamond

2.1 Carbon

Carbon, denoted by the chemical symbol C, is one of the most abundant elements in the universe. It has an atomic number of 6. Carbon takes the form of several allotropes, shown in figure 2.1, with diamond and graphite being two of the most well known.

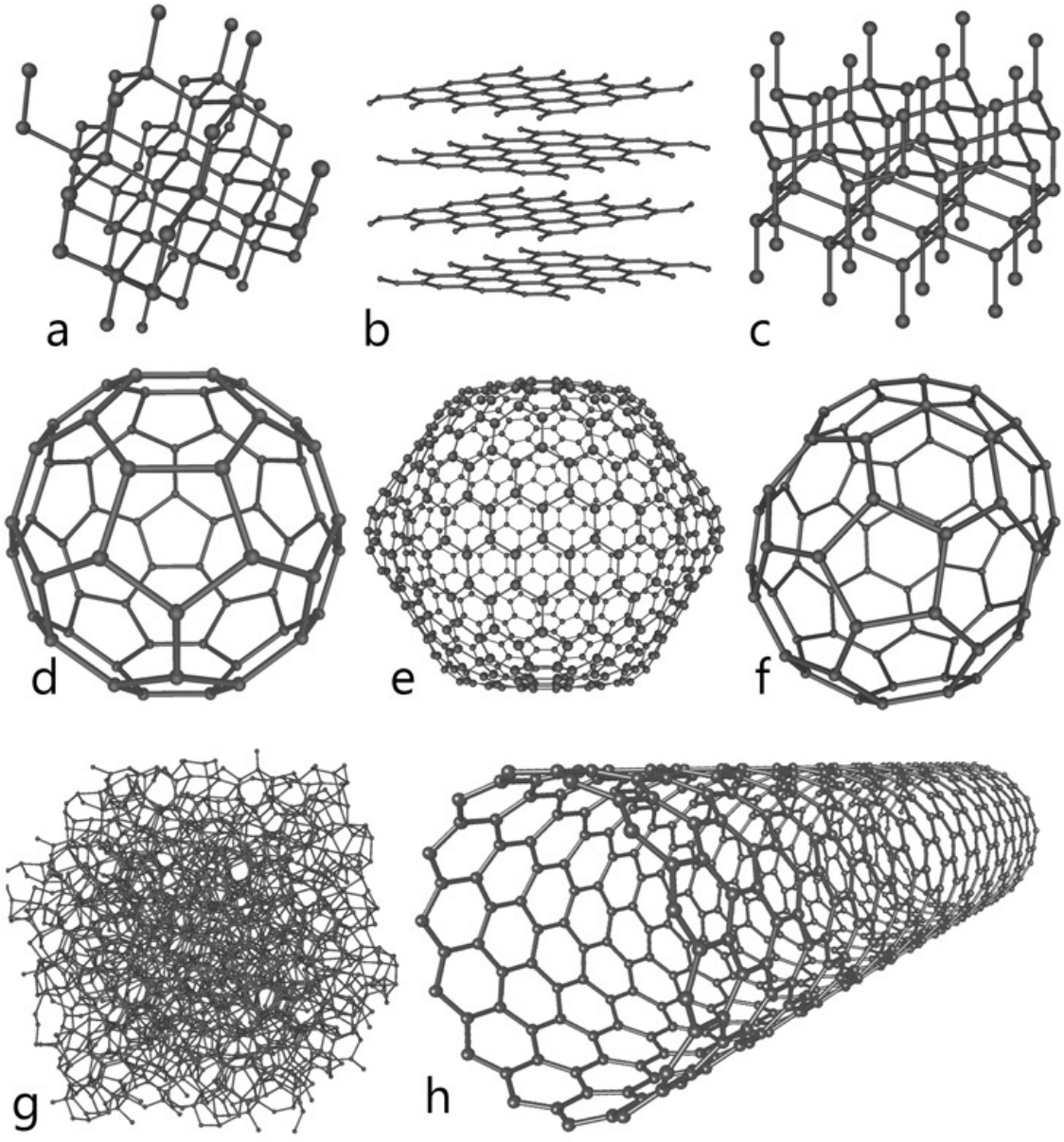

Figure 2.1: The structures of eight allotropes of carbon (a) diamond, (b) graphite, (c) lonsdaleite, (d, e, f) buckyballs (C60, C540, C70), (g) amorphous carbon and (h) a carbon nanotube (reproduced from Ref. 2.1).

Carbon has four electrons in its outer shell. Two electrons, with opposite spin are found in the first shell, the K shell. This shell is at the lowest possible energy and is completely stable. The second shell, the L shell, consists of two sub-shells (2s and 2p orbitals) which contain the remaining four electrons. Two will go into the 2s orbital with opposite spins. The remaining two will be in two separate 2p orbitals. This is because the p orbitals have the same energy and the electrons would rather be in separate orbitals.

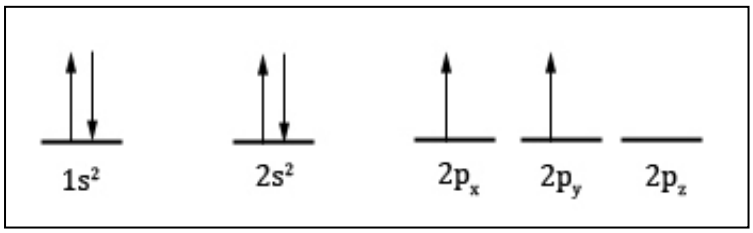

Figure 2.2: Distribution of electrons available at energy levels for carbon at its ground state.

Once the carbon atom is in its excited state (C*) with four unpaired electrons, the four atomic orbitals (A.O.s) can be mixed together to form four equivalent hybrid orbitals (H.O.s). This process is called hybridisation. In bonded carbon, such as diamond and graphite sp^n hybridisation of orbitals occur with n = 1,2,3.[2.2] The three possible hybridizations of orbitals occurring in carbon are: sp^3 (tetragonal), sp^2 (trigonal) and *sp* (diagonal), this is due to mixing of electronic wave functions of the 2s and 2p orbitals.

When the carbon bonds in diamond are formed, orbital hybridisation occurs allowing the 4 electrons in the L shell to take up places in separate orbitals. One of the $2s^2$ orbital electrons gets promoted up to a vacant 2p orbital, forming hybrid set of orbitals appropriately designated sp^3 having one s orbital and 3 p orbitals.[2.3] The four sp^3 hybrid orbitals will arrange themselves in three-dimensional space to get as far apart as possible (to minimise repulsion). The geometry that achieves this is tetrahedral geometry, where any bond angle is 109.5 °. The stable electronic configuration for the 2nd shell is eight and as a result, each one of the 4 sp^3 valence electrons covalently bonds with one valence electron of other carbon atoms making each carbon attached to 4 carbon atoms thus forming a tetrahedral carbon

interconnected structure called the diamond lattice Each bond is a sigma (σ) bond and the hybridisation energy amounts to 230 kJ mol^{-1}. [2.2]

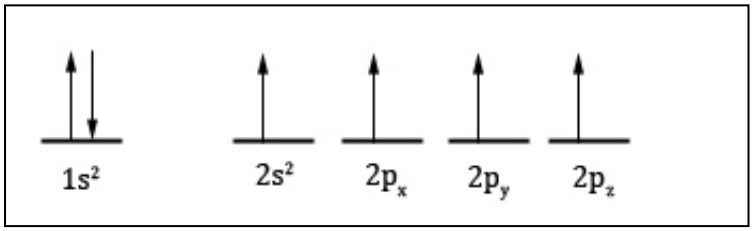

Figure 2.3: 4 *sp³* hybrid orbitals are formed.

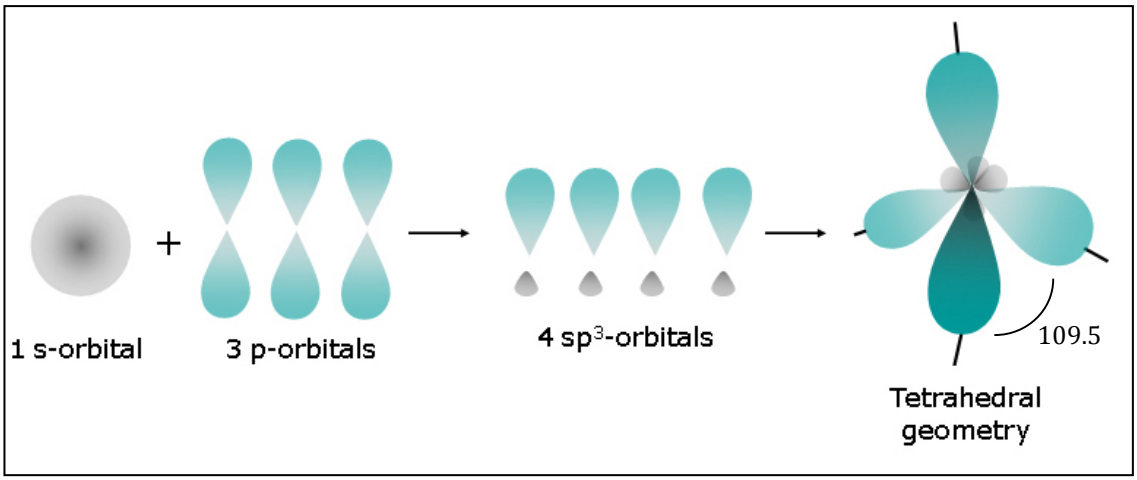

Figure 2.4: 4 *sp³* hybridisation of carbon forming tetrahedral geometry.

Graphite is an example of *sp²* hybridisation. The *sp²* hybrid orbitals are generated when 3 of the 4 electrons in the 2s and 2p orbitals combine and achieve a planar trigonal geometry where the bond angle between the hybrid orbitals is 120 °. The lone 2p electron i.e., the delocalized electron, is directed perpendicularly to the plane and paired with another delocalised electron of the adjacent plane by a much weaker van der Waals bond. Therefore a single carbon atom forms sigma bonds with three others forming a series of continuous hexagonal structures, all located in parallel planes - two dimensional carbon sheets called graphene. Sheets of graphene stack up to create graphite with the unhybridised 2p electrons establishing pi (π) bonds, weakly binding the carbon layers together by Van der Waals forces.

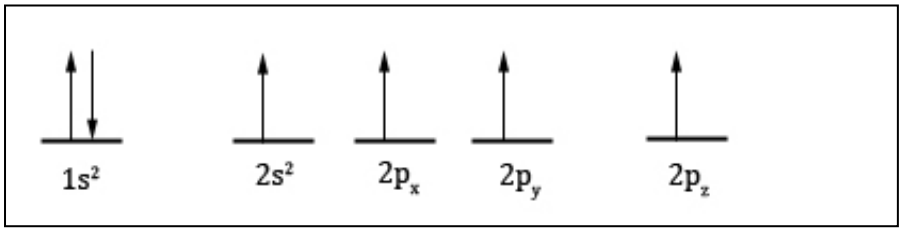

Figure 2.5: 3 *sp²* hybrid orbitals are formed.

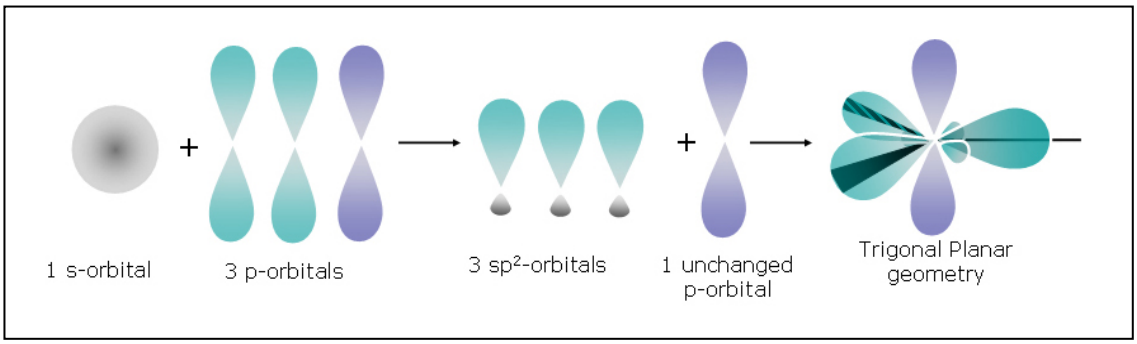

Figure 2.6: Formation of three *sp²* hybrid orbitals forming a trigonal planar geometry

2.2 Diamond

The diamond lattice

Each tetrahedron combines with four other tetrahedra, forming a strongly-bonded, uniform, three-dimensional, entirely covalent crystalline structure. The covalent bonding between carbon atoms is characterised by a small bond length of 0.154 nm and a high bond energy of 348 kJ mol^{-1}.

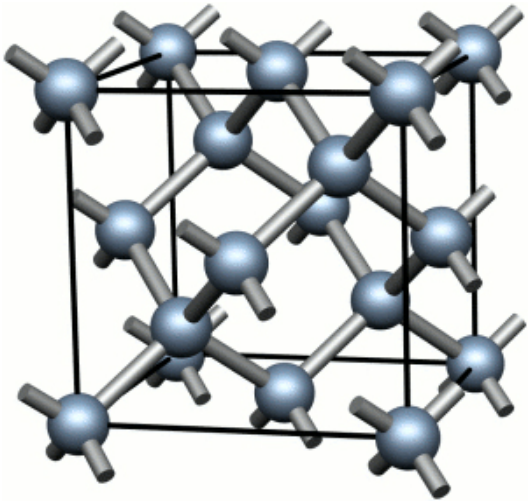

Figure 2.7: The crystal structure of diamond is a face-centred cubic (FCC) lattice, with a basis of two identical carbon atoms associated with each lattice point (reproduced from Ref. 2.4)

Natural diamond is thought to have formed over 990 million years ago between 140 and 200 km from the Earth's surface, where temperatures range between 900 °C to 1400 °C and pressures between 45 to 60 kbar.[2.5] Other than for their beauty as gemstones, natural diamonds are mainly used as abrasives and cutting tools. Natural Diamonds have been historically classified into four categories according to their optical absorption properties, which are determined by impurities of nitrogen-, boron- and hydrogen-related defects as listed in table 2.1.

Type	Description
Ia	Nitrogen is the dominant impurity and is present as aggregates or clustered together within the carbon lattice. It has a pale yellow or brown appearance. 98% of diamonds fall into this category.
Ib	Nitrogen is present as single substitutional atoms and is uniformly distributed throughout the carbon lattice. These diamonds can appear deep yellow, orange, brown or greenish depending on the concentration and distribution of nitrogen atoms. They account for 0.1 % of diamond
IIa	These diamonds have a miniscule amount of impurities present. They are colourless unless lattice defect are present, which would render them yellow, brown, pink or red. 1-2 % of diamonds are this type.
IIb	This type of diamond contains boron as an impurity and appear, blue, grey or near-colourless and make up approximately 0.1 % of diamonds.

Table 2.1: Classification of natural diamond types (taken from Ref. 2.2)

2.2.1 Synthetic Diamond

Natural, bulk diamond cannot be effectively engineered into the many physical configurations required to exploit many of its properties. The developments in the synthesis of diamond, in particular chemical vapour deposition (CVD) have led to the ability to grow diamond in the form of thin films or coatings on a variety of shapes, with control over attributes such as the grain size. This has enabled the exploitation of more combinations of some of extreme properties of diamond for specific applications.

Large, transparent, single crystal diamond is typically used in gemstones although it may have applications in the realm of electronics such as electron amplification. Polycrystalline diamond consists of numerous small grains and as such is unsuitable as a gemstone. It is used for industrial applications such as mining and cutting tools as well as in recent years, pioneering research work to create electronic devices. The average (grain) size of the crystal defines the polycrystalline diamond. Grain sizes range from nanometres to hundreds of micrometres usually referred to as "nanocrystalline" and "microcrystalline" diamond, respectively.[2.6] Diamonds in the form discrete nano-sized grains are termed nanodiamonds and typically kept suspended in solutions. Nanodiamond particles agglomerate to form micro-sized clusters. The synthesis, processing and applications of nanodiamond particles will be reviewed later in this chapter.

2.2.2 Growth of diamond

Artificial diamond synthesis was first reported in 1955 by General Electric by using the high-pressure high-temperature (HPHT).[2.7] Under these conditions diamond is thermodynamically stable and can be formed, typically from a graphite source.[2.8] The transformation of graphite to diamond, although thermodynamically feasible at relatively low pressure and temperatures, faces considerable kinetic barriers since the rate of transformation decreases with increasing pressure. This kinetic consideration supersedes the thermodynamic conditions and it was found experimentally that very high pressure and temperature (>130 kb and ~3300 K)

were necessary in order for the direct graphite-diamond transformation to proceed at any observable rate.[2.9] Unsurprisingly, these conditions are difficult and costly to achieve. Using a solvent-catalyst reaction, it is possible to bypass this kinetic barrier by establishing a reaction path with lower activation energy than that of direct transformation. Molten metal catalysts are used to dissolve carbon and acceleration its conversion into diamond. The solvent-catalysts are the transition metals such as iron, cobalt, chromium, nickel, platinum, and palladium. These metal-solvents dissolve carbon extensively, break the bonds between groups of carbon atoms and between individual atoms, and transport the carbon to the growing diamond surface. [2.3]

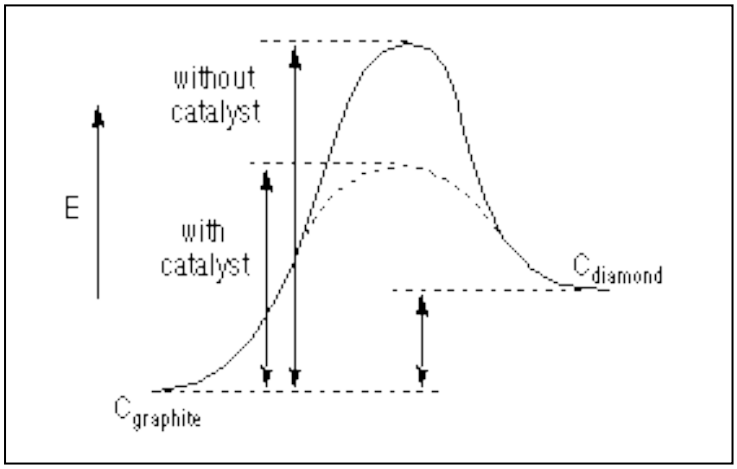

Figure 2.8: Energy diagram displaying the conversion of graphite to diamond, with and without a catalyst (from Ref. 2.10)

At the same time, studies were being carried out in order to deposit diamond from the gas phase. The first documented report of diamond growth at a low pressure was that of W Eversole in 1954 using thermal chemical vapour deposition.[2.11] Patent applications by Eversole of the Union Carbide Corporation in 1962 outlined the low pressure CVD technique used; this was far superior to earlier techniques that also produced large quantities of graphitic carbon. In 1956, the former USSR scientists Spitsyn and Deryagin proposed the growth of diamond at low pressures through the thermal decomposition of carbon tetraiodide (CI_4).[2.12] Diamonds were synthesized using CBr_4 or CI_4 at temperatures ranging from 800 to 1000 °C and pressures of approximately 4×10^{-4} Pa. The Soviet group subsequently explored direct CVD from hydrocarbons and in 1969 it was stated that diamond was

synthesized from pure methane at pressures from 13 to 40 Pa and temperatures from 950 to 1050 ºC with a growth rate about an order higher than that reported by Eversole. A major breakthrough in the CVD diamond process was achieved in the early 1970s. Atomic hydrogen used in the growth process was found to remove graphite co-deposits, based on the face that atomic hydrogen etches graphite much faster than it does diamond. This gave a much higher growth rate and permitted nucleation of new diamond crystallites on non-diamond substrates.

The modern era of CVD diamond began in the early 1980s. The National Institute for Research in Inorganic Materials (NIRIM) based in Japan, publishing a series of papers in which different techniques were described: hot filament CVD processes, RF-plasma CVD and microwave plasma CVD (MWPCVD).[2.13, 2.14, 2.15, 2.16] They reported that diamond particles and films could be deposited on various substrates heated around 850 ºC, using a gas mixture of methane diluted by hydrogen, and preferred partial pressures in the range 4×10^3 – 5×10^3 Pa. A growth rate higher than several micrometres per hour was achieved. Several research groups in the USA and Europe soon confirmed these results.

Since then, extensive research has been carried out by many groups into process techniques, understanding the mechanism of CVD diamond nucleation and growth, diamond doping, investigation of optical, electronic, thermal, mechanical properties of CVD diamond, diamond coating on various substrates for specific applications and characterisation of CVD diamond. Until the late 1980s most of the significant developments reported were due to Japanese work. These include the development of filament-assisted thermal CVD,[2.5, 2.6] electron-assisted thermal CVD,[2.17] laser-assisted thermal CVD,[2.18] RF plasma CVD,[2.19] microwave-plasma CVD,[2.20] combustion flame-assisted CVD [2.21] and direct-current arc plasma jet CVD.[2.22] Although a number of enhanced CVD methods exist, with different process details, there are a number of important common features.

The basic reaction in the CVD diamond process is the decomposition of a hydrocarbon, typically methane. The two basic activation methods are by using high temperature or by electronic or electromagnetic gas discharge. The presence of atomic hydrogen is also crucial. Atomic hydrogen plays an essential role in the surface and plasma chemistry of diamond deposition as it contributes to the

stabilisation of the sp^3 dangling bonds found on the diamond surface plane.[2.23] Without this stabilising effect, these bonds would not be maintained and the diamond plane would collapse (flatten out) to the graphite structure. The other function of atomic hydrogen is to suppress the formation of graphite. In contrast with molecular hydrogen, atomic hydrogen is extremely reactive. It etches graphite fifty times faster than diamond. This etching ability is important since, when graphite and diamond are deposited simultaneously, graphite is preferentially removed while most of the diamond remains.[2.24] Thus, growth of diamond from carbon containing molecules diluted in hydrogen involves two processes. The first is carbon deposition primarily in the form of graphite with a small amount of diamond, and the second is selective etching of graphite by atomic hydrogen. As a result, the various enhanced CVD methods for the growth of diamond are optimised to produce atomic hydrogen from molecular hydrogen close to the surface of the growing film.

The next consideration is the dissociation of the carbon containing source gases. In a simple thermal CVD process, the diamond growth rate is very low (<0.1 μmh^{-1}). This is due to the rather high activation energy needed for the decomposition of methane on the surface of diamond. Thus, in the various enhanced CVD methods, the carbon containing compounds are dissociated by thermal, plasma or combustion processes to produce the reactant species responsible for the diamond nucleation and growth. The film growth rate depends on the ability of these reactant species to be transported to the substrate.

Figure 2.9 shows a schematic diagram for the processes occurring during the growth process. The gaseous reactants are dissociated into highly reactive radicals and reactant species using the chosen activation method. The most abundant carbon containing precursors in typical diamond growth systems are methyl radicals and acetylene molecules.[2.25] These growth species are then delivered to the growth surface.

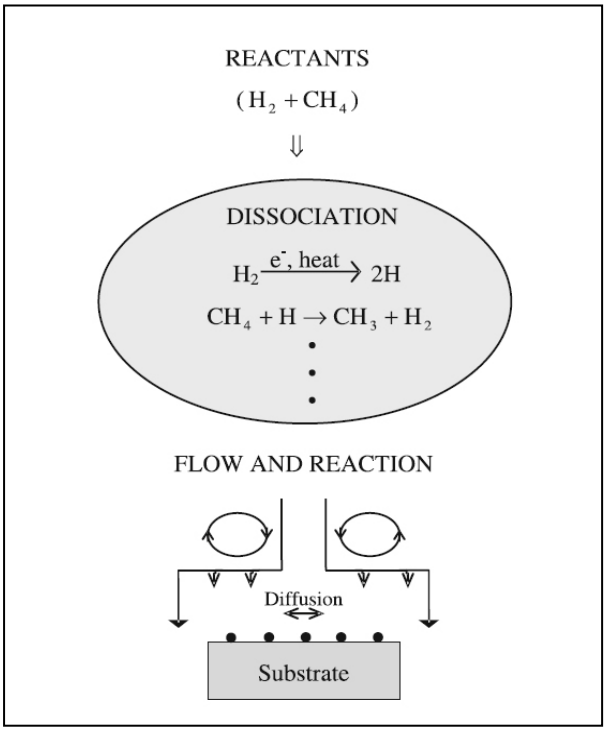

Figure 2.9: Schematic diagram of the processes occurring during diamond CVD (taken from Ref. 2.26)

CVD diamond growth goes through a series of steps i.e. nucleation, formation of a continuous film and competitive growth of crystallites. The nucleation and early growth stages are critical in determining the film properties, morphology, homogeneity, defect formation, adhesion and the type of substrates that can be successfully coated. Diamond can grow homoepitaxially on a diamond surface without nucleation problems HFCVD,[2.27,2.28] MWPACVD[2.29, 2.30] and ECR MW PACVD[2.31] from a variety of carbon sources . However, substrate pre-treatment of non-diamond surfaces is essential, without this, only a few isolated diamond crystallites be will found on a non-diamond substrate which has been exposed to proper growth conditions.

2.2.3 Nucleation

Various nucleation procedures have been proposed and are utilised with research continuing to improve these processes. The simplest is abrasion using diamond grit,[2.32] which leaves small diamond particles of sizes in the range 2-10nm on the

surface that act as growth sites. This method has some limitations: it can only be used with flat surfaces and can damage any intermediate layers that may be present. Diamond nucleation densities after scratching pre-treatments range typically from 10^6 to 10^{10} cm^{-2}, as compared to < 10^5 cm^{-2} on untreated surfaces.[2.33.]

Ultrasonic treatment is a gentler method, where the substrate is immersed in an ultrasonic bath, with the diamond powder dispersed in an organic solvent, such as methanol. This method can be used with 3-D shaped substrates and the appropriate choice of diamond particle size and seeding time allows further control of the nucleation procedure. Nanodiamond (ND) particles, in the form of a colloidal solution can also be used in the ultrasonic method. Nucleation densities as high as 10^{11} cm^{-2} have been obtained with this method. Spin coating of nanoparticle solutions, with or without polymers or surfactants is also mentioned in several studies.[2.34, 2.35] With all these methods, the nanodiamond deposits are strongly dependent on various parameters such as the dispersion and concentration of the nanoparticles in the colloid solutions.

Spin-coating deposits may be strongly disturbed by the roughness of the substrate and fragile substrates may suffer from the ultrasonic treatment. Girard *et al.* presented a simple approach to disperse NDs on a substrate by taking advantage of the oxygenated terminations present on the diamond nanoparticle surface.[2.36] These chemical groups provide the particle an electrostatic charge. The approach relies on the use of an oppositely charged substrate: the nanoparticles can hence be simply deposited by electrostatic interactions. This technique is called layer-by-layer deposition. With this method, the authors have deposited negatively charged HPHT diamond nanoparticles on various substrates previously coated with a cationic organic polymer. By simple dipping of the coated substrate into the ND solution, electrostatic interactions ensures a spontaneous grafting of the particles onto the surface resulting in reproducible and homogeneous nanoparticle films. This approach has been shown to work on a several kinds of materials and also on 3-D structures.

Once the small diamond crystallites are present on the non-diamond surface by the chosen nucleation procedure, they begin growing three dimensionally until the grains coalesce and form a continuous film; this period of time is known as the

incubation period. The growth proceeds with competitive crystal growth between the crystals oriented along the fastest growth direction.

The majority of research into the growth of diamond films is divided into two categories; whether the films are grown with the suppression or enhancement of re-nucleation processes. In conventional diamond growth, hydrogen-rich gas phase chemistry is used which is known to reduce the re-nucleation by the significantly higher etch rate of graphite over diamond in such a plasma. This results in an increase in the grain size from the small seeding crystals and after a given thickness the grains will no longer be of nanometre scale. This material is conventionally referred to as microcrystalline diamond (μCD). If this material is grown very thin and with high nucleation density, then coalesced films with grains sized less than 100 nm can be grown and this material is termed nanocrystalline diamond (NCD). Nanodiamond films grown with a significant re-nucleation rate by reduction of the hydrogen concentration in the plasma allows some sp^2 binding to create new unepitaxial nucleation sites on the facets of growing crystals. This limits the maximum grain size and thick films can be grown with a small distribution of grain sizes. This material is known as ultrananocrystalline diamond (UNCD) and typically has a grain size of between 3-5nm regardless of film thickness.[2.37] Figure 2.10 illustrates the difference in the grain sizes using these two distinct methods.

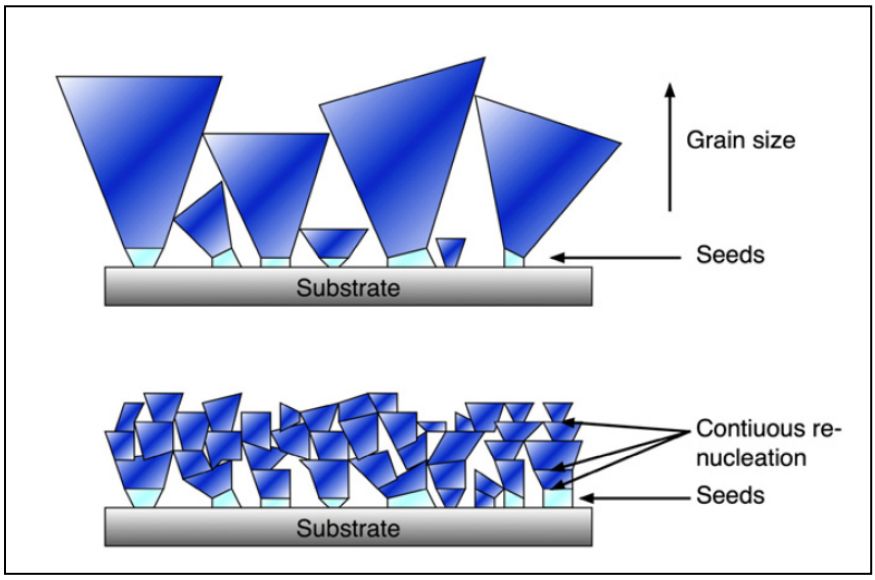

Figure 2.10: Schematic illustration of the difference between nanocrystalline diamond (NCD) and ultrananocrystalline diamond (UNCD) (from Ref. 2.38).

Although this type of film might be considered inferior to the more crystalline and therefore better quality diamond films, it still possesses many of the desirable properties of diamond whilst being much smoother and considerably faster to deposit. Thus, by the simple tactic of changing the growth conditions, diamond films can be deposited with properties ranging from almost graphite to essentially those of natural diamond. This allows the quality, appearance and properties of a diamond film, as well as its growth rate and cost, to be easily designed to suit particular applications.

2.2.4 Microwave-Plasma CVD

A range of diamond growth techniques involve various forms of plasma-assisted CVD using carbon-containing species mixed in a low concentration with hydrogen. Plasma is generated by various forms of electrical discharges or induction heating. Microwave plasma-assisted CVD has been used more extensively than others for the growth of diamond films and is the reactor type used in the work of this thesis. The plasma generates atomic hydrogen through the electron impact dissociation of molecular hydrogen and produces proper carbon precursors for diamond growth.

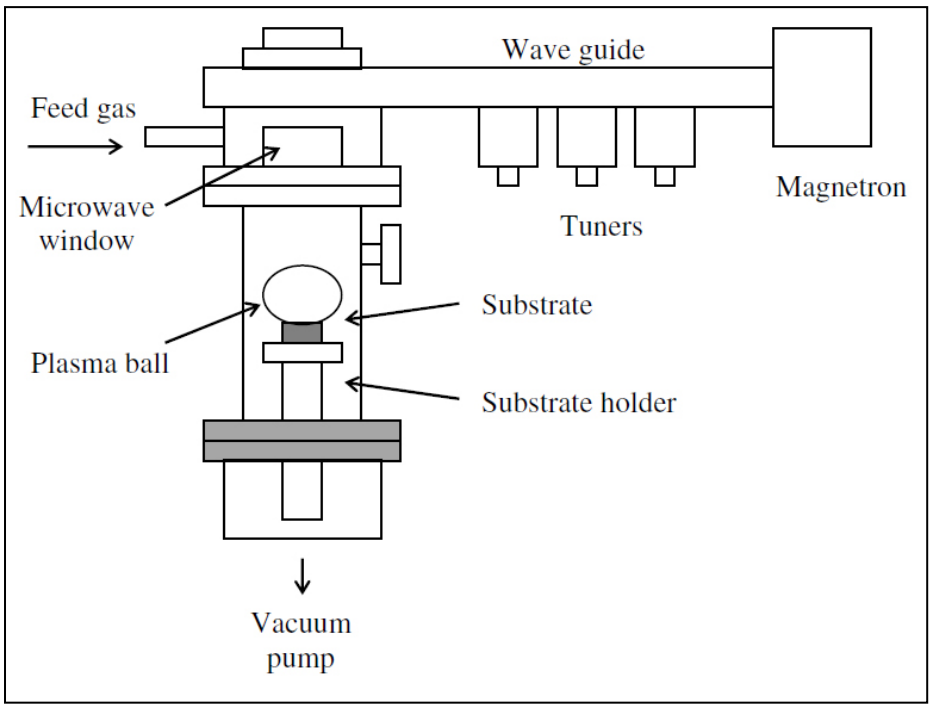

Figure 2.11: A modern MWPCVD reactor (taken from Ref. 2.39)

Glow-discharge (non-isothermal) plasma is generated in a gas by a high-frequency electric field such as microwave, at relatively low pressure. The gases are ionised into electrons and ions in the high-frequency field. The electrons are accelerated to high energy levels corresponding to 5000 K or higher. The heavier ions with their greater inertia cannot respond to rapid changes in the field direction and as a result, their temperature and that of the plasma, remain low. The high energy electrons collide with the gas molecules resulting in dissociation and the generation of the reactive chemical species required for the chemical reactions.

Figure 2.11 shows a schematic diagram of a modern microwave-plasma CVD system. The substrate is placed towards the lower end of a tube, in which the plasma is generated. The gases are introduced at the top of the reactor and the gaseous by-products are removed into the exhaust. The 2.45 GHz microwave is coupled from the rectangular waveguide into the cavity via an axial antenna. The discharge, a "plasma ball" is generated above the substrate. Its shape, size and stability are dependent on the deposition conditions; the plasma power, the pressure and the gas composition. Under the correct conditions a ball-shaped, stable plasma is formed in the centre of the tube, away from the reactor walls. The plasma ball provides the substrate heating.

In the earlier, NIRIM-type reactors the CH_4/H_2 plasma is generated in a cylindrical quartz tube which intersects the rectangular waveguide. The modern ASTeX rectors have overcome lot of the limitations of the NIRIM-type reactors. The plasma has no contact with the reactor walls so the incorporation of impurities is greatly reduced. If operated under well-defined deposition conditions, it is possible to deposit diamond continuously and unattended for several days or even weeks. The use of higher microwave power allows the production of diamond discs 5 cm in diameter.

This method of diamond growth has distinct advantages over the other methods. Being an electrode-less process, avoids contamination of the films due to electrode erosion. The microwave discharge at 2.45 GHz is a higher frequency process than the radio frequency (RF) discharges (13.5 MHz), which produces a higher plasma density with higher energy electrons. This should result in higher concentrations of atomic hydrogen and hydrocarbon radicals.

Reviews of the various different CVD methods mentioned can be found in the paper "Diamond growth by chemical vapour deposition"[2.40] and the book, "Carbon Nanowalls".[2.41]

2.2.3 Diamond doping

Electronic applications generally require extrinsic semiconducting materials. To achieve this impurities are inserted to the crystal structure that generate additional electron energy levels within the band gap; this process is called doping. Compared to silicon and other common semiconductor materials, diamond's extremely compact lattice does not favour the presence of substitutional impurities. Consequently only a few species can be used as dopants for diamond.

Energy levels created near the conduction band by dopant atoms containing extra electrons act as donors. These electrons can then be thermally excited into the conduction band to carry an electric current (n-type conduction). Typical atoms that can act as donors in diamond are the group V atoms; nitrogen, phosphorus and arsenic. If the dopant atoms generate energy levels, devoid of electrons, near the valence band, they act as acceptors. Electrons can then be excited from the valence band into these levels, leaving behind positive holes which can act as carriers for the generation of an electric current (p-type conduction). Typical acceptor atoms are from group III such as boron and aluminium.[2.42]

The methods of diamond doping are limited to dopant uptake during growth or dopant injection using ion implantation. This is because diamond cannot be heated to temperatures at which vacancies and interstitial atoms form by thermal excitation. Therefore any diffusion process that relies on these defects as carriers is not possible. For this reason, it is difficult to introduce dopant atoms by in-diffusion as in the case of silicon doping. Even if they can diffuse in by some interstitial atom mechanism, there will not be vacant lattice sites available for them to occupy and hence become electrically active.

P-type diamond (during growth)

P-type extrinsic semiconducting diamonds, doped with boron acceptors are found in nature and are known as type IIb diamonds. The boron acceptor has been well studied and its activation energy is 0.37 eV above the valence band. This is still quite a large energy, which means that at room temperature only about two out of every thousand acceptors are ionised to create holes in the valence band. However, p-type diamonds can conduct well at room temperature, and transistor action has been demonstrated in them.[2.42]

Boron can be incorporated into diamond during both HPHT and PACVD growth. Under HPHT conditions, the solvent catalyst often contains materials that getter the nitrogen in order to stop its incorporation and to prevent these atoms from compensating the boron. In general, these boron-doped diamonds tend to be over-doped. This can result in a change of the conduction mechanism, from hole conduction in the valence band to conduction by carriers that tunnel from one acceptor state to the next (called hopping conduction). The latter conduction degrades device performance and, if possible, should be avoided. Doping during PACVD growth is accomplished by introducing diborane (B_2H_6), boric acid or boron oxides. The quality of boron-doped diamond layers grown by PACVD has improved steadily over the last ten years, and single crystalline layers grown homoepitaxially on diamond with hole mobilities in excess of 1000 $cm^2V^{-1}s^{-1}$ can now be produced. The activation energy required for hole excitation into the valence band has been demonstrated to be concentration dependent, down to a few meV at boron concentrations > 1×10^{20} cm^{-3}. [2.42]

N-type diamond (during growth)

Of the group V elements which are potential substitutional donors in group IV semiconductors, only nitrogen (N) and phosphorus (P) seem to enter the diamond crystal and contribute to its electrical properties. Nitrogen is abundant in natural diamonds and can be synthesized under HPHT laboratory conditions with an activation energy of 1.7 eV.[2.43] Due to these very high ionisation energies, N containing diamonds are electrically insulating at room temperature. P and N can be introduced into the diamond also during CVD growth. The quality of P layers is

still poor and the activation energy for electron excitation into the conduction band lies at E > 0.5eV

Ion implantation

In ion implantation, dopant atoms are ionised and driven to high velocities by electric fields in an accelerator (ion implanter) where they impinge on to the surface of the semiconductor substrate, and are injected into the underlying bulk to a depth that depends on the mass and energy of the ions. This technique is widely used to dope silicon and other semiconductor materials. Using this process, it is possible to accurately control the number and location of the dopant atoms. However, the process also introduces a large number of defects in the material which have to be removed by subsequent annealing. Such high temperatures cannot be used with diamond and the presence of these defects can even lower the temperature at which graphitisation occurs.[2.44] Additionally, broken sp^3 bonds and other implantation-related defects or graphitic clusters can give rise to electrical effects which may be mistaken for real chemical doping due to the presence of dopants.[2.42]

The method of cold implantation-rapid annealing (CIRA) has been reported to have the best success. In this method the diamond is implanted at low temperature, rapidly heated to 800 K to induce interstitial-vacancy recombination before the interstitial can diffuse away from the implanted layer, and then annealed at high temperature (1700 K) to further reduce the radiation damage and increase the electrical activation of the dopants.[2.42] This technique was based on Prins earlier investigations on the role of implantation temperature on the nature of the defects.

The ion implantation of boron is now a well-controlled process which has been optimised in the last five years. This has resulted in doping efficiencies of the order of 2-5 % and hole mobilities of up to 600 $cm^2V^{-1}s^{-1}$. The optimal implantation-annealing scheme compromises of a multiple energy cold implantation followed by a medium temperature and a high temperature (T > 1400 °C) annealing stage. The fabrication of over-doped highly conductive layers can be achieved either by hot implantations (high dose, high current implantations into poorly heat sunk samples), or by high dose implantations followed by annealing and graphite

removal. These are widely used for creating ohmic contacts to p-type diamond. Optical characterisation of the B acceptors in substitutional sites is well understood and is a useful tool in the study of defect-dopant interaction.[2.42]

Ion implantation offers precise control of dopant concentration as ion beam current can be measured. Good uniformity over the surface, uniform depth profile obtained by multiple implantations at different energy levels and selective doping at preferential sites are other advantages of this technique. However, the drawback is the inevitable lattice damage caused by ion bombardment.

2.2.4 Surface conductivity

The diamond surface can be terminated by a variety of elements or molecules, giving rise to new phenomena and applications. Hydrogen terminated diamond gives rise to negative electron affinity (NEA) due to the formation of carbon-hydrogen dipoles. This is described in more detail in chapter 3.1.3. Under vacuum conditions, such surfaces are insulating, however, if hydrogen terminated surfaces are exposed to air, surface conductivity can be detected. It is now well established that for surface conductivity to occur hydrogen termination in combination with adsorbate coverage is required. The origin of surface conductivity is due to holes created in the diamond near surface as a result of electrons tunnelling into available states in the adsorbed electrolyte layer. A thin water layer, as it forms naturally on all surfaces exposed to atmosphere, provides an electron system, which can act as a surface acceptor for diamond. Electron exchange from diamond to the water layer is governed by a redox reaction.[2.45]

The sample can be put into vacuum and the wetting layer removed. As long as the anions remain at the surface the hole accumulation will also be preserved. Thermal desorption of the anions which takes place at much lower temperatures (~300 °C) than those necessary for surface dehydrogenation in UHV (~1000 °C), removes the accumulation layer and leaves a hydrogenated but highly resistive surface.[2.46]

2.2.5 Applications of diamond

Diamond has extreme mechanical and excellent electronic properties. CVD diamond offers broad potential and there are many applications which can take advantage of the intrinsic properties of diamond, such as in semiconductors, optics, optoelectronics, corrosion coatings and others. Table 2.2 lists a selection of these mechanical and electronic properties.

Properties	**Single Crystal Diamond**
Density (gcm^{-3})	3.567
Young's modulus (GPa)	910-1250
Poisson's Ratio	0.2
Compression Strength (GPa)	8.68-16.53
Thermal expansion (K^{-1})	1.05×10^{-6}
Thermal conductivity at 25°C ($W\ m^{-1}\ K^{-1}$)	2200
Thermal capacity at 27°C ($J/mol{\cdot}K^{-1}$)	6.195
Vicker's hardness (GPa)	57-104
Electrical resistivity (Ω cm)	10^{16}
Electronic Properties	**CVD**
Band gap (eV)	~5.45
Dielectric constant at 45 MHz-20 GHz	5.6
Dielectric strength (MV cm-1)	4-10
Loss tangent at 45 MHz-20 GHz	<0.0001
Saturated electron velocity ($cm\ s^{-1}$)	2.7×10^{7}
Carrier mobility (cm^2/Vs)	
Electron (n)	2200
Hole (p)	1600

Table2.2: Properties of single crystal diamond and electronic properties of CVD diamond. (from Ref. 2.2)

Grinding and cutting

CVD diamond coatings provide excellent protection against chemical and physical abrasion due to their hardness and chemical inertness. The coatings are used on tools from industrial drilling tools to surgical scalpels.

Thermal management

Diamond, an electrical insulator with the highest thermal conductivity at room temperature compares favourably with conventional heat-sink materials such as aluminium, copper or ceramics. Current applications for diamond heat spreaders include mountings for laser diodes, laser diode arrays, and high power transistors. More recently, micro and nano-sized diamond particles have been incorporated into thermal paste which has far superior thermal conductivity than pastes based on silver or ceramics.

Optical applications

In addition to being hard, chemically inert and possessing excellent thermal conductivity, diamond has a wide range of transparency and a low coefficient of thermal expansion. These properties make diamond far superior to any other existing window material used for transmitting infrared and microwave. Recent advances in the HPHT and CVD synthesis techniques have led to greater purity and crystallinity of single-crystalline diamond, enough to replace silicon as a diffraction grating and window material in high-power radiation sources, such as synchrotrons. Both the CVD and HPHT processes are also used to create designer optically transparent diamond anvils as a tool for measuring electric and magnetic properties of materials at ultra high pressures using a diamond anvilcell.

Electronic applications

Diamond has excellent semiconductor properties, coupling these with its radiation and temperature resistance and high thermal conductivity, diamond is the ideal material for many semiconductor applications such as high-power and high-frequency transistors or for example, in the harsh environments found in internal combustion and jet engines. Boron doped CVD diamond is now an established technology and there are many examples in the literature of semiconductor devices based on CVD diamond. These include field effect transistors (FETs) that are characterised by high-power handling capacity, low saturation resistance, and excellent high-frequency performance.[2.47] For CVD diamond to be seriously

considered as an electronic material, reproducible high quality n-type diamond is a necessity. As discussed earlier in this chapter, this is yet to be realised. Therefore, most devices made from diamond are unipolar utilising the p-type hole conduction. These include Schottky diodes on boron doped diamond operating up to 1000 °C,[2.48] boron/nitrogen pn-junction diodes,[2.49,2.50] bipolar transistors based on this pn-junction[2.50] and field effect transistors (FETs)[2.48] with boron delta-doped channel and hydrogen-related surface conductive layers.[2.51] Diamond also shows promise as a cold cathode material due to the negative electron affinity when the surface is appropriately terminated.[2.52]

2.3 Nanodiamond particles: synthesis, purification and applications

Nanoscale diamond particles are rapidly becoming an important class of materials resulting from their excellent mechanical and optical properties, high surface area and the ability to functionalise the surface structure. Nanodiamonds can be synthesised using a wide array of methods, such as the detonation technique, laser ablation,[2.53] high-energy ball milling of high-pressure high temperature diamond microcrystals,[2.54] plasma-assisted CVD,[2.55] and others.[2.56]

The material of particular interest is single digit nanodiamond produced by the detonation process and then subsequently de-aggregated. This material is now commercially available and there has been a great deal of research into its purification and processing. A single particle of detonation nanodiamond (DND) consists of a chemically inert diamond core and chemically active surface with controllable properties. They can exist as powders where the DND form aggregates and as suspensions of either aggregated or isolated particles.

Three main methods have been commercialised to produce nanodiamond using explosives. The first is shockwave synthesis, which can transform graphitic material into diamond crystals. The second is based on the detonation of a mixture of carbon containing material with explosives. The third method utilises the carbon atoms within the explosives alone.

2.3.1 Shockwave Synthesis

Carbon precursors (e.g. graphite, coal, and carbon black) can be transformed to diamond in a capsule compressed by a shockwave generated outside the capsule. Carbon material is placed in an inner tube covered with a driving tube. The whole system is placed in the outer tube and the free space is filled with explosive. The ignition of this explosive at one end of the apparatus leads to the propagation of a circular shock wave that compresses the driving tube. This explosively produced shockwave can create high pressure (~140 GPa), high temperature conditions in a confined volume for a sufficient duration to achieve partial conversion of graphite to nanometer sized diamond grains. The grains are compacted into micron-sized, polycrystalline particles. To prevent diamond re-graphitisation, a mixture of graphite (6 to 10 %) with metallic powder (Cu, Al, Ni) is used. The diamond yield is about 60 mass percent of the carbon phase or about 5 % of the initial mixed material loaded into a capsule.

This is known as the 'Du Pont method' as it was commercialised by Du Pont de Nemour & Co, to produce polycrystalline diamond particles of micron size (1 to 60 μm), widely used in fine polishing applications.

2.3.2 Detonation Nanodiamond

Two methods of producing nanodiamond via more effective detonation processes exist. The first is based on the detonation of a mixture of carbon-containing material with explosives. This method was initiated in Russia in the early 1960s soon after Du Pont's work on shock wave synthesis. Diamond formation takes places both within the carbon containing particles as well as by condensation of the carbon atoms contained in the explosives. The explosion can be done in air or in an inert atmosphere relative to the product of synthesis. In the latter case, a diamond cubic phase not more than 20 nm in size is formed. When the formation is in an atmosphere of air, the samples always contain londsdaleite and the particle size is about 8 nm. The diamond yield constitutes up to 17 % of the mass of the initial carbon material or about 3.4 % of the mass of the explosives. Diamond

obtained by this method is also polycrystalline, with particle sizes comparable to the particle sizes of the precursor carbon material.

The second method of detonation synthesis uses only the explosive material as a precursor material, in a closed container. Diamond clusters are formed from carbon atoms containing within explosive molecules themselves. A wide variety of explosive materials can be used, including products for military applications. A typical explosive is a mixture of TNT (2-methyl- 1,3,5-trinitrobenzene) and hexogen (in proportion 60/40) composed of carbon, nitrogen, oxygen and hydrogen with a negative oxygen balance, so that 'excess' carbon is present in the system; an important condition for ultra-dispersed nanodiamond (UDD) formation. The explosion takes place in a non-oxidising medium of either gases (N_2, CO_2, Ar, or other media that can be under pressure) or water (ice) so-called dry or wet synthesis correspondingly, that plays the role of a coolant.

To prevent the UDD formed in the detonation wave from transforming into graphite at the high temperature generated by the detonation, the cooling rate of the reaction products should be no less than 3000 K/min. The initial shock from a detonator compresses the high explosive material, heating it and causing chemical decomposition that releases enormous amounts of energy in a fraction of a microsecond. As the detonation wave propagates through the material it generates high temperatures (3000 to 4000 K) and high pressures (20 to 30 GPa) that correspond to conditions of thermodynamic stability for diamond. During detonation, the free carbon coagulates into small clusters, which grow larger by diffusion.[2.57] Figure 2.12 shows the phase diagram of diamond-graphite. The most stable phase of carbon is graphite at low pressures, and diamond at high pressures, with both phases melting when at temperatures above 4500 K (with the precise melting temperature for each phase depending on the pressure). The phase diagrams for nanoscale carbon are similar, but the liquid phase is found at lower temperatures.[2.58] During detonation, the pressure and temperature rise instantaneously, reaching the Jouguet point (point A), which falls within the region of liquid carbon clusters of 1–2 nm in size for many explosives. As the temperature and pressure decrease along the isentrope (red line), carbon atoms condense into nanoclusters, which further coalesce into larger liquid droplets and crystallise.

When the pressure drops below the diamond–graphite equilibrium line, the growth of diamond is replaced by the formation of graphite. Figure 2.12(b) shows the schematic of the detonation wave (I) the front of the shock wave caused by the explosion; (II) the zone of chemical reaction in which the explosive molecules decompose; (III) the Chapman–Jouguet plane (where P and T correspond to point A, indicating the conditions when reaction and energy release are essentially complete); (IV) the expanding detonation products; (V) the formation of carbon nanoclusters; (VI) the coagulation into liquid nanodroplets; and (VII) the crystallisation, growth and agglomeration of nanodiamonds.

The product of detonation synthesis, called detonation soot or diamond blend, contains 40 to 80 wt.% of the diamond phase depending on the detonation conditions. The carbon yield is 4 to 10% of the explosive weight for the most effective of the three industrial methods of diamond production using explosives.

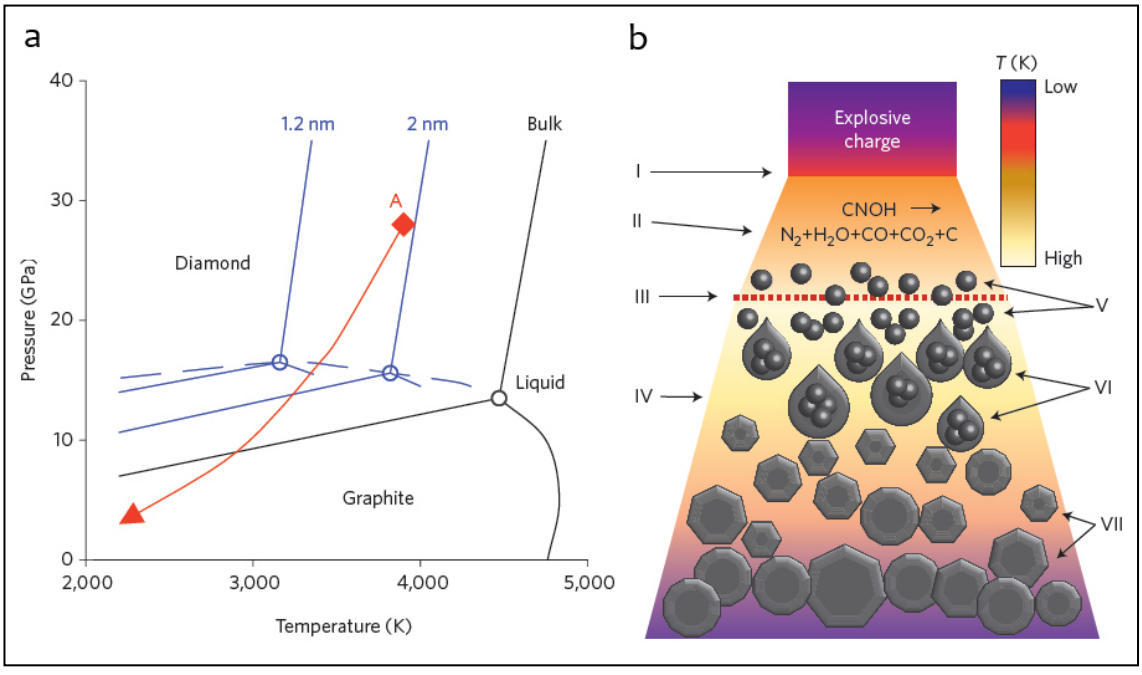

Figure 2.12: (a) the phase diagram for diamond/graphite formation, (b) schematic of the detention shockwave propagation (taken from Ref. 2.56)

2.3.3 Purification

In addition to the diamond phase, the diamond soot contains graphite-like structures (25-85 wt.%) and incombustible impurities (metals and their oxides – 1 to 8 wt.%).[259, 2.60] It is thus essential to remove these species in order to obtain the purest product for application purposes. X-ray diffraction and small angle X-ray scattering has shown than a UDD cluster in detonation soot has complex structure consisting of a diamond core of about 4.3nm in size and a shell made of sp^2 coordinated carbon atoms.[2.61]

The process of chemical isolation of the sp^3 hybridised carbon i.e. nanodiamond, from the detonation soot, substantially affects the properties of nanodiamonds. UDD purification is performed by mechanical and chemical methods. After mechanical removal of process admixtures, the diamond-carbonic powder is subjected to thermal oxidation with acid under pressure to separate the diamond phase.[2.62] Sulphuric acid, nitric acid or mixtures of these two acids are classically used.[2.63, 2.64] This is currently considered to be the best approach because it acts efficiently on all impurities; metals are dissolved and the non-diamond carbon is simultaneously oxidised.

Regarding the oxidation treatment necessary to remove sp^2 carbon species, other methods involve; thermal oxidation in air using boric anhydride to selectively oxidize the non-diamond carbon,[2.64] elimination of sp^2 carbon species by oxidising treatment at 425 °C under air in TGA apparatus [2.65] and gas phase treatment using ozone to purify nanodiamond from non-diamond carbon.[2.66]

Impurities embedded in nanodiamond aggregates are practically impossible to remove by wet chemistry. To minimize surface energy, the primary UDD particles with diameters of ~4 nm form larger clusters of 20 to 30 nm in size that in turn form larger, weakly bound aggregates of the order of order of one micron in size. The aggregates measuring approximately 100 nm, which have been coined 'core aggregates' are remarkably strong; it was found impossible to break up these aggregates into primary 4 nm sized diamond particles by ultrasound processing. Partial success in crushing the aggregates down to 40-60 nm grains was reached by subjecting the suspension to shock waves.[2.67] Although these aggregated samples may be useful in chromatography or drug delivery, in many applications

de-aggregation into individual primary particles is often needed to benefit fully from the advantages of nanodiamond.

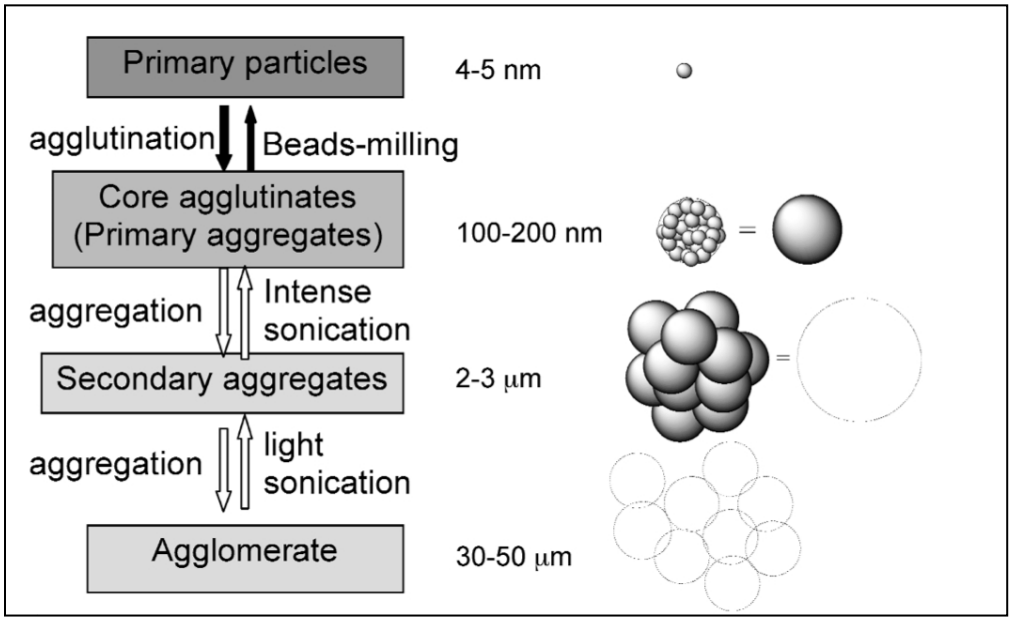

Figure 2.13: Hierarchical structure in conglomerates of commercial ND's based on the result of DLS analysis (taken from 2.71).

Eiji Osawa's work highlighted the problem of ND aggregation; his work recognised the existence of core agglutinates with 100-200 nm size and unusually tight binding. He found that even the most powerful sonicator failed to decompose core aggregates. He established that to free primary particles, the C-C bonds in the grain boundaries must be cleaved. The solution is wet milling with micron sized beads.[2.68]

After initial experiments to purify commercial samples of nanodiamond by removing the surface layers on non-diamond carbon atoms by strenuous oxidation, Osawa suspected that there might be domains in the ND powder where the oxidizing agent cannot penetrate. He therefore went back to the previous unproven statement that conventional sonication should lead to primary particles. Dynamic Light Scattering (DLS) measurements of the particle-size distribution were performed before and after a series of treatments. These experiments seemed to indicate complex hierarchical agglomeration structure in the commercial ND powder comprising three discrete modes of aggregation, each

mode holding component particles by different interparticle forces. The most important conclusion from these experiments is the recognition of core agglutinates which are 100-200 nm in size and the tight binding within these. The second breakthrough was the disintegration of these core agglutinates. To achieve this, wet milling with zirconia beads was applied. The resulting material is primary particles of detonation nanodiamond.

The DLS analysis of a typical colloidal solution obtained after the beads milling process (and removal of the small amount of coarse grains that remained uncrushed, by filtration and centrifugation), shows 99.94 wt.% of single nanoparticles of 4.6 ± 0.8 nm in diameter. When left standing in concentrations higher than about 8 %, the solution quickly solidifies to a soft gel, but can be readily turned back to smooth sol by adding small amounts of water. [2.69]

The mono dispersed detonation nanodiamond colloid is pitch black in colour but clear, from initially being a suspension of grey powder. This colour is attributed to the formation of graphitic patches on the surface of the primary particle by diamond-graphite transformation caused by the impact of shearing collision with beads.[2.70]

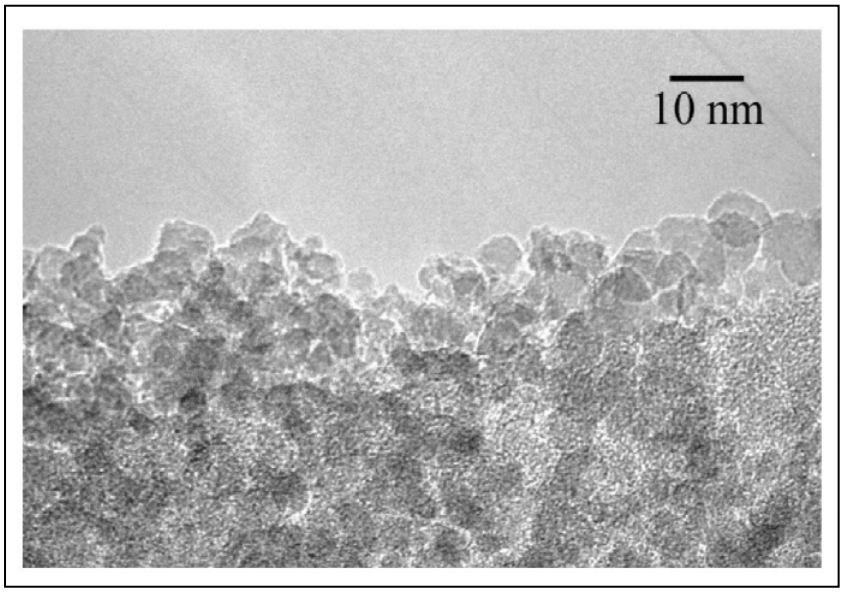

Figure 2.14: TEM of mono disperse primary detonation nanodiamond particles (from Ref. 2.71).

Another characteristic of monodispered primary ND particles is that their surfaces are highly polar. This polarity is thought to come from oxygen-containing functional groups especially carboxyl groups, C–H groups, and sp^2 (graphite) – sp^3 (diamond) interface, all known to be present on the surface of the primary ND particles. If oxygen atoms in water molecules are the counterpart of electrostatic interaction between these polar groups and water, then protons with partial positive charge will be directed to the outside in the non-freezing hydration shell. This surface polarity also gives rise to highly stable colloidal primary ND particles in water and also in some organic solvents like alcohols and dimethyl sulfoxide. Other novel features of monodispersed single digit nanodaimond particles, such as a high tendency toward self-organization, leading to spontaneous formation of whiskers, films, and fibres of nanodiamond from its colloid, and hydrogel formation, may be all related with localized polarity on the surface. The polarity may be changed and controlled by chemical modification or reconstruction of the surface as clear colloidal solution may be subjected to homogeneous reactions.[2.10] Recently Williams *et. al.* have shown that prior treatment of the particles by high temperature annealing in hydrogen gas can yield a monodisperse nanodiamond colloid with exceptional long time stability in a wide range of pH, and with high positive zeta potential (>60 mV).[2.72]

2.3.4 Functionalisation

The surface chemistry of nanodiamonds has been studied in considerable detail by NMR, TPD, XPS and FTIR spectroscopy.[2.73] The groups identified on the surface depend of the degree of chemical purification of the detonation charge; $C{=}CH_2$, $C{-}CH_2$, $O{=}CH_2$, O– CH as well as O-H groups. It has also been shown that the surface of oxidized NDs cleaned of detonation soot was covered to a large extent with different oxygen- containing groups, among them –COOH (carboxylic), –O–C=O (lactone), >C=O (carbonyl), –C–O–C– (ether) and –OH (hydroxyl). In such samples, the oxygen to surface carbon atom ratio was found to be close to 0.5.[2.11] These functional groups open up the possibilities for selective attachment of other functional groups and molecular fragments that can be produced on the diamond

surface. Thus, the ND surface reveals a broad spectrum of functional chemical groups with directly linked carbon structures.

The funcationalisation of nanoparticles creates surface functional molecular/ionic groups that can provide chemical or physical interaction of nanodiamond with organic molecules. This opens up vast possibilities for selective attachment of other functional groups and molecular fragments that can be produced on the diamond surface and used to advantage for the creation of various building blocks of nanostructures. Figure 2.14 displays the functional groups that can be realized by covalent surface modification. The rich surface chemistry and the absence of toxic impurities and small size make nanodiamonds a very convenient object for biomedical applications. The basic applications of nanodiamond surface functionalisation range from altering the wetting or adhesion characteristics and improving the nanoparticle dispersion in matrices to enhancing the catalytic properties. Partial graphitisation of the NDs suggests an additional way of modification of the diamond surface properties and synthesis of new nanographite/nanodiamond composites. Creation of specific surface sites on NDs for selective molecular attachment is considered a promising approach for their applications in nanofabrication, self- assembly, nanosensors, bioprobes, drug delivery, pigments, etc.

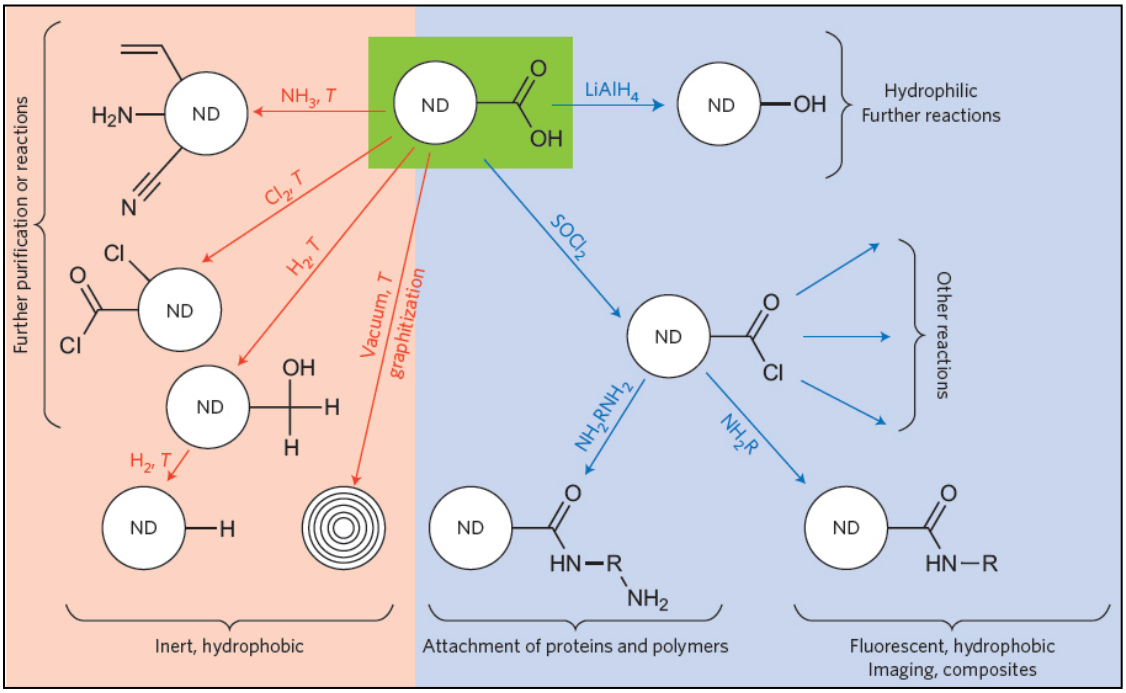

Figure 2.15: Nanodiamond terminated with carboxylic groups (ND–COOH; green region) is a common starting material. The surface of ND–COOH can be modified by high-temperature gas treatments (red) or ambient-temperature wet chemistry techniques (blue). Heating in NH3, for example, can result in the formation of a variety of different surface groups including NH2, C–O–H, C≡N and groups containing C=N . Treatment in H_2 completely reduces C=O to C–O–H and forms additional C–H groups. Hydroxyl (OH) groups may be removed at higher temperatures or with longer hydrogenation times, or by treatment in hydrogen plasma. Annealing in N_2, Ar or vacuum completely removes the functional groups and converts the nanodiamonds into graphitic carbon nano-onions. A wide range of surface groups and functionalized nanodiamonds can also be produced using wet chemistry treatments. (Taken from Ref. 2.56)

2.3.5 Properties and applications of nanodiamonds

Nanodiamond inherits many of the superior properties of bulk diamond and delivers them at the nanoscale. They can be used to provide a homogenous seeding layer for the chemical vapour deposition of diamond films as discussed in the previous section. The addition of diamond containing detonation soot has been shown to improve lubricants; decreasing fuel consumption and making engines last longer.[2.60]

The presence of nitrogen–vacancy (NV) centres — a nitrogen atom next to a vacancy — in nanodiamond leads to useful fluorescence properties. Fluorescent NV centres in isotopically clean diamond are of particular interest for quantum computing. NV centres in nanodiamond are also being investigated for applications in high-resolution magnetic sensing, fluorescence resonance energy transfer and biomedical imaging. Fluorescent particles can also be produced by linking [2.74] or adsorbing[2.75] various fluorophores onto nanodiamond. Fluorophore-conjugated nanodiamond can travel through cellular compartments of varying pH without degradation of the surface-conjugated fluorophore or alteration of cell viability over extended periods of time.[2.76] Bright blue fluorescent nanodiamond has been produced by covalent linking of octadecylamine to carboxylic groups on nanodiamond surface.[2.77]

The superior mechanical and thermal properties of diamond, combined with the rich surface chemistry of nanoscale diamond particles, make nanodiamond an excellent filler material for composites. Moreover, the biocompatibility and chemical stability of the diamond core make these composites very well suited for biomedical applications. Transparent poly (vinyl alcohol) nanocomposites with improved mechanical properties have been produced by adding small amounts of nanodiamond.[2.78]

Tissue engineering is an area of significant interest. The superior mechanical properties of nanodiamond, in combination with tunable surface chemistry, ability to deliver drugs and biologically active molecules, and biocompatibility, are beneficial for reinforcement of biodegradable polymers to create multifunctional tissue engineering scaffolds. One nanodiamond–polymer composite being explored for biomedical applications is ND–ODA–PLLA.* Although PLLA is biocompatible and bioresorbable, it is not mechanically robust for load bearing implants: however, the addition of well-dispersed ND–ODA leads to hardness and Young's modulus values that are close to those of human cortical bone.[2.79]

Nanodiamond has also shown to have applications in the field of drug delivery. The properties for a drug delivery platform include biocompatibility, the ability to carry a board range of therapeutics, dispersability in water and scalability.

* ND-ODA: Octadecylamine-functionalized nanodiamond.
PLLA: poly(L-lactic acid)

References

2.1 Michael Ströck (2006) *Allotropes of Carbon* [online] Available at: http://en.wikipedia.org/wiki/File:Eight_Allotropes_of_Carbon.png [Accessed on 31/11/2011]

2.2 H.O. Pierson, Handbook of Carbon, Graphite, Diamond and Fullerenes, Noyes, Park Ridge, NJ (1993). 3a. C. Y. Fong, B. M. Klein, in Diamond: electronic properties and applications, edited by Lawrence S. Pan, Don R. Kania Boston: Kluwer Academic, c1995.

2.3 L. Ladon, (2001) Hybridization of Carbon, Towson University [online] Available at:http://pages.towson.edu/ladon/carbon.html [Accessed on 31/11/2011]

2.4 Element Six (2001 – 2012) *Diamond Crystallography* [online] Available at:http://www.e6cvd.com/cvd/page.jsp?pageid=361 [Accessed on 31/11/2011]

2.5 G.S. Woods, Properties *and Growth of Diamond*, ed. G. Davies, INSPEC, London, UK (1994)

2.6 C.G. Zoski, *Handbook of Electrochemistry*, Elsevier B.V., 1st edition (2007)

2.7 F.B. Bundy, H.T. Hall, H.M. Strong, Jr. R.H. Wentorf, *Nature*, 176, 51-55 (1995).

2.8 H.O. Pierson, Handbook of Carbon, Graphite, Diamond and Fullerenes, Noyes, Park Ridge, NT (1993), 3a

2.9 F. P. Bundy, H. M. Strong, and R. H. Wentorf, Jr., *Chemistry and Physics of Carbon*, Vol. 10 (P. L., Walker, Jr. and P. A. Thrower, eds.), Marcel Dekker Inc. (1973).

2.10 Y. L. Orlov, *The Mineralogy of Diamond*, John Wiley & Sons, New York (1977).

2.11 Angus, J.C. (1994), *Development of Low-Pressure Diamond Growth in the United States, in Synthetic Diamond: Emerging CVD Science and Technology*, Spear, K.E. and Dismukes, J.P. (Eds.), JohnWiley & Sons, New York, 21-39.

2.12 Spitsyn B.V. and Deryagin B.V. (1980) USSR Patent 339.134 (author's certificate dated 10 July 1956)

2.13 S. Matsumoto, Y. Sato, M. Kamo and N. Setaka, *Japan Journal of Applied Physics*, 21 L183 (1982)

2.14 S. Matsumoto, Y. Sato, M. Tsutsumi and N. Setaka, *Journal of Materials Science*, 17, 3106 (1982)

2.15 M. Kamo, Y. Sato, S. Matsumoto and N. Setaka, *Journal of Crystal Growth*, 62, 642 (1983)

2.16 Y. Matsui, S. Matsumoto and N. Setaka, *Journal of Materials Science Letters*, 2532 (1993)

2.17 A. Sawabe and T. Inuzuka, *Applied Physics Letters*, 46 146 (1985)

2.18 K. Kitahama, K. Hirata, H. Nakamatsu, S. Kawai, N. Fujumori, T. Imai, H. Yoshino and A. Doi, *Applied Physics Letters*. 49 634 (1986)

2.19 S. Matsumoto, *Journal of Materials Science Letters*, 4 600 (1985)

2.20 M. Kamo, Sato Y, S. Matsumoto and N. Setaka, *Journal of Crystal Growth,* 62 642 (1983)

2.21 Y. Hirose, S. Ananuma, N. Okada and K. Komaki (1989) *1st Int. Symp. on Diamond and Diamond-like Films*, (Proceedings Vol 89–12), Ed J Dismukes (Pennington, NJ: The Electrochemical Society) pp 80–85

2.22 K. Kurihara, K. Dasaki, M. Kawarada and N Koshino, *Applied Physics Letters*, 52 437 (1988)

2.23 B. V. Derjaguin, and D. V Fedoseev, *Scientific American*, 233(5): 102- 109 (1975).

2.24 P.K. Bachmann, *Physics World*, Vol.32 (1991).

2.25 J. E. Butler, R. L. Woodin, L. M. Brown and P. Fallon, *Phil. Trans. R. Soc. Lond. A*, 342, 209-224 (1993).

2.26 J. J. Gracio1, Q. H. Fan and J. C. Madaleno, *Journal of Physics D: Applied Physics*. 43 374017: 22 (2010).

2.27 M. P. D'Evelyn, C. J. Chu, R. H. Hange, and J. L. Margrave, *Journal of Applied Physics*, 71(3):1528-1530 (1992).

2.28 C. J. Chu, M. P. D'Evelyn, R. H. Hauge, and J. L. Margrave, *Journal of Applied Physics*, 70(3):1695-1705 (1991).

2.29 Z.M. Zhang, H.M. Cheng, S.H. Li, Q.Y. Cai, D.L. Ling, S.J. Wang, Z.W.Hu, S.S. Jiang, C.Z. Ge, and N.B. Ming, *Journal of Crystal Growth*, 132(1-2):200-204 (1993)

2.30 S.Katsumata, *Japan Journal of Applied Physics*, 31(11):3594-3597 (1992).

2.31 M. Komori, T. Maki, T. Kim, G. Hou, Y. Sakaguchi, K. Sakuta, and T. Kobayashi, *Applied Physics Letters,* 62(6):582-584 (1993).

2.32 Y. Mitsuda, Y. Kojima, T. Yoshida and K. Akashi, *Journal of Materials Science*. 22, 1557 (1987)

2.33 P. Ascarelli, and S. Fontana, *Applied Surface Science*, 64(4):307- 311 (1993).

2.34 E. Scorsone, S. Saada, J. C. Arnault, P Bergonzo, *Journal of Applied Physics*, 106, 014908 (2009)

2.35 M Daenen, L. Zhang, R. Erni, O. A. Williams, A. Hardy, M.K Van Bael. , P. Wagner, K. Haenen, M. Nesladek, G.V. Tendeloo, *Advanced Materials*, 21, 670–673 (2009).

2.36 H.A. Girard, S. Perruchas, C. Gesset, M. Chaigneau, L. Vieille, J.-C. Arnault, P. Bergonzo, J.-P. Boilot, T. Gacoin, *Applied Materials and Interfaces*, 1, (12): 2738–2746 (2009).

2.37 D.M. Gruen, *Annual Review of Materials Science*, 29, 211 (1999)

2.38 O.A. Williams, M. Nesladek, M. Daenen, S. Michaelson, A. Hoffman E. Osawa e, K. Haenen, R.B. Jackman, *Diamond & Related Materials*, 17, 1080–1088(2008)

2.39 J.C. Angus, (1994), *Development of Low-Pressure Diamond Growth in the United States, in Synthetic Diamond: Emerging CVD Science and Technology*, Spear, K.E. and Dismukes, J.P. (Eds.), John Wiley & Sons, New York, 21-39.

2.40 J.J. Gracio, Q.H. Fan and J.C. Madaleno *Journal of Physics D: Applied Physics*, 43, 374017 (2010)

2.41 M. Hiramatsu and M. Hori, (2010) *Carbon Nanowalls: Synthesis and Emerging Applications*, Springer

2.42 K.H.J. Buschow, R.W. Cahn, M.C. Flemings, B. Ilschner, E.J. Kramer, S. Mahajan, *Encyclopedia of Materials - Science and Technology*, Volumes 1- 11, Elsevier, (2001)

2.43 S. A. Kajihara, A. Antonelli, J. Bernholc and R. Car, *Physical Review Letters*, 66 2010 (1991).

2.44 F. Fontaine, C. Uzan-Saguy, B. Philosoph and R. Kalish, *Applied Physics Letters,* 68, 16 (1996).

2.45 H. Gerischer, in *Physical Chemistry*, edited by H. Eyring (Academic Press, New York), Vol. IX A, p. 463 (1970)

2.46 F. Maier, M. Riedel, B. Mantel, J. Ristein, and L. Ley*, Physical Review Letters*, 85, 16 (2000).

2.47 N. Fujimori, *New Diamond*, 2(2):10-15 (1988).

2.48 A. Vescan, I. Daumiller, P. Gluche and W. Ebert, *Diamond and Related Mater*ials 7, 581 (1998).

2.49 A. Aleksov, A. Denisenko, M. Kunze, A. Vescan, A. Bergmaier, G. Dollinger, W. Ebert and E. Kohn, *Semicond. Sci. Technol*. 18, S59-S66 (2003).

2.50 A. Aleksov, A. Denisenko and E. Kohn, *Solid-State Electron*. 44, 369–375 (2000).

2.51 H.Umezawa, T. Arima, N. Fujihara, H. Taniuchi, H. Ishizaka, C. Wild, P. Koidl and H. Kawarada, *Japan Journal of Applied Physics*, 41, 2611 (2002).

2.52 M.W. Geis, N.N. Efremow, J.D. Woodhouse, M.D. McAleese, M. Marchywka, D.G. Socker, *IEEE Electron Device Letters*, 12, 8, 456, (1991).

2.53 G. W Yang, J. B Wang & Q. X. Liu, *Journal of Physics: Condensed Matter*, 10, 7923–7927 (1998)

2.54 J.P. Boudou *et al*., *Nanotechnology* 20, 235602 (2009).

2.55 M. Frenklach, W. Howard, D. Huang, J. Yuan, K.E. Spear and R. Koba, *Applied Physics Letters*, 59, 546–548 (1991).

2.56 V. N. Mochalin, O. Shenderova, D. Ho, and Y. Gogotsi The properties and applications of nanodiamonds, Published Online: 18 December 2011 | DOI: 10.1038/NNANO.2011.209

2.57 F. H. Ree, N. W. Winter, J. A. Viecelli, *Physica B*, 265, 223 (1999).

2.58 J. A. Viecelli, S. Bastea, J. N. Glosli, and F. H. Ree. *Journal of Chemical Physics*, 115, 2730–2736 (2001).

2.59 S. Osswald, G. Yushin, V. Mochalin, S. Kucheyev, Y. Gogotsi, *J. American Chemical Society,* 128, 11635-11642 (2006)

2.60 V. Y. Dolmatov, *Detonation synthesis ultradispersed diamonds: Properties and applications*. Usp. Khim. 70, 687–708 (2001).

2.61 A.E Aleksenskii, M.V. Baidakova, A.Y. Vul', and V.I. Siklitskii, *Physics of the Solid State*, 41, 668–671, (1999).

2.62 V. Y. Dolmatov, *Russian Chemical Reviews,* 70**,** 607– 626 (2001)

2.63 V. Y. Dolmatov, M.V. Veretennikova, V.A. Marchukov, V.G. Sushchev, *Physics of the Solid State*, 46 (4) 611 (2004).

2.64 A.S. Chiganov, *Phys. Solid State* 46 (4) 620 (2004)

2.65 O. Shenderova, I. Petrov, J. Walsh, V. Grichko, T. Tyler, G. Cunningham *Diamond and Related Materials*, 15, 1799 (2006)

2.66 I. Petrov In: D. Gruen *et al.*, Editors, *Ultrananocrystalline Diamond: Synthesis, Properties and Applications*, NATO Science Series, Springer (2005), p. 333.

2.67 A. Ya. Vul, A. T. Dideĭkin, Z. G. Tsareva, M. N. Korytov, P. N. Brunkov, B. G. Zhukov and S. I. Rozov, *Technical Physics Letters,* 32 (7): 561 (2006).

2.68 A. Krüger, F. Kataoka, M. Ozawa, A. Aksenskii, A. Ya. Vul', Y. Fjino, A. Suzuki, E. Ōsawa. *Carbon* 43, 1722 (2005)

2.69 E. Ōsawa. *NCRI Tech. Bull.*, No. 3, 1–6 (2007) (see <http://nano carbon.com>)

2.70 E.D. Eidelman, V.I. Siklitsky, L.V. Sharonova, M.A. Yagovkina, A. Ya Vul', M.Takahashi, M. Inakuma, M. Ozawa, E. Osawa, *Diamond and Related Materials*, 14, 1765-1769 (2005).

2.71 E. Osawa, *Pure Applied Chemistry,* 80, (7):1365–1379, (2008).

2.72 O.A. Williams, J. Hees, C. Dieker, W. Jager, L. Kirste, C.E. Nebel, *ACS Nano,* 4 (8) 4824 (2010).

2.73 M. Baidakova and A. Vul', *Journal of Physics D: Applied Physics*, 40, 6300–6311 (2007)

2.74 S. C. Hens, G. Cunningham, T. Tyler and O. Shenderova, *Diamond and Related Materials*, 17, 1858–1866 (2008)

2.75 L.C.L. Huang, H.C. Chang, *Langmuir* 2, 5879-5884 (2004).

2.76 A.M. Schrand, J.B. Lin, S.C. Hens, and S.M. Hussain, *Nanoscale*, 3, 435–445 (2011).

2.77 V.N. Mochalin and Y. Gogotsi, *Journal of the American Chemical Society*, 131, 4594–4595 (2009).

2.78 S. Morimune, M. Kotera, T. Nishino, K. Goto and K. Hata, *Macromolecules*, 44, 4415–4421 (2011).

2.79 Q. Zhang, V.N. Mochalin, I. Neitzel, I.Y. Knoke, J. Han, C.A. Klug, J.G. Zhou, P.I. Lelkes, Y. Gogotsi, *Biomaterials*, 32, (1): 87-94 (2011).

Chapter 3 Photomultiplication

Chapter 3 presents some of the basic theory behind photomultiplier devices and secondary electron emission, ending with a review of diamond as a secondary electron emitter and its application to image intensifiers.

3.1 Photomultiplier Tubes

Photomultiplier (PM) tubes convert light signals consisting of no more than a few hundred photons into a usable current pulse without adding a large amount of random noise to the signal. Two major components inside the tube are a photosensitive layer, called the photocathode, coupled to an electron multiplier structure.

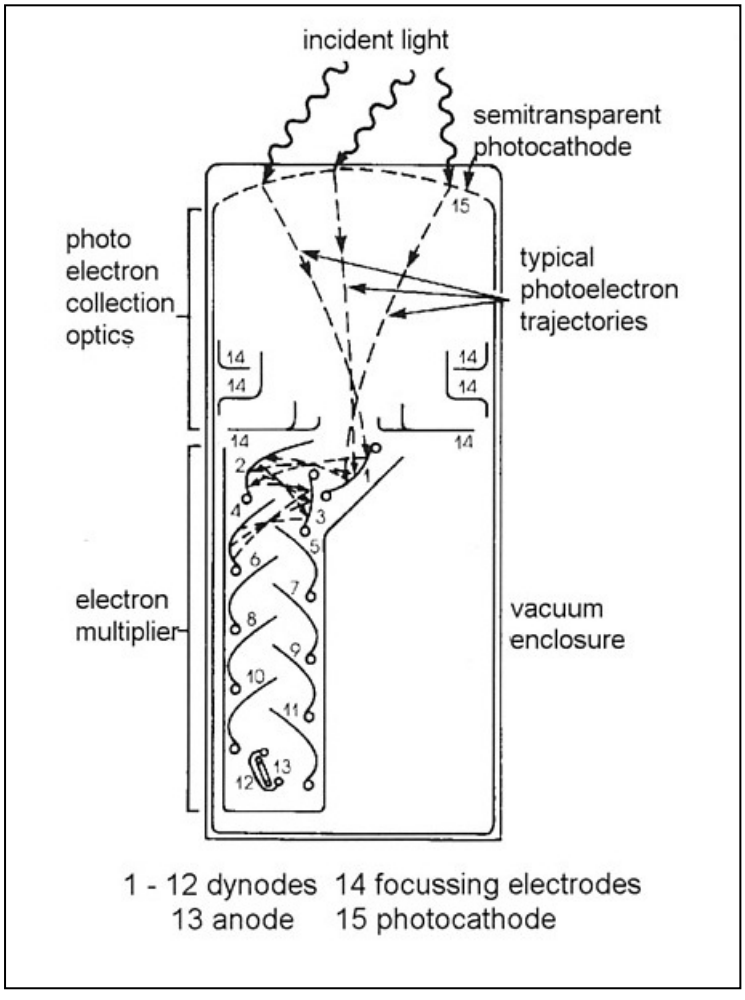

Figure 3.1: Basic elements of a PM tube (taken from Ref. 3.1)

The photocathode serves to convert as many of the incident light photons as possible into low-energy electrons. The electron multiplier section in a PM tube provides an efficient collection geometry for the photoelectrons as well as servicing as a near-ideal amplifier to greatly increase their number. After amplification through the multiplier structure, a typical scintillation pulse will give rise to 10^7-10^{10} electrons, sufficient to serve as the charge signal for the original scintillation event. This charge is conventionally collected at the anode or output stage of the multiplier structure. Most photomultipliers perform this charge amplification in a very linear manner, producing an output pulse at the anode that remains proportional to the number of original photoelectrons over a wide range of amplitude.

3.1.1 The Photocathode

The first step to be performed by the PM tube is the conversion of incident light photons into electrons. The energy that can be transferred from the photon to an electron during the absorption of the incident photon within the material is given by the quantum energy of the photon, *hv*. Some energy will then be lost in electron-electron collisions in the migration process. Finally, there must be sufficient energy left for the electron to overcome the potential barrier between the material and vacuum (material work function). The rate of energy loss as the electrons migrate to the surface should be kept small in order to maximise the depth in the material at which electrons may originate and still reach the surface with sufficient energy to overcome the potential barrier (escape depth).

In order for an incident light photon to be absorbed in a semiconductor, its energy must exceed the bandgap energy E_g of the material. The absorption process simply consists of elevating an electron from the valence band to the conduction band. In normal semiconductors, the electron potential outside the surface is higher than the bottom of the conduction band by an amount called the *electron affinity*. If an electron is to escape, it must reach the surface before phonon interactions reduce its energy to the bottom of the conduction band.

3.1.2 Secondary Electron Emission

The multiplier portion of a PM tube is based on the phenomenon of secondary electron emission. Secondary emission is a phenomenon where additional electrons, called secondary electrons, are emitted from the surface of a material when an incident particle (often, a charged particle such as electron or ion) impacts the material with sufficient energy. Electrons from the photocathode are accelerated and caused to strike the surface of an electrode, called a dynode. The energy deposited by the incident electron on the dynode can result in the reemission of more than one electron from the same surface.

The secondary electron yield is a sensitive function of incident electron energy. If a relatively low-energy electron strikes the dynode surface, little energy is available for transfer to electrons in the dynode material, and relatively few electrons will be excited across the gap between the valence and conduction bands. At the same time, because the distance of penetration is not large, most of these excited electrons will be formed near the surface. For incident electronics of a higher energy, more excited electrons will be created within the dynode by at a greater average depth. Because the probability of escape will diminish with increasing depth, the observed electron yield with be maximised at an optimum incident electron energy.

The overall multiplication factor for a single dynode is given by,

$$\delta = \frac{\text{number of secondary electrons emitted}}{\text{primary incident electron}} \qquad \text{(eq. 3.1)}$$

and should be as large as possible for maximum amplification per stage in the photomultiplier tube.

Figure 3.2 illustrates the secondary electron emission process using a three-step model:[3.2] [1] generation of the internal secondary electrons by kinetic impact of the primary electrons, [2] transmission of the internal secondary electrons through the material and [3] escape of the secondary electrons over the vacuum barrier. The presence of dopants in the material influences the secondary electron yield by affecting the transmission process (step 2), while the influence of the surface affects the escape process (step 3).

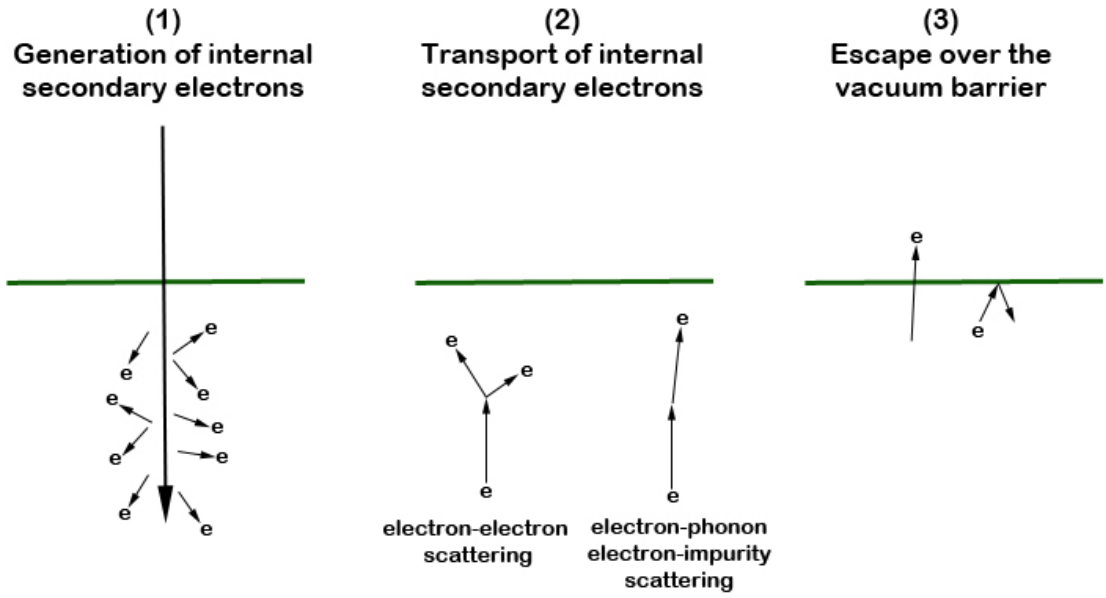

Figure 3.2: A three-step model of the secondary-electron-emission process (reproduced from Ref. 3.3)

3.1.3 Negative Electron Affinity Materials

The secondary emission yield of dynodes can be increased significantly through the use of negative electron affinity (NEA) materials. NEA materials lead to a much greater escape depth by allowing electrons that have dropped to the bottom of the conduction band to also escape if they reach the surface. The electron affinity of a semiconductor is defined as the energy required to remove an electron from the conduction band minimum to a distance macroscopically far from the semiconductor. This energy may be schematically shown as the difference between the vacuum level and the conduction band minimum (CBM). In a typical band scheme of a semiconductor, the vacuum level lies above the CBM and creates an energy barrier, χ, the electron affinity. If the vacuum level was to lie below the CBM then $\chi < 0$ and a NEA surface is produced. The electron affinity or work function of a material is usually ascribed to two aspects of the material; the origin of the atomic levels, or the surface dipole due to surface termination.

The surface dipole can be substantially affected by surface reconstructions and surface adsorbates. It has been established that electrons excited by photons into

the conduction band of p-type diamond can, provided the surface has been prepared appropriately, find themselves at a higher energy than the vacuum level,[3.4, 3.5] i.e. NEA prevails. As anticipated, these electrons do move out into the vacuum without encountering an energy barrier. The most commonly used surface treatment is to hydrogenate a (111), p-type diamond surface. Quantitative evidence now exists that it is the dipole character of the C-H bonds on the surface that causes this NEA behaviour.[3.6]

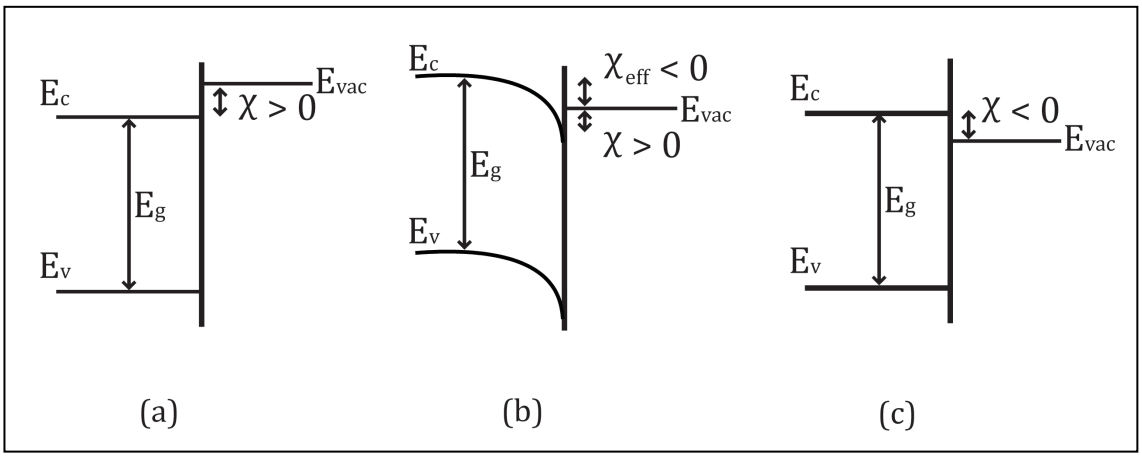

Figure 3.3: Energy band diagram of diamond surfaces (a) Positive Electron Affinity (b) Effective Negative Electron Affinity (c) True Negative Electron Affinity.

The energy band diagrams of a positive electron affinity (PEA), effective negative electron affinity (NEA) and a true NEA diamond surfaces are shown in Figure 3.3 (a-c), respectively. The electron affinity of diamond depends on the amount of hydrogen present. If the surface of the diamond is completely free of hydrogen, the net electron affinity is positive, resulting in a potential barrier between the diamond-vacuum interface. When the diamond surface is hydrogenated a positive dipole is induced which results in the band bending and correspondingly a smaller electron affinity value than the previous case. In that case, the surface of the diamond will have an effective NEA where the highest level of the conduction band edge is above the vacuum level while the lowest level of the conduction band edge bends below the vacuum level (Figure 3.3(b)). In Figure 3.3(c), the energy band diagram of a true NEA surface of diamond is shown. As the conduction band is above the vacuum level, the net barrier height is negative and therefore, electrons can easily flow from the conduction band to the vacuum level without any

potential drop. A diamond NEA surface can also be produced by depositing a monolayer surface of caesium upon oxygen terminated diamond. Through band bending, the vacuum level is forced below the CBM. The resulting surface is in fact metallic due to Cs-O-C surface states and thereby also provides a low work function.

3.2 Secondary electron emission in diamond

In 1992, Dr. Gerald Mearini, Dr. Isay Krainsky, and Dr. James Dayton made a secondary electron emission discovery that laboratory-grown diamond films could produce up to 45 electrons from a single incident electron, making diamond an excellent electron emitter.[3.7] Diamond surfaces with negative electron affinity provide an easy path for escaping electrons. The diffusion length for these electrons depends on the crystalline quality. In order to avoid charging effects, diamond films need to be electrically conductive, too.

N-doped diamond samples are insulators. However, electrical conductivity is needed to sustain the secondary electron emission process, otherwise sample charging results. If $\delta > 1$, the sample becomes positively charged, resulting in an increased vacuum barrier height and a decreased yield. If $\delta < 1$, the samples becomes negatively charged, resulting in a slow down or even repulsion of the impinging electrons. With a perfect insulator $I_s = I_o$ † and $\delta = 1$. δ_{max} was measured to be 1.06 ± 0.04 from an N-doped CVD diamond sample.[3.8]

Boron doped diamond is electrically conductive and has a high δ when it is terminated with hydrogen or caesium due to the creation of a NEA surface. For H-terminated diamond samples, both Miller *et al.*[3.9] and Shih *et al.*[3.10] found that the secondary electron yields are sensitive to the B-doping level. In fact there is an optimum rage of boron concentrations for high secondary electron yields. δ decreases at low B-doping levels due to the insufficient electrical conductivity required to sustain high secondary electron emission levels. However, B dopants are also sources for electron collisions which can suppress the yield if the doping concentration becomes too high. Specifically, most of the internal secondary

† I_s is the secondary electron intensity, I_o is the primary electron intensity and $\delta = (I_s/I_p)$ and varies with primary electron energy.

electrons in diamond have kinetic energies of about 1 eV. These low-energy electrons are unable to excite valence electrons over the 5.47 eV bandgap and collisions with phonons and impurities become a major source of energy loss. As the doping concentration increases, the collision rate increases and the electron escape depth decreases, resulting in lower electron emission. Boron doped and hydrogen terminated diamond is a good candidate for high-yield secondary electron emitter applications.

3.2.1 Secondary electron yield curves

The emission probability at a NEA surface is assumed to be independent of electron energy; therefore the measured yield is affected by the generation process (i.e. number of generated electrons) and by the transport process (i.e. percentage of generated electrons reaching the surface). The number of generated electrons increases proportionally with the incident beam energy, E_b, because the number of possible impact-ionisation events increases as E_b increases and therefore number of impact-ionised electrons increases. However, the number of electrons reaching the surface depends on the electron generation depth, D_g, and the electron escape depth, D_{esc}. While D_g increases with E_b, D_{esc} is a property of the material and is independent of E_b. For the low-energy electrons that dominate the emission measurements, D_{esc} is primarily limited by electron-hole recombination and capture by electron traps. The shape of the yield curve reflects the changes in the electron generation and escape processes as E_b increases, with yield curves typically exhibiting three regimes and having a bell shape as seen in figure 3.3.[3.11] For low values of E_b, the electron penetration depth is very small so that $D_g < D_{esc}$ and the electrons can readily escape. Thus, the yield initially increases with increasing E_b (regime 1) as the number of generated electrons increases. For high values of E_b, the electron penetration depth is much larger so that $D_g > D_{esc}$. Thus, the yield decreases with increasing E_b (regime 3) since increasing numbers of electrons are captured in the material as D_g increases. In between these two regimes, the yield reaches a maximum (regime 2) at an energy $E_b = E_{max}$ for which the condition $D_g \sim D_{esc}$ is satisfied.

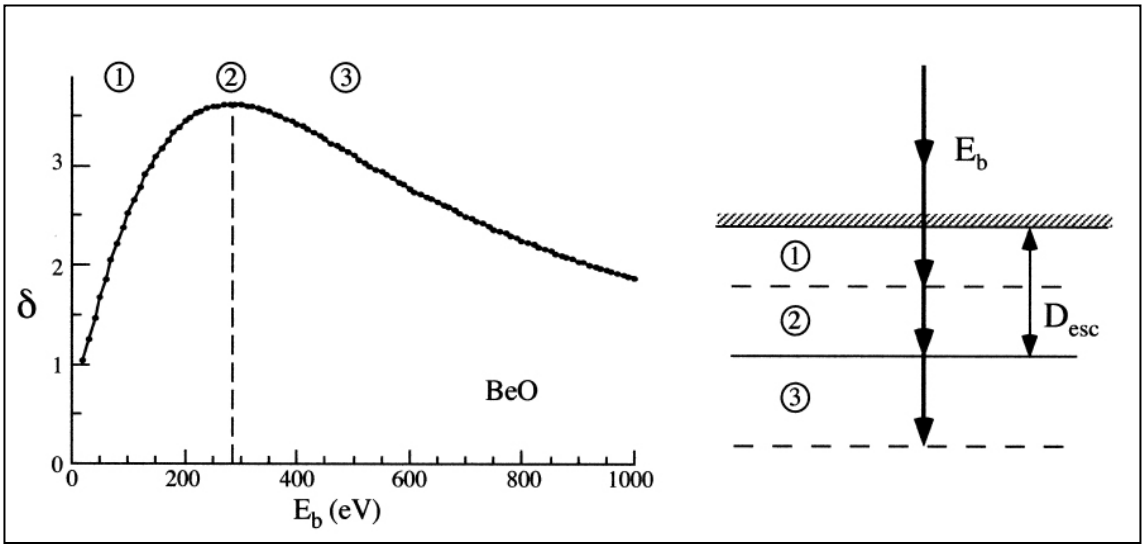

Figure 3.4: A typical bell-shaped secondary electron yield curve (measured from BeO) obtained with increasing impact energy and penetration depth of the incident electron beam. δ = secondary emission yield (taken from Ref. 3.12).

3.2.2 Secondary electron emission studies in boron doped films

H-termination of diamond is essential for the low electron affinity of diamond as discussed in the previous section and is consequently crucial to the high secondary electron yield. Figure 3.5 shows the secondary electron yield curve of a hydrogen terminated boron doped diamond sample. The sample was heated to 1000 °C for 15 min to desorb a large fraction of the surface hydrogen resulting in a huge decrease of the secondary electron yield. Accompanying the hydrogen desorption, the vacuum barrier height increases by about 1.45 eV and is too high for the quasi-thermalised electrons to escape.[3.13]

The authors introduced B impurities in to the CVD diamond to provide the required electrical conductivity. Since electron-phonon and electron-impurity scatterings are the main energy-loss mechanisms for the low-energy secondary electrons, an excessively high impurity concentration may reduce the escape depth and the yield. Figure 3.6 compares the yield curves taken on diamond samples with different B-doping levels. The higher yield curves are typical for low or moderately B-doped diamond samples which have a resistivity between 50-170 kΩ cm and are transparent. The lower yield curve is taken from the highly B-doped

sample which appears black and opaque and has a resistivity between 50-170 Ω cm. In this case, too high a boron concentration actually reduces the yield as predicted.

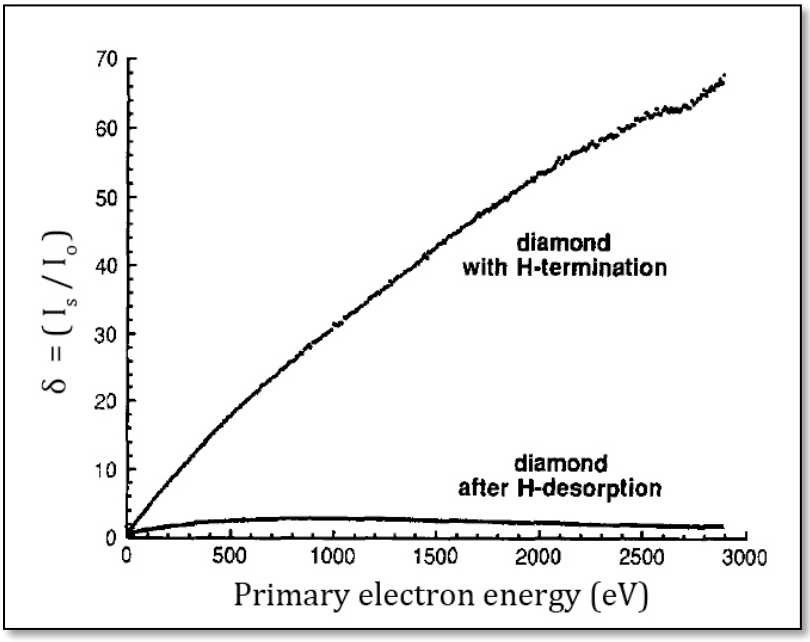

Figure 3.5: A large reduction in the secondary-electron yield from diamond occurs with hydrogen desorption (taken from Ref. 3.13)

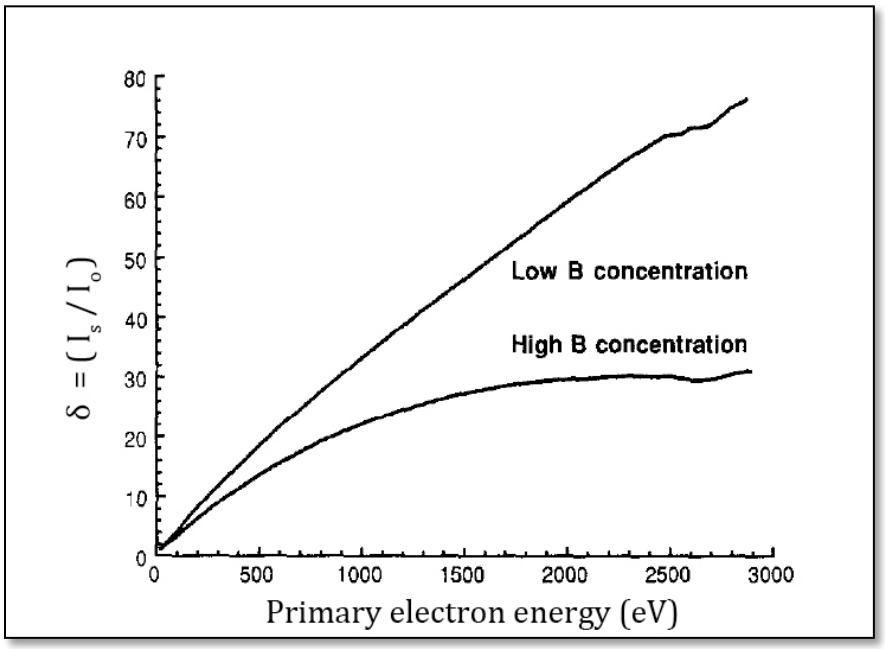

Figure 3.6: Effect of the B impurity level on the secondary electron yield from diamond (taken from Ref. 3.13)

3.2.3 SEY from bare and caesiated, natural and CVD diamond

Shortly after, Yater *et al.*[3.12] published a comparison of C (100) (natural IIb) and CVD diamond (boron doped) samples in both 'bare' surface condition and coated with caesium. The 'bare' surfaces were thermally cleaned under the vacuum conditions. Secondary electron yield curves were obtained for both samples. The secondary electrons are defined to include all emitted electrons, with energy up to E_b, produced by the incident electron beam. Therefore, the secondary electron yield coefficient δ is defined as the ratio of the total emitted electron intensity to the incident electron intensity. This parameter thus represents the average number of emitted electrons per incident electron. The data is presented as secondary electron yield curves where δ is plotted as a function of E_b between 0 and 2900 eV.

The measurements of secondary emission yield were made in a straightforward manner as described in earlier literature.[3.14] With the sample kept at a negative voltage to repel the emitted electrons, the measured sample current is the net current I_{net}, which is the difference between the secondary emitted current I_s, and the incident beam current I_B. I_B was measured with the aid of a Faraday cage. Thus the secondary emission coefficient;

$$\delta = \frac{I_S}{I_B} = \frac{I_{net} + I_B}{I_B} \qquad \text{(eq. 3.2)}$$

The secondary electron emission is tremendously enhanced at the cesiated NEA surfaces and the overall yields are extremely high. Specifically, the highest measured yield increases from **δ ~** 3 at the bare diamond surfaces to **δ ~** 132 and 83 at the caesiated C(100) and CVD diamond surfaces, respectively.

At the bare diamond surface, E_{vac} lies above the peak position in the energy distribution and consequently most of the low-energy secondary electrons remain trapped in the diamond. After caesiating the diamond surface, the vacuum barrier is removed and the large number of low-energy electrons contained in the sharp peak is emitted into vacuum, resulting in a large increase in the measured yield.

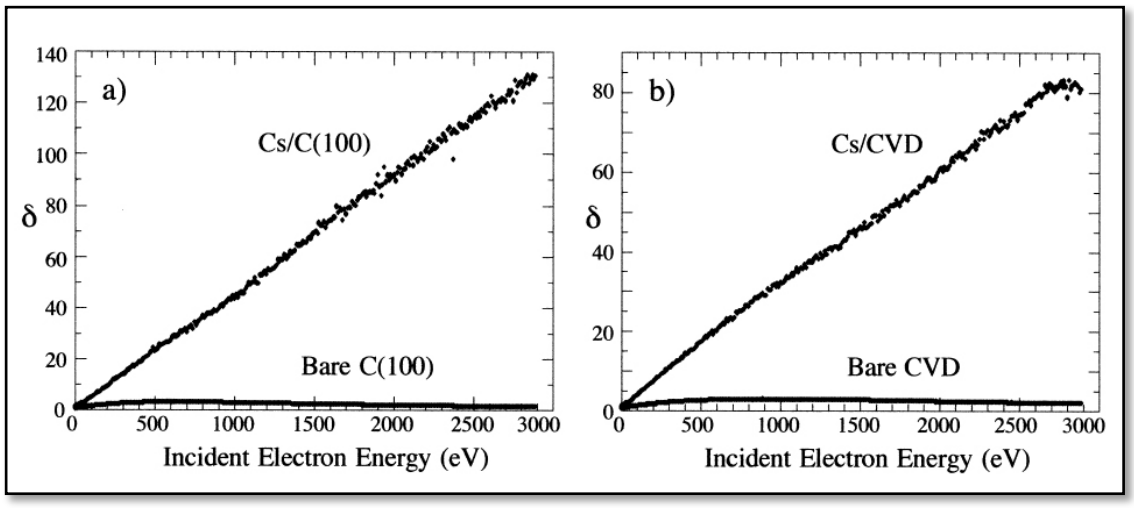

Figure 3.7: Secondary electron yield curves for E_b =0 - 2900 eV measured from bare and caesiated surfaces of (1) the C(100) sample and (b) the CVD diamond sample. At the bare C (100) and CVD surfaces δ_{max} = 3 at E_b ~ 650 eV and 900 eV respectively (from 3.12).

3.2.4 Secondary electron amplification using single-crystal CVD diamond film

Recently, Yater *et al.* reported on the current amplification characteristics of an unbiased 8.3 μm thick single-crystal diamond film.[3.15] Previous measurements were obtained in a reflection configuration in which electron impact and emission occurred at the same surface. Therefore, the actual secondary-electron transport distances were relatively short (≤ 0.1 μm) due to the limited penetration depth of the primary electrons with an incident energy (E_o) ≤ 3 keV. Diamond has predicted long escape depths (≥ 5 μm in (100) diamond), in order to confirm this, the secondary electrons must be generated at greater distances from the emitted surface. This can be accomplished by increasing E_o, which results in deeper primary electron penetration. Therefore, the authors use a transmission configuration whereby high-energy electrons are injected into the back side of the diamond, such that the hydrogenated front surface is not impacted – which would risk electron-induced surfaces modification at higher E_o.

In previous studies using this same approach, the authors directed an electron beam at the back surface of thin (0.15–2.5 μm) polycrystalline diamond films and then studied the transmission of secondary electrons through the films.[3.16] In these studies, electron transmission was detected when electrons were generated within

~1.3 μm of the emitting surface, in good agreement with the predicted escape depth in polycrystalline diamond. However, the transmission gains were substantially lower (<5) than the reflection gains. The authors attributed this low transmission gain to be most likely due to increased electron scattering at grain boundaries as well as low diffusive-transport efficiency over the longer transport distances.[3.17] Therefore, it is proposed that the use of single-crystal diamond *and* an internal electric field are necessary to achieve the high transport efficiency needed for high-gain current amplification (e.g., gain ~100).

Compared to the authors previous transmission measurements from polycrystalline diamond, the single-crystal diamond film has a substantially longer diffusion length (8.1 μm vs 1.3 μm), and comparable transmission gain (~3–4) in spite of the larger film thickness (8.3 μm vs 2.5 μm). These measurements indicate that there is not a significant problem with the transport or surface properties of the diamond material itself. The long transport distance achieved indicates the potential for excellent electron transport capabilities. The transmission gain is being limited by diffusion-limited transport in the film. Thus, the transport efficiency must be improved by applying a bias across the film to generate an internal field.

The distinctive transmission peak is observed even at E_o = 5 keV, which corresponds to a penetration depth of ~0.2 μm and therefore a transport distance of more than 8 μm. Such a long transport distance is consistent with the predicted (≥5 μm) escape depth in (100) diamond that was deduced from the author's previous reflection measurements.

3.3 Night Vision Devices

The current generation of night vision devices is based on the use of image intensifiers. An image intensifier is a vacuum tube that amplifies a low light-level scene to observable levels. The object lens collects light and focuses it onto the image intensifier. At the photocathode of the image intensifier the incoming light is converted into photo-electrons. These photo-electrons are accelerated in an electric field and multiplied by a micro channel plate. Subsequently the highly intensified photo-electrons strike the phosphor screen and a bright image is

emitted that you can see.

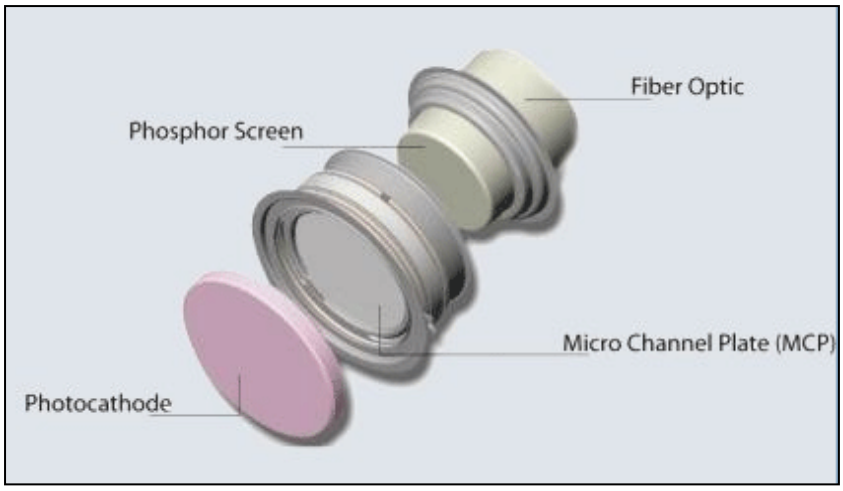

Figure 3.8: Components of a night vision device (taken from Ref. 3.18)

Figure 3.8 shows the components of the image intensifier from the industrial collaborators of this work, Photonis SAS. The photocathode is the input surface of an image intensifier; the theory behind its operation is described in chapter 3.1.1. The type of photocathode material used is a distinguishing characteristic of the generations of image intensifiers. The microchannel plate is a metal coated (typically nickel-chromium or only chromium that acts as the electrodes) glass disc that multiples the electrons produced by the photocathode. The number of holes in an MCP is a major factor in determining resolution. Photonis SAS produces MCP's with 11 million pores. The phosphor screen converts electrons into photons. A very thin layer of phosphor is applied to the output fibre optic system, and emits light when struck by electrons.

3.3.1 Microchannel plate (MCP)

A type of specialised electron multiplier is the continuous channel. This device is extremely simple, consisting of a hollow glass tube whose inner surface acts as a secondary electron emitter. Channel multipliers must be shaped to prevent feedback problems that can arise when positive ions occasionally formed within the channel are accelerated in the reverse direction from the electrons. By forming the channel as a curve or chevron, these ions can be made to strike a wall before

their energy is enough to create secondary electrons. Clusters of many thousands of tubes can be fabricated to form a *microchannel plate*. Each channel is of very small diameter (typically 15-50 μm) and acts as an independent electron multiplier. MCPs are made from highly resistive material with a thickness of typically 2 mm. MCP detectors are extensively used to detect and image individual particles such as photons, electrons, and ions. Currently the main material for MCP production is lead-silicate glass. Figure 3.9 shows a digitally rendered image of an MCP and Figure 3.10 shows a schematic diagram of an MCP.

A gain is achieved by applying a voltage of approximately 1 kV across the electrodes. A typical MCP has a resistance of 100 MΩ. A voltage of 1 kV results in a typical current of 10 μA. This is called a strip current. The current distributes the voltage evenly along the channel. When the input of the channel is hit by a photoelectron, it will create a few secondary electrons. The field inside the channel will accelerate these electrons in the direction of the output. After the secondary electrons have gained sufficient kinetic energy, they will colloid again with the wall, creating more secondary electrons. This process repeats itself like an avalanche until a cloud of electrons leaves the channel. The device acts much like a photomultiplier tube with continuous dynodes available along its entire length.

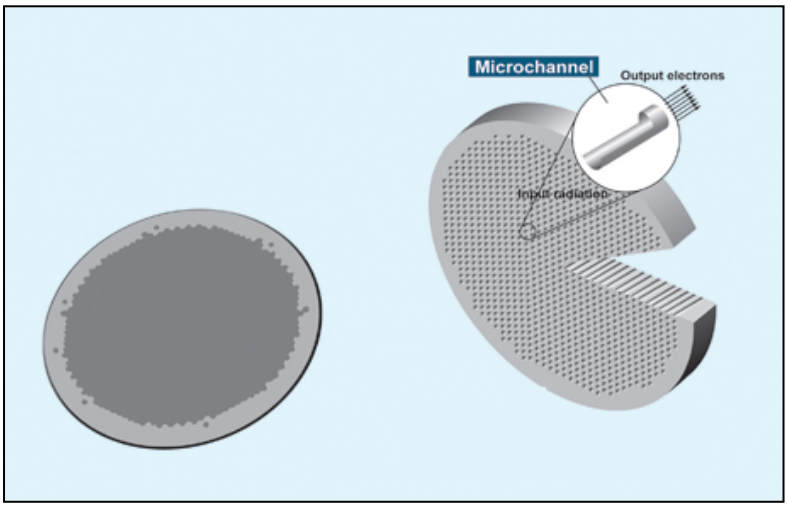

Figure 3.9: A digitally rendered image of an MCP (left) with the channels depicted on the right (taken from Ref. 3.19).

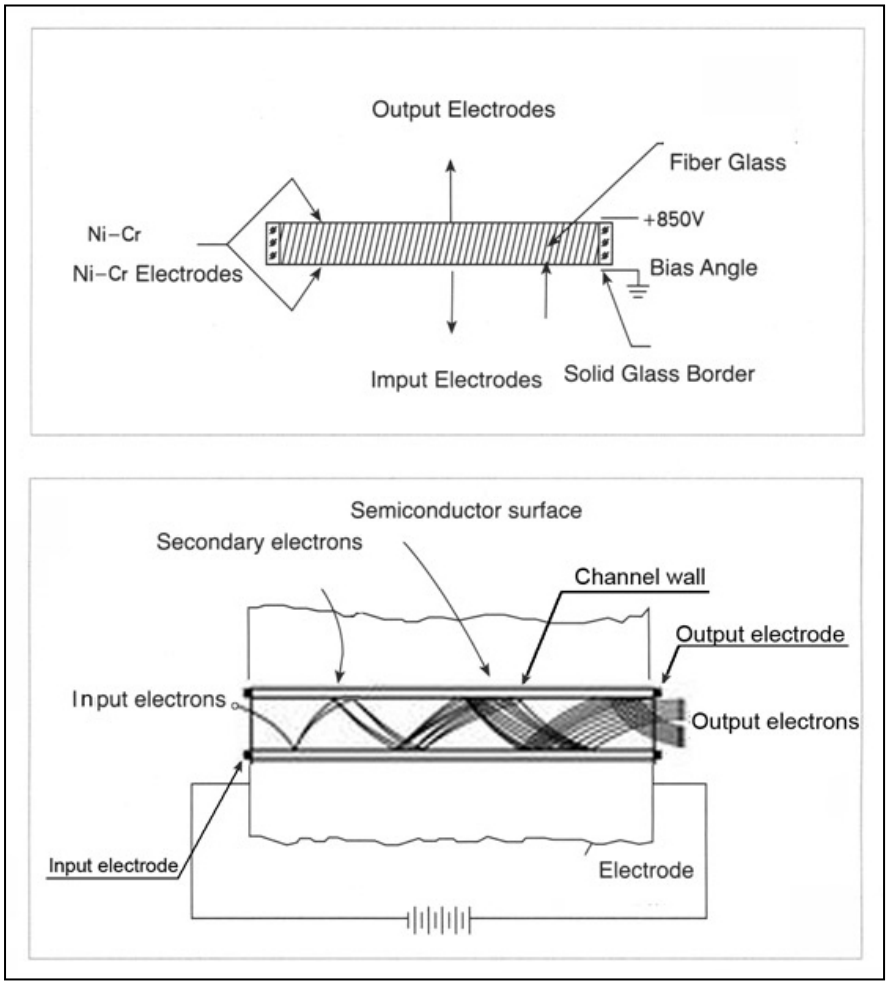

Figure 3.10: Schematic diagram of an MCP. The top diagram is looking from the side, showing the angled channels. The bottom diagram shows the electron amplification (taken from Ref. 3.20).

3.3.2 MCP Gain

The MCP has a cascade gain which is given by the following equation using the length-to-diameter ratio of the channel: gain = exp (G*(L/d), where G is the secondary emission characteristics of the channel called gain factor. This gain factor is an inherent characteristic of the channel wall material and represented by a function of the electric field intensity inside the channel. Generally, L/d is designed to be around 40, which produces a gain of 10^4 with an applied voltage of 1 kV.

If δ (the secondary electron yield of the material) were strictly constant, each photoelectron would be subject to exactly the same multiplication factor. In

practice, the emission of secondary electrons is a statistical process and therefore the specific value of δ will fluctuate from event to event about its mean value. In the simplest model, the production of secondary electrons can be assumed to follow a Poisson distribution mode about the average yield. For a single photoelectron incident, the number of secondaries produced has a mean value of δ and a standard deviation σ of $\sqrt{\delta}$. The relative variance, defined as $(\sigma/\delta)^2$, is this equal to $1/\delta$. When this process is now compounded over N identical stages of the channel, the mean number of electrons collected at the anode is given by δ^N. It can be demonstrated from the properties of Poisson statistics that the relative variance in this number is now

$$\frac{1}{\delta}+\frac{1}{\delta^2}+\frac{1}{\delta^3}+....+\frac{1}{\delta^N}\cong\frac{1}{\delta-1} \qquad \text{(eq. 3.3)}$$

Thus if $\delta >> 1$, the relative variance or spread in the output pulse is dominated by fluctuations in the yield from the first interaction with the channel wall, where the absolute number of electrons is smallest. When poor light conditions exist, signal pulses corresponding to only a few photoelectrons may be involved. Then the fluctuations in electron multiplication may interfere with the ability to discriminate against noise event, many of which correspond to single photoelectrons.

The gain factor of the Photonis SAS. MCP‡ is currently **δ = 2.5**; incidentally it is possible that an incident photoelectron interaction with the MCP channel would produce zero secondary electrons (Figure 3.11) and the signal from that photoelectron would be lost. By improving the gain factor of the MCP, the probability of a zero or a low number of secondary electrons being produced is lowered. This would greatly improve the performance of the image intensifier in low light conditions and improve the signal to noise ratio (SNR).

‡ *Appendix 1: Photonis SAS. MCP specifications.*

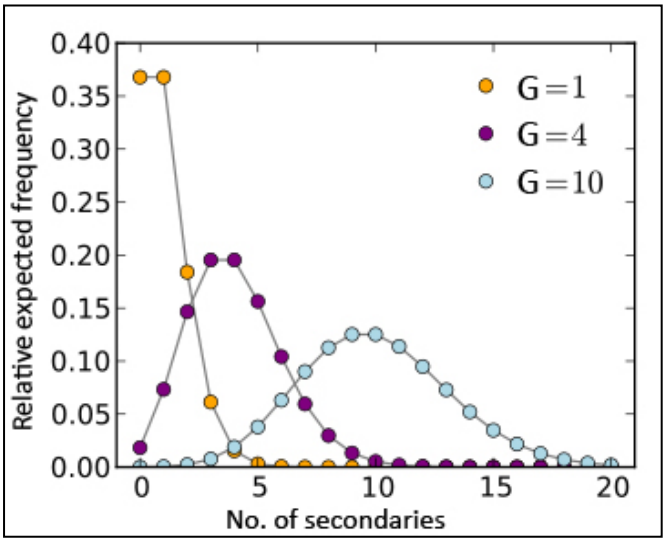

Figure 3.11: Poisson distribution for values of G (adapted from Ref. 3.21).

3.3.3 Performance characteristics

Two regimes are used to describe the imagine performance of an image intensifier. At high light levels, there are enough photons available to form a practically noise-free image; the image quality is determined by the image output contrast. From 1 mlux[§] downward, the noise performance of the image intensifier plays an increasingly important role. In the shot noise regime, the noisiness of the image intensifier is determined by three factors.

1. The quantum efficiency of the photocathode.
2. The collection efficiency of the MCP.
3. The gain noise.

Some photoelectrons do not create a detectable effect on the phosphor. They are annihilated by the MCP cladding or by the Poisson statistics of the first interaction with the MCP. As explained in the previous section, an improved gain factor of the MCP will improve the collection efficiency of the MCP and therefore improve the signal-to-noise ratio.

[§] lux: Si unit of illuminance. An example of 1 mlux is a moonless clear night sky with airglow.

Image artifacts

Image intensifiers have some typical artifacts. One of these are 'halos'; round brighter areas around bright spots. There are three main causes of halos, the most disturbing is the one created by backscattered electrons on the MCP. The diameter of this halo is equal to about four times the cathode gap. Using a carbon material will lower the backscattering effect causes by the photoelectrons impacting the walls of the channels.

Chapter 8 investigates the application of nanodiamond coatings in the MCP channels to improve the secondary electron yield. As discussed earlier in this chapter, diamond with NEA can be an excellent secondary electron emitter. A simple but effective process to improve the MCP performance characteristics would be the ability to coat the existing structure with a film of nanodiamonds.

References

3.1 G. Knoll, *Radiation Detection and Measurement* (3rd Ed.) pg. 266

3.2 A. Shih, J. Yater, C. Hor, R. Abrams, *Applied Surface Science*, 111, 3, 251 (1997).

3.3 A. J. Neves and M.H. Nazaré, *Properties, growth and applications of diamond,* By INSPEC. EMIS Group, Institution of Electrical Engineers (2001).

3.4 B. B. Pate, P.M. Stefan, C. Binns, P. J. Jupiter, M. L. Shek, I. Lindau, and W. E. Spicer, *Journal of Vacuum Science and Technology*, 19, 349 (1981).

3.5 M. W Geis, J. C. Twichell, J. Macaulay, K. Okano, *Applied Physics Letters*, 67, 9, 1328 (1995).

3.6 P. K. Baumann, R. J. Nemanich, *Surface Science*, 409, 2, 320 (1998).

3.7 R.J. Nemanich, P.K. Baumann, J. van der Weide ,in: A. Feldman, Y. Tzeng, W.A. Yarbrough, M. Yoshikawa, M. Murakawa (Eds.), *Proc. 3rd Int. Conf on Applications of Diamond Films and Related Materials*, NIST Spec. Publ. 885 (1995), p. 17

3.8 A. Shih, J. Yater, P. Pehrsson, J. Butler, C. Hor, and R. Abrams*, Journal of Applied Physics,* 82, 1860 (1997).

3.9 J. Miller, G. Brandes, *J. Appl. Phys*, 82, 4538 (1997).

3.10 A. Shih, J. Yater, P. Pehrsson, J. Butler, C. Hor, R. Abrams, *Journal of Applied Physics,* 82, 1860 (1997).

3.11 R.O. Jenkins, and W.G. Trodden*, Electron and Ion Emission*. Dover, New York, (1965) p. 65.

3.12 J.E Yater, A Shih, R Abrams, *Solid-State Electronics*, 42, 12, 2225 (1998).

3.13 A. Shih, J. Yater, C. Hor, R. Abrams, *Applied Surface Science,* 111, 251 (1997).

3.14 A. Shih and C. Hor, *IEEE Trans. Electron Dev*ices, 40, 824 (1993).

3.15 J.E. Yater, J.L. Shaw, K.L. Jensen, T. Feygelson, R.E. Myers, B.B. Pate, J.E. Butler, *Diamond and Related Materials*, 20, (5):798-802 (2011).

3.16 J.E. Yater, A. Shih, J.E. Butler, P.E. Pehrsson, *Journal of Applied Physics*, 93, 3082 (2003).

3.17 J.E. Yater, A. Shih, J.E. Butler, P.E. Pehrsson, *Journal of Applied Physics*, 97, 093717 (2005).

3.18 Photonis SAS (2010) *How does an image intensifier work?* [online] Available at:http://www.photonis.com/nightvision/technology/how_does_an_image_intensifier_work [Accessed on 31/01/2012]

3.19 Made-in-China (2012) *Microchannel Plate* [online] Available at: http://www.made-in-china.com/showroom/xtayghtydou/product-detailIohxFzjTMCVZ/China-Microchannel-Plate.html [accessed on 31/01/2012]

3.20 51EV.com (2012) *MCP* [online] Available at:http://www.51ev.org/product-Magnifiers/125532/MCP-Microchannel-plate.html [accessed on 31/01/2012]

3.21 “Poisson distribution” (2010) [online] Available at:http://en.wikipedia.org/wiki/Poisson_distribution [Accessed on 31/01/2012]

Chapter 4 Experimental Methods

4.1 Introduction

This chapter describes some of the characterisation techniques employed throughout this thesis. It begins with an account of some widely utilised techniques such as atomic force microscopy (AFM), Raman spectroscopy and scanning electron microscopy (SEM), before going on to describe some of the more specialised analytical techniques used in this thesis.

4.2 Atomic Force Microscopy (AFM)

AFM is a powerful technique that can image almost any kind of surface. It was developed to overcome a basic drawback with STM; that it can only image conducting or semiconducting materials.[4.1]

This work has relied heavily on AFM for the imaging of nanodiamonds. AFM has provided information on the topography of diamond layers, the size of individual nanodiamond particles in distributed layers and also layer thicknesses obtained by different substrate coating techniques.

The AFM consists of a cantilever with an atomically sharp tip extended down from the end of the cantilever. Tips are typically made from silicon or silicon nitride. The tip is scanned over a surface with feedback mechanisms that enable the piezo-electric scanners to maintain the tip at a constant force (to obtain height information), or height (to obtain force information) above the sample surface. Depending on the situation, forces that are measured in AFM include mechanical contact force, van der Waals forces and magnetic forces. Typical AFM heads (such as the one used in this work) employ an optical detection system in which the tip is attached to the underside of a reflective cantilever. A diode laser is focused onto the back of a reflective cantilever. As the tip scans the surface of the sample, moving up and down with the contour of the surface, the laser beam is deflected off the attached cantilever into a photodiode. The photodetector measures the difference in light intensities between the upper and lower photodetectors, and

then converts to voltage. Feedback from the photodiode difference signal, through software control from the computer, enables the tip to maintain either a constant force or constant height above the sample.

The primary modes of operation for an AFM are static mode and dynamic mode. In static mode, the cantilever is 'dragged' across the surface of the sample and the contours of the surface are measured directly using the deflection of the cantilever. In the dynamic mode, the cantilever is externally oscillated at or close to its fundamental resonance frequency or a harmonic. The oscillation amplitude, phase and resonance frequency are modified by tip-sample interaction forces. These changes in oscillation with respect to the external reference oscillation provide information about the sample's characteristics.

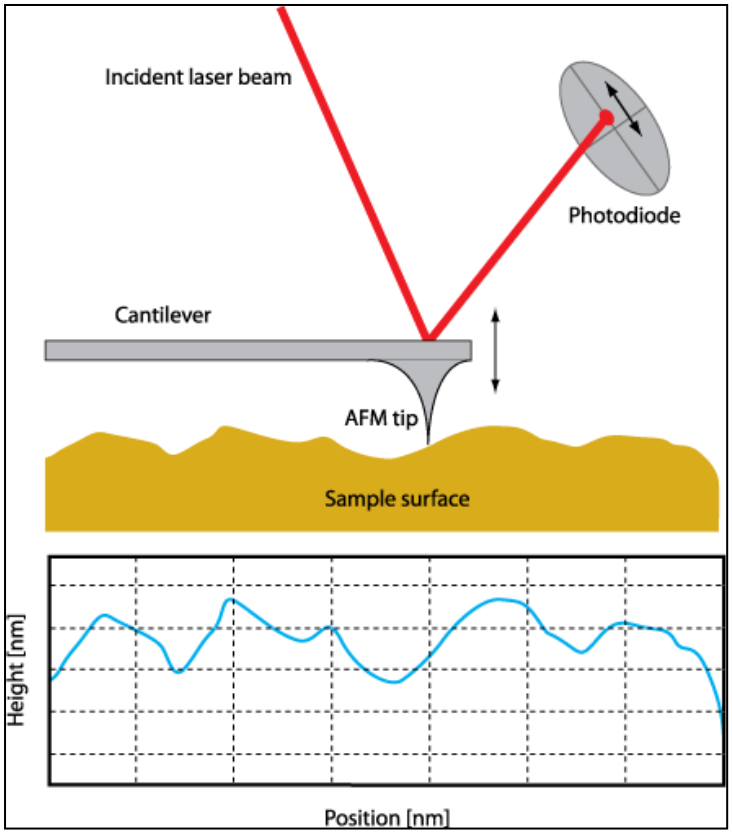

Figure 4.1: Schematic illustration of the cantilever scanning action (taken from Ref. 4.2).

4.2.1 Contact mode

In the static mode operation, the static tip deflection is used as a feedback signal. Because the measurement of a static signal is prone to noise and drift, low stiffness cantilevers are used to boost the deflection signal. However, close to the surface of the sample, attractive forces can be quite strong, causing the tip to 'snap-in' to the surface. Thus static mode AFM is almost always done in contact where the overall force is repulsive. Consequently, this technique is typically called 'contact mode'. In contact mode, the force between the tip and the surface is kept constant during scanning by maintaining a constant deflection.

4.2.2 Non-contact mode

Non-contact mode belongs to a family of AC modes, which refers to the use of an oscillating cantilever. A stiff cantilever is oscillated in the attractive regime, meaning that the tip is quite close to the sample, but not touching it (hence, "noncontact"). The tip hovers 50 - 150 Angstrom above the sample surface. Attractive Van der Waals forces (in the order of picoNewtons) acting between the tip and the sample are detected, and topographic images are constructed by scanning the tip above the surface. The detection scheme is based on measuring changes to the resonant frequency or amplitude of the oscillating cantilever in response to force gradients from the sample.

4.2.3 Dynamic force/"tapping mode" AFM

In tapping mode, a stiff cantilever is oscillated closer to the sample than in non contact mode. Part of the oscillation extends into the repulsive regime, so the tip intermittently touches or "taps" the surface. Very stiff cantilevers are used as tips can get "stuck" in the water contamination layer. Due to the interaction of forces acting on the cantilever when the tip comes close to the surface, Van der Waals force, dipole-dipole interaction, electrostatic forces, etc cause the amplitude of this oscillation to decrease as the tip gets closer to the sample. An electronic servo uses the piezoelectric actuator to control the height of the cantilever above the sample. The servo adjusts the height to maintain a set cantilever oscillation amplitude as the cantilever is scanned over the sample. A tapping AFM image is therefore

produced by imaging the force of the intermittent contacts of the tip with the sample surface.

This method of 'tapping' lessens the damage done to the surface and the tip compared to the amount done in contact mode. In addition to this the lateral resolution is improved on soft samples and lateral forces such as drag, which is common in contact mode, are virtually eliminated.

4.3 Fourier Transform Infra-Red Spectroscopy (FTIR)

Fourier transform infrared spectroscopy (FTIR) is a technique which is used to obtain an infrared spectrum of absorption, emission, photoconductivity or Raman scattering of a solid, liquid or gas. Functional groups have natural vibration frequencies characteristic of that functional group. The resonant frequencies can be in a first approach related to the strength of the bond, and the mass of the atom at either end of it. Thus, the frequency of the vibrations can be associated with a particular bond type. The fact that many functional groups can be identified by their characteristic vibration or resonant frequencies makes infrared spectroscopy often the most simplest and rapid means of assigning a compound to its class. It is extensively employed in chapter 7 to provide information on the functional groups that are present on the surface of nanodiamond particles.

4.3.1 Vibrational spectroscopy

When two or more atoms are bonded together to form a molecule many different modes of mechanical vibration are possible. The diatomic molecule can also have different modes of rotation. It happens that the frequency of molecular vibrations usually lies in the infrared region of the electromagnetic wave spectrum. Infrared absorption spectroscopy can therefore be used to study the various modes of mechanical vibrations in a molecule. It happens that in polyatomic molecules the frequencies of mechanical vibrations can be used to identify the various types of bonds and functional groups present in the molecule. This is the basis of the

popularity of infrared absorption spectroscopy in both organic and inorganic chemistry.[4.3]

For infrared spectroscopy, the selection rule is that the electric dipole moment of the molecule must change during vibration in order for a particular vibration mode to be infrared active. Symmetric vibrations are therefore forbidden because the electric dipole moment will not change. The symmetric stretch mode of carbon dioxide, for example, is not IR active.[4.3]

A complex molecule has a large number of vibrational modes which involve the whole molecule. To a good approximation, however, some of these molecular vibrations are associated with the vibrations of the individual bonds or functional groups (localised vibrations) while others must be considered as vibrations of the whole molecule. The localized vibrations are either, stretching, bending, rocking, twisting or wagging. To illustrate this, the methylene group is used (Figure 4.2)

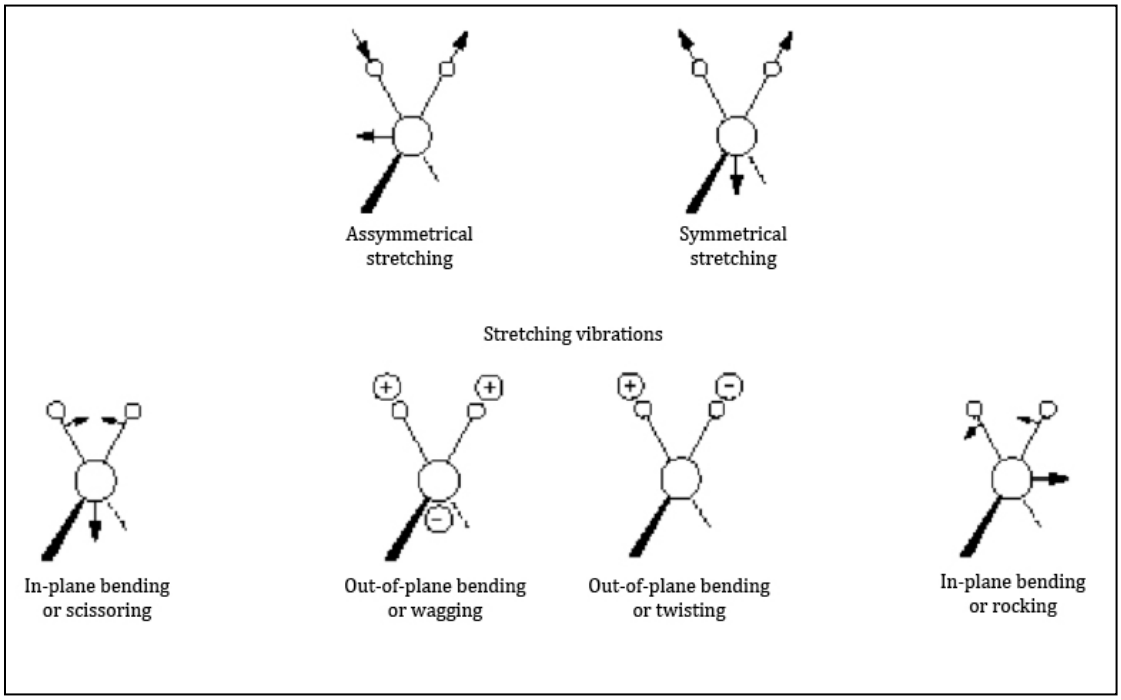

Figure 4.2: Major vibrational modes for a non-liner group methylene (CH_2) (reproduced from Ref. 4.4).

By passing a beam of infrared light through the sample, its infrared spectrum can be recorded. Examination of the transmitted light reveals how much energy was absorbed at each wavelength. This can be done with a monochromatic beam,

which changes in wavelength over time, or by using a Fourier transform instrument to measure all wavelengths at once. From this, a transmittance or absorbance spectrum can be produced, showing at which IR wavelengths the sample absorbs. Analysis of these absorption characteristics reveals details about the molecular structure of the sample. When the frequency of the IR is the same as the vibrational frequency of a bond, absorption occurs.

4.3.2 Terminology

In infrared spectroscopy the term "wavenumber", which is defined as the reciprocal of the wavelength and thus proportional to the frequency, is widely used. Wavenumber is expressed in cm^{-1}. Transmittance T is defined by $T = I/I_0$, where I is the intensity of light transmitted through the sample and I_0 is the intensity of light incident on the sample. Absorbance A is defined by $A = \log (1/T)$. The infrared spectrum obtained by FTIR spectrometer is in the form of either transmittance T or absorbance A plotted against wavenumber.

4.3.3 Fourier transfer infrared spectrometry

The principle behind Fourier Transform Infrared Spectroscopy (FTIR) is essentially based on the Michelson Interferometer (Figure 4.3).

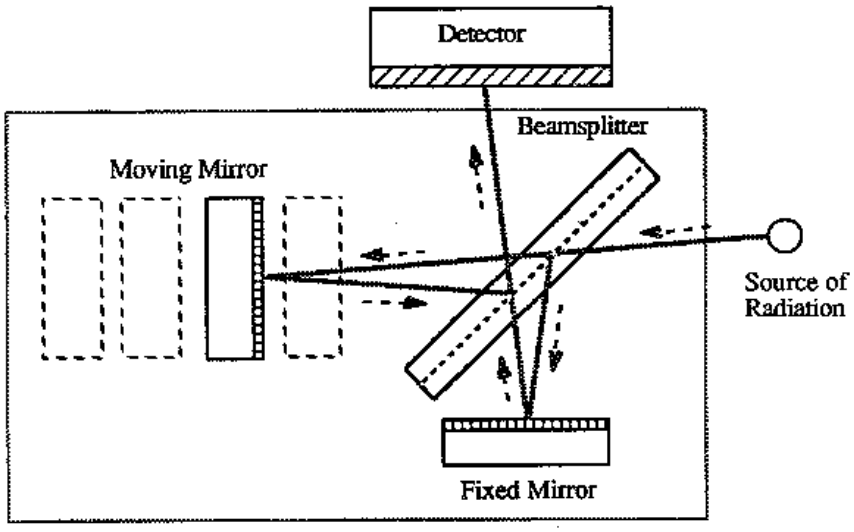

Figure 4.3: Schematic of Michelson's interferometer.

The Michelson interferometer consists of a beamsplitter, a fixed mirror and a moving mirror. Collimated radiation from the broadband infrared source is directed into the interferometer and impinges on the beamsplitter. The beamsplitter splits the incoming beam into two beams of equal intensity. Approximately half of the infrared radiation from the source is transmitted through the beamsplitter and directed onto the fixed mirror, whereas the other half reflects off the beamsplitter and is directed onto the fixed mirror. The beams reflect off the surfaces of the two mirrors and recombine at the beamsplitter, where constructive and destructive interference occurs depending on the position of the moving mirror relative to the fixed mirror. The resulting beam passes through the sample where selective absorption takes place and then continues onto the detector. The scan in FTIR spectroscopy is achieved by the mechanical displacement of the moving mirror assembly. The detected signal as a function of the position of the moving mirror is called on "interferogram", and is fed to a computer. A data-processing technique called Fourier Transform turns this raw data into the desired result, i.e. the sample's spectrum.

4.3.4 Transparent substrates

When FTIR is applied to thin films relevant to microelectronics, the infrared absorption spectrum of a thin solid film or an infrared-transparent substrate is needed. Even though silicon is a very good infrared material in terms of transparency, it is not perfect due to five factors: 1) infrared absorption due to lattice vibrations: in monocrystalline silicon, its atoms can have collective lattice vibration modes known as phonons; various absorption peaks in the infrared absorption spectrum of silicon are assigned to various combinations of phonons; 2) infrared absorption due to impurities; 3) free-carrier absorption: in semiconductors, electrons at the bottom of the conduction band can absorb infrared radiation to go up to energy levels slightly higher than the bottom of the conduction band; 4) plasma resonance, defined as the collective vibration of electrons or holes with respect to the fixed atoms in semiconductors; the substrate is transparent for frequencies above the plasma resonance frequency. In semiconductors, the plasma resonance frequency lies within the infrared region;

5) surface roughness: silicon substrates are usually highly polished only on one side, and it has been proved that the rough side can scatter infrared light significantly.

Potassium Bromide (KBr) does not influence the infrared spectrum in the wavenumber range 4000 – 400 cm^{-1}. This technique can be used when the sample material can be crushed or ground. Two milligrams of sample is mixed with 200 mg of KBr powder. The mixture is pressed into a tablet, which is then used for analysis. This technique was used to analyse detonation nanodiamond powders.[4.5] FTIR has been extensively used to investigate the presence of various functional groups on the surface of DND.[4.6,4.7,4.8,4.9]

4.4 Raman Spectroscopy

Raman spectroscopy is a surface and near-surface probe which offers insight into the binding energy of atoms within a sample by observing the light scattered by them. When monochromatic light, usually from a laser, is incident on a sample surface, a small proportion of the scattered light experiences an interaction with the lattice resulting in the creation of an optical phonon and a consequent loss of energy known as the 'Raman effect'. If the photon experiences a perfectly elastic collision with the material, it is reflected with no change in frequency. In this case, radiation is emitted in all directions win an intensity inversely proportional to the fourth power of the wavelength, therefore shorter wavelengths are more prominent in scattered light.

Radiation scattered with a frequency lower than that of the incident beam is referred to as 'Stokes' radiation. In an inelastic collision, energy is exchanged between the incident photon and the molecule. The photon may give up a proportion of its energy to excite a lattice phonon and thus emerges with lower energy. Photons such as these which contribute to the lower frequency area of a Raman distribution give rise to Stokes lines. If molecules within the lattice are initially in an excited state and lose energy to the incident photons, the emergent beams are of a higher frequency than the Rayleigh line. This lines are termed Anti-Stokes.

Raman spectroscopy does not require operation at a specific region of the light spectrum. The region is governed by the choice of incident light frequency, and therefore Raman analysis may be performed in the visible region.

In a typical experimental set-up, laser light is delivered to the sample through an optical microscope to facilitate the operator to selection the region of the sample to be analysed. The scatted light is then filtered and delivered to an optical multichannel analyser which can take the form of a spectrometer or monochromator combined with a photodiode array or charge coupled device. Scanning, collection and interpretation of the data under computer control allows rapid generation of spectra having a resolution of less than one wavenumber with the mode of operation (Stokes or anti-Stokes) being determined by the filtering regime of the optical system.

Raman scattering spectroscopy is a particularly useful technique to differentiate between different phases of carbon, as diamond and related carbon material have strong and recognisable Raman "signature' spectra. Since it is non destructive, requires virtually no sample preparation or vacuum requirements, it is incredibly useful for the identification of diamond. The first order Raman spectrum of natural diamond (purely sp^3 bonded carbon) has been demonstrated to show an explicit single peak at 1332cm^{-1} at room temperature, which is clearly distinguishable from the broader non-diamond carbon features such as those shown at 1500-1600cm^{-1}.

4.5 Scanning electron microscopy

A scanning electron microscope uses a focussed beam of high energy electrons instead of light to form an image. The signals that derive from electron-sample interactions reveal information about the sample including external morphology (texture), chemical composition, and crystalline structure and orientation of materials making up the sample.

In a typical SEM, an electron beam is thermionically emitted from an electron gun under vacuum conditions. The gun filament is usually a loop of tungsten which

functions as the cathode. Since tungsten has a high melting point and low vapour pressure, it can be heated for electron emission. Field emission guns (FEG) can also be used to produce an electron beam that is smaller in diameter, more coherent and with up to three orders of magnitude greater current density or brightness than can be achieved with conventional thermionic emitters.

The electron beam, which typically has an energy ranging from 0.2 keV to 40 keV is focused by one or two condenser lenses to a spot about 0.4 nm to 5 nm in diameter. The beam passes through pairs of scanning coils or pairs of deflector plates in the electron column, typically in the final lens, which deflect the beam in the *x* and *y* axes so that it scans in a raster fashion over a rectangular area of the sample surface. The energy exchange between the electron beam and the sample results in the reflection of high-energy electrons by elastic scattering, emission of secondary electrons by inelastic scattering and the emission of electromagnetic radiation, each of which can be detected by specialised detectors. These signals include secondary electrons (that produce SEM images), backscattered electrons (BSE), diffracted backscattered electrons (EBSD that are used to determine crystal structures and orientations of minerals), photons (characteristic X-rays that are used for elemental analysis and continuum X-rays), visible light (cathodoluminescence-CL), and heat. Secondary electrons and backscattered electrons are commonly used for imaging samples: secondary electrons are most valuable for showing morphology and topography. In the most common or standard detection mode, secondary electron imaging or SEI, the SEM can produce very high-resolution images of a sample surface, revealing details about less than 1 to 5 nm in size. Due to the very narrow electron beam, SEM micrographs have a large depth of field yielding a characteristic three-dimensional appearance useful for understanding the surface structure of a sample.

The secondary electrons are moving very slowly when they leave the sample and are attracted to the detector which has a positive charge. This attractive force allows electrons from a wide area to be pulled in. The secondary electron current reaching the detector is recorded and the microscope image consists of a “plot” of this current against probe position on the surface. The contrast in the micrograph

arises from several mechanisms, but first and foremost from variations in the surface topography. Electronic amplifiers of various types are used to amplify the signals which are displayed as variations in brightness on a cathode ray tube. The raster scanning of the CRT display is synchronised with that of the beam on the specimen in the microscope, and the resulting image is therefore a distribution map of the intensity of the signal being emitted from the scanned area of the specimen. The image may be captured by photography from a high-resolution cathode ray tube, but in modern machines is digitally captured on a computer. Figure 4.4 shows a schematic of the various components within a typical SEM.

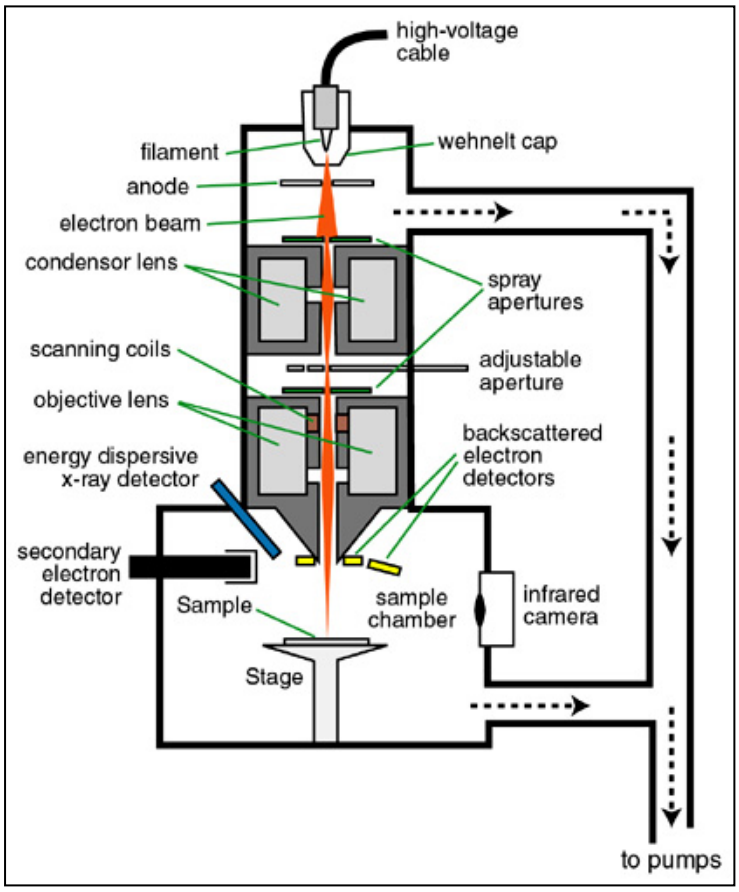

Figure 4.4: Schematic of a typical SEM(taken from Ref. 4.10)

Sample preparation

Samples must be of an appropriate size to fit in the specimen chamber. For conventional imaging, the sample must be electrically conductive, at least at the surface. Nonconductive specimens tend to charge when scanned by the electron

beam, and especially in secondary electron imaging mode, this causes scanning faults and other image artifacts. They are therefore usually coated with an ultrathin coating of electrically conducting material (gold or graphite for example), deposited on the sample either by low-vacuum sputter coating or by high-vacuum evaporation.

4.6 Impedance Spectroscopy

Impedance Spectroscopy (IS) is a very useful technique which can be used to characterise the electrical properties of materials and their interfaces with electrically conducting electrodes. The technique may be used to investigate the dynamics of bound or mobile charges in bulk or interface regions of any kind of ionic solids, or liquid materials, semiconductors, mixed ionic-electronic materials and insulators (dielectrics). The technique measures the impedance as a function of frequency automatically in the range of 1 MHz to 10 MHz and is easily interfaced to computer. The technique was comprehensively reviewed by MacDonald.[4.11]
Complex impedance measurements are capable of separating the various contributions to the total conductivity due to bulk, grain boundary and electrode and therefore are suited to measuring nanodiamond layers.

Impedance spectroscopy is performed by applying an AC potential of $V(t) = A \sin(\omega t)$, for a single frequency $\omega/2\pi$, and measuring the current $I = A \sin(\omega t+\phi)$ through the sample.[**] The relationship between the applied potential and the current flow is known as the impedance, which is analogous to the resistance-current-potential of a dc circuit. ϕ is the phase difference between the voltage and current; it is zero for purely resistive behaviour. Therefore, impedance measurements are carried out over a frequency range. In the experiments performed in this work, from 0.1 – 10^7 Hz.
The objective of impedance experiments is to determine the values of the various elements in the equivalent circuit, or to confirm that a system fits a particular

[**] A = maximum amplitude, ω = frequency in radians/sec, f = frequency in hertz and ϕ = phase shift in radians.

equivalent circuit model. We will consider the impedance plots for the following equivalent circuit, consisting of a single resistance-capacitance (RC) parallel circuit. This model has been selected because many of the electrochemical systems encountered in practice are modelled using this network.[4.11]

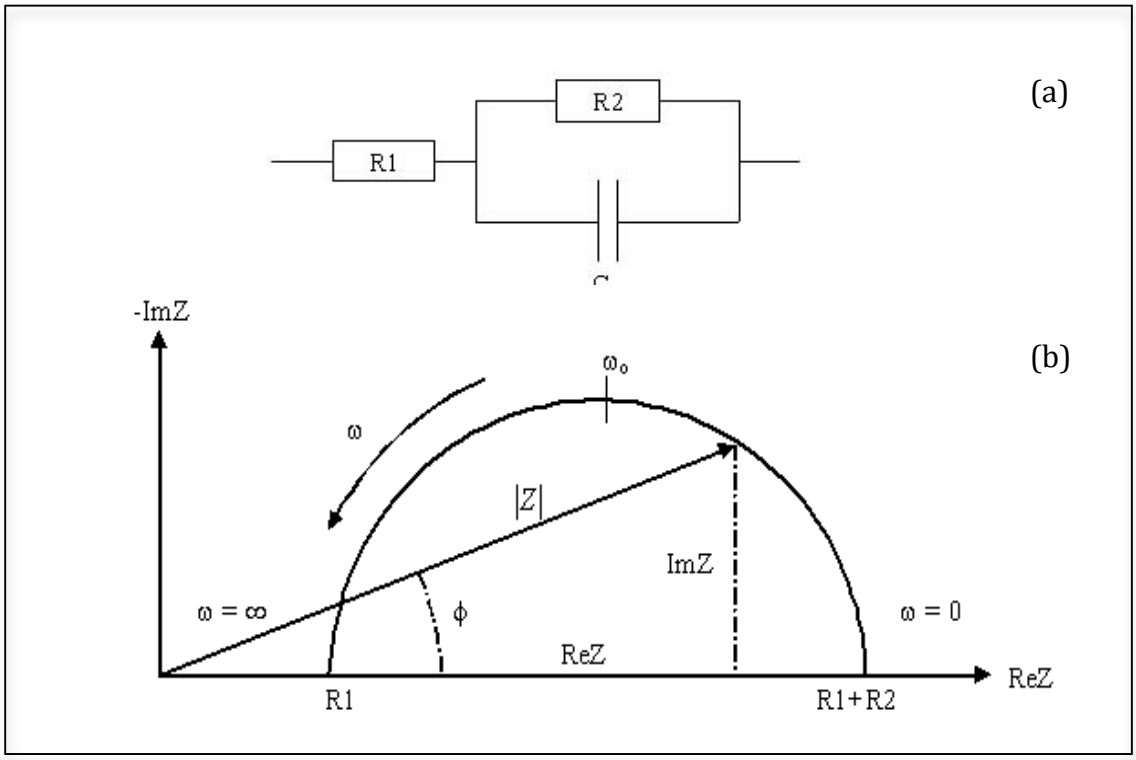

Figure 4.5: Equivalent circuit and AC impedance plots of an electrochemical cell with one time constant: (a) equivalent circuit, (b) Cole-Cole plot in the complex plane, $\omega_o=1/(R_2C)$

The plot in figure 4.5 (b) is based on a vector diagram, corresponding to a sine wave *I*. The current sine wave can be described by the following equations:

$$I = A \sin(\omega t+\phi) \qquad \text{(eq. 4.5.1)}$$

$$\omega = 2\pi f \qquad \text{(eq. 4.5.2)}$$

where A is the maximum amplitude, ω is the frequency in radians/sec, f is the frequency in Hz, ϕ is the phase shift in radians.

The impedance $Z(\omega)$ is a complex number that can be represented either in polar co-ordinates or in Cartesian coordinates:

$$Z(w) = |Z|e^{j\phi} \qquad \text{(eq. 4.5.3)}$$

$$Z(w) = \mathrm{Re}\,Z + j\,\mathrm{Im}\,Z \qquad \text{(eq 4.5.4)}$$

where ***ReZ*** and ***ImZ*** are the real part and the imaginary part of the impedance, respectively.[4.10] The relationships between theses quantities are:

$$|Z|^2 = (\mathrm{Re}\,Z)^2 + (\mathrm{Im}\,Z)^2 \qquad \text{(eq. 4.5.5)}$$

$$\phi = Arc\tan\frac{\mathrm{Im}\,Z}{\mathrm{Re}\,Z} \qquad \text{(eq. 4.5.6)}$$

$$\mathrm{Re}\,Z = |Z|\cos\phi \qquad \text{(eq. 4.5.7)}$$

$$\mathrm{Im}\,Z = |Z|\sin\phi \qquad \text{(eq. 4.5.8)}$$

Figure 4.3 (a) shows the equivalent circuit of a material with a resistive and capacitive element, whose impedance is:

$$Z(\omega) = \frac{V}{I} = R_1 + \frac{1}{\frac{1}{R_2} + jC\omega} = R_1 + \frac{R_2}{1+\omega^2 C^2 {R_2}^2} - \frac{j\omega C {R_2}^2}{1+\omega^2 C^2 {R_2}^2} \qquad \text{(eq. 4.5.9)}$$

where V is the voltage, I is the current, R_1 and R_2 are the resistance values of the equivalent circuit and C is the capacitance value of the equivalent circuit.

The impedance modulus is given by:

$$|Z(\omega)| = \sqrt{\left(R_1 + \frac{R_2}{1+\omega^2 C^2 {R_2}^2}\right)^2 + \left(\frac{\omega C {R_2}^2}{1+\omega^2 C^2 {R_2}^2}\right)^2} \qquad \text{(eq. 4.5.10)}$$

The high frequency intercept yields R_1, whereas the low frequency $R_1 + R_2$, meaning that at high frequencies the capacitor conducts the current easily, whereas at low frequencies the current flow via the capacitor is impeded.[4.11] The current therefore flows through R_1 and R_2, and the impedance is given by the sum of the two resistors:

$$|Z(\omega)| = R_1 + R_2 \text{ when } \omega \rightarrow 0 ,$$
$$|Z(\omega)| = R_1 \text{ when } \omega \rightarrow \infty$$

At intermediate frequencies the impedance has a value between R_1 and $R_1 + R_2$, thus possessing both real and imaginary components. This gives rise to the semicircular shaped Cole-Cole plot, described by the equation:

$$\left[Z' - \left(R_1 + \frac{R_2}{2}\right)\right]^2 = Z''^2 = \left(\frac{R_2}{2}\right)^2 \qquad \text{(eq. 4.5.11)}$$

It has been shown that equation (4.5.11) is analogous to the equation of a circle, with radius $r = \frac{R_2}{2}$ and a centre at $\left(R_1 + \frac{R_2}{2}, 0\right)$.

In all the materials studied, ω, R_1 and R_2 are greater than zero, thus resulting in semicircles on the axis when plotted as a function of frequency.
$Z(\omega)$ is plotted in figure 4.5 in terms of a Cole-Cole plot in the complex plane with the negative imaginary parts in the positive part of the real axis.

At the peak of the semicircle, the following condition is obtained:

$$\omega_{max} R_2 C = 1 \qquad \text{(eq 4.5.12)}$$

and hence:

$$C = \frac{1}{2\pi f_{max} R_2} \qquad \text{(eq 4.5.13)}$$

Knowing the value of R_2 and the frequency f_{max}, the value of the capacitance can be determined. It is possible to obtain all three parameters (R_1, R_2 and C) from the Cole-Cole plot as shown in figure 4.5 (b), provided a sufficient frequency range is investigated. The semicircle in figure 4.5 (b) is characteristic of a single "time constant". Electrochemical impedance plots often contain several time constants. Often only a portion of one or more semicircles is seen.

The impedance plots of polycrystalline materials can be related to their microstructure by means of physical models of the grain interior, grain boundary and the electrode behaviour. The physical models used to describe the electronic materials are reviewed in detail with their respective circuit equivalents.[4.12] The widely used physical model is a more realistic one, which treats the microstructure as an array of cubic shaped grains with flat grain boundaries of finite thickness as shown in figure 3.6.[4.13]

The current flow is assumed to be one-dimensional and the current path at the corners of the grains is neglected. In this case the two paths available to the current are either through the grains and across the grain boundary, or along grain boundaries, as depicted in figure 3.6. Depending on the relative magnitudes of grain and grain boundary conductivity one of the two paths may dominate. This model has been applied to many material systems and according to this model the bulk resistivity and the grain boundary resistivity may have different response.[4.13]

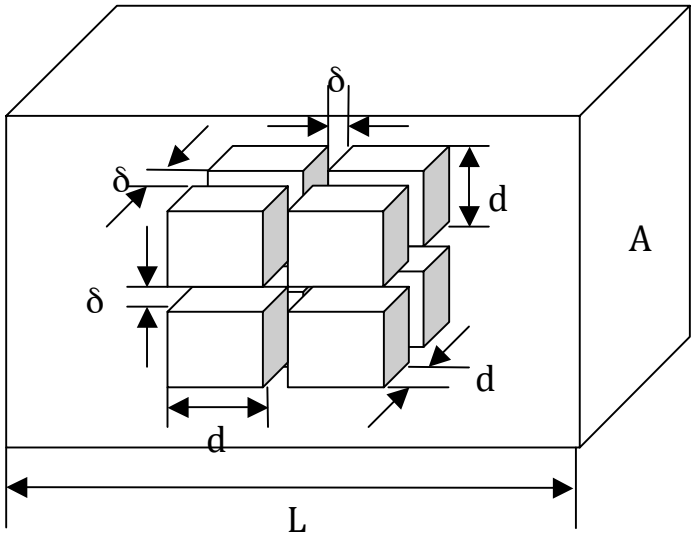

Figure 4.6: Brick layer model of idealized polycrystalline structure in which grains of dimensions d[3] are separated by grain boundaries of width δ (from Ref. 4.14).

The grain interior capacitance (C_{gi}) is given by equation (eq 4.5.14). Where L is the sample length in millimetres, A is the cross sectional area (order of 10 mm^2), ε_o is the permittivity of free space (8.854 x 10^{-12} F/m) and ε_{gi} is the electrical relative dielectric constant of the grain interior. The grain interior capacitance for diamond is estimated around 0.5 pF.

$$C_{gi} = \frac{A\varepsilon_o\varepsilon_{gi}}{L} \qquad \text{(eq 4.5.14)}$$

$$C_{gb} = \frac{A\varepsilon_o\varepsilon_{gi}}{L}\frac{d}{\delta} \qquad \text{(eq 4.5.15)}$$

The same A and L values can be applied to the grain boundary capacitance (C_{gb}) in equation (eq 4.5.15). The grain size of a typical polycrystalline material is usually on the order of micrometres (μm), where the effective grain boundary width is expected to be on the order of nanometres (nm). Thus the estimated grain boundary capacitance for a polycrystalline diamond is around 0.5 nF.

The *loss angle* is a standard and widely used measure of capacitor and insulator performance. Its value is simply 90°-ϕ, where ϕ is the phase angle of the associated impedance. The quantity normally quoted however is tan**δ**, which is known as the *loss tangent*. tan**δ** is zero for a perfect insulator or capacitor and increases as the losses increase.

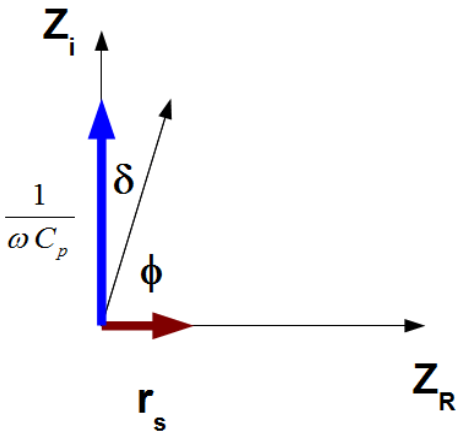

Figure 4.7: Showing the angle, δ on an impedance plot.

$$\tan\delta = \frac{|Z_R|}{|Z_i|} = \frac{|\varepsilon''|}{|\varepsilon'|} \qquad \text{(eq 4.5.16)}$$

Where ε'' is imaginary part of the complex dielectric constant and ε' is its real component. This is a profound result, because the equation does not contain any length, area, capacitance, or reactance terms. Therefore, the tan**δ** value for a particular insulator is completely independent of the physical shape or value of the capacitor that was used to determine it; tan**δ** is the loss tangent for that capacitance. In terms of losses therefore, there is only one basic selection criterion for insulating materials; for tan**δ** to be as small as possible.

4.7 Substrate cleaning

Prior to the deposition of any nanodiamond particles the substrate must be cleaned to remove any grease or dust particles that will cause the nanodiamonds to begin agglomerating.

De-grease

1) The sample is submerged in a dish containing acetone and gently agitated for 10 minutes. The sample is then removed for step 2.
2) The sample is submerged in a dish containing isopropyl alcohol and gently agitated for 10 minutes. The sample is then removed for step 3.
3) The sample is submerged in a beaker containing de-ionised water. The beaker is put into an ultrasonic bath and agitated for 10 minutes.
4) The sample is removed from the beaker and dried with pressurised nitrogen.

This protocol is followed immediately before the deposition procedure for coating the surface of the substrate with nanodiamonds.

References

4.1 G. Binnig, C. F. Quate, C. Gerber, *Physical Review Letters,* 56, 930 (1986).

4.2 Bioimaging (2008) *Atomic force microscopy - a brief explanation* [online] Available at: http://www.bioimaging.dk/index.php?id=77 [Accessed on 31/12/2011]

4.3 W.S Lau, *Infrared Characterization for Microelectronics*, World Scientific Publishing Co. Pte. Ltd. (1999)

4.4 R. M. Silverstein, G. C. Bassler, and T. C. Morrill, *Spectrometric Identification of Organic Compounds, 4th edition*. New York: John Wiley & Sons, 1981, p. 166, by permission of John Wiley & Sons, Inc., (1981)

4.5 M. Bevilacqua, A. Chaudhary, R.B. Jackman, *Journal of Applied Physics*, 106 (12) (2009).

4.6 T. Jiang, *Journal of Chemical Society*, Faraday Transactions, 92, 3401 (1996).

4.7 E. Mironov, A. Koretz, E. Petrov*, Diamond and Related Materials*, 11, 872 (2002)

4.8 D. Mitev, R. Dimitrova, M. Spassova, Ch. Minchev and S. Starev, *Diamond and Related Materials*, 16, 776 (2007).

4.9 A.P. Koshcheev, *Russian Journal of Physical Chemistry A***,** 82, 10 (2009).

4.10 James H. Wittke (2008) *Introduction* [online] Available at: http://www4.nau.edu/microanalysis/Microprobe-SEM/Instrumentation.html [Accessed on at 31/12/2011]

4.11 J.R. MacDonald, *Impedance Spectroscopy*, Wiley, New York (1987)

4.12 N. Khan, PhD Thesis, University of London (1990)

4.13 H.L Tuller, *Solid State Ionics*, 131, 143 (2000)

4.14 T. Van Dijk and A.J. Burggraaf, *Physica Status Solidi A*, 63, 229 (1981).

Chapter 5 AFM and Raman studies of nanodiamond layers

An interesting property of monodispersed detonation nanodiamond is that the particles in colloidal form can readily attach themselves to substrate materials such as silicon or diamond. This is highly dependent on the zeta potential†† of the particles and therefore the surface functional groups.[5.1]

The formation of nanodiamond layers on substrates has been the basis for various investigations, from allowing the measurement of the electrical properties of mDND[5.2] to their utilisation to promote the formation of functional neuronal networks.[5.3] Although there have been a number of publications dealing with the issue of colloidal dispersion, there is little information on the details of producing ND covered surfaces, especially in regards to coverage densities. This is a critical step for the production of high nucleation densities of diamond nanoparticles for the nucleation of nanocrystalline diamond films and reducing the nucleation density for discrete single photon emitters.

The subsequent chapters of this thesis rely on the ability to coat substrate materials with the required thickness or density of nanodiamond particles. Therefore this chapter investigates the processes and colloid concentrations required to achieve a variety of ND coverage densities.

5.1 Deposition of nanodiamonds onto surfaces

The monodispersed DND colloid used was purchased from NanoAmando (New Metals & Chemicals Corporation, Japan). This material has been de-aggregated by a process of wet-milling with zircona beads,[5.4] which, along with any additional pretreatment, has been discussed in detail in chapter 2.

The as-received nanodiamond surface is covered in a variety of surface groups including carboxylic acid groups, anhydride functionalities and groups such as C–OH, COO^-, C–O–C, C–H. The FTIR of the as-received nanodiamond surface is presented in chapter 7, figure 7.3. The zeta (ζ) potential of the nanodiamonds in this state is +0.45 mV and the attachment of the NDs on a surface such as silicon is

†† *Zeta potential*: the potential difference between the dispersion medium and the stationary layer of fluid attached to the dispersed particle.

made possible through electrostatic attraction.[5.1] A very shallow layer (approximately 1 nm) of so-called native oxide is formed on the silicon surface when it is exposed to air under ambient conditions. Oxygen, having superior electro-negativity renders the surface negative.

The colloid is received with a concentration of 50 g/L of NDs dispersed in water. This concentration of particles is significantly more than required and it is typical to dilute the solution to lower concentrations for coating substrates. Contamination of the colloid with dust or salts causes the particles in the colloid to agglomerate, therefore any handling of the colloid and sample preparation was carried out in the clean room.

To prepare a dilution, the required volume of the original solution is pipetted out using a micropipette with sterile, individually packed tips. This volume is then added to a bottle or beaker containing the required volume of de-ionised water. The beaker is then placed in an ultrasound bath for a short duration to ensure the particles are well dispersed throughout the volume.

The substrate material, in this case silicon, is cleaned prior to utilisation using the de-grease method described in chapter 4.7. The substrate is then placed in to the beaker and the sample is ultra-sonicated in the colloid for the chosen duration of time.

Following ultra-sonication the substrate is removed from the beaker with tweezers and one of two methods can be applied;

(1) Immediately dip the sample in de-ionised water to remove the excess colloid and dry with pressurised nitrogen. This leaves only the nanodiamonds attached during the sonication process on the surface of the sample.

(2) Leave the excess colloid on the substrate and place the substrate on a heater to evaporate the water. This second method is used in conjunction with higher colloid concentrations to obtain thick ND layers.

5.2 Results

After nanodiamonds were coated on to the substrates, AFM was performed using a Veeco Dimension V.

Preparation conditions	Sample 1
Colloid Concentration:	3.33 g/L (0.2 ml ND colloid in 2.8ml DI water)
Post Sonication:	Nitrogen dried.

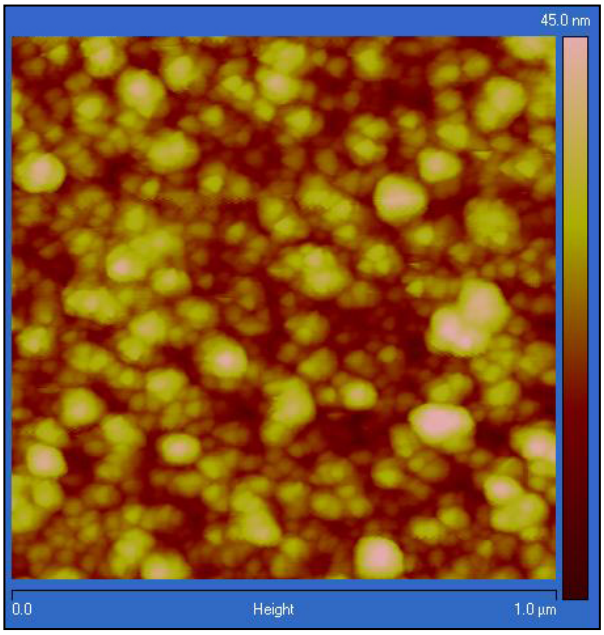

Figure 5.1: AFM image of ND layer on silicon using a colloid of concentration 3.33g/L. The image size is 1.0 µm x 1.0 µm. The height scale is given by the gradient scale on the right hand side of the image.

Figure 5.1 shows that a colloid concentration of 3.33 g/L gives complete surface coverage. It appears that there may be some agglomeration of the particles as shown by the large, bright spots on the image. However, from this image, it is not possible to establish the approximate thickness of the layer. Therefore, following this, the AFM tip was forced into contact with the sample surface and a rectangular area of particles was scratched away using the tip. Figure 5.2 shows the cantilever from above (left image) under the optical microscope of the AFM, and on the right, the outline of the scratched area is just visible.

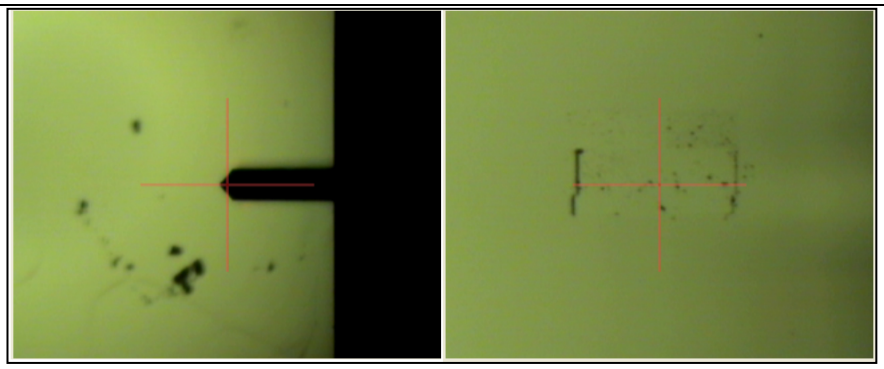

Figure 5.2: Optical image of the AFM probe from above (left) and the scratched area of sample 1 (right).

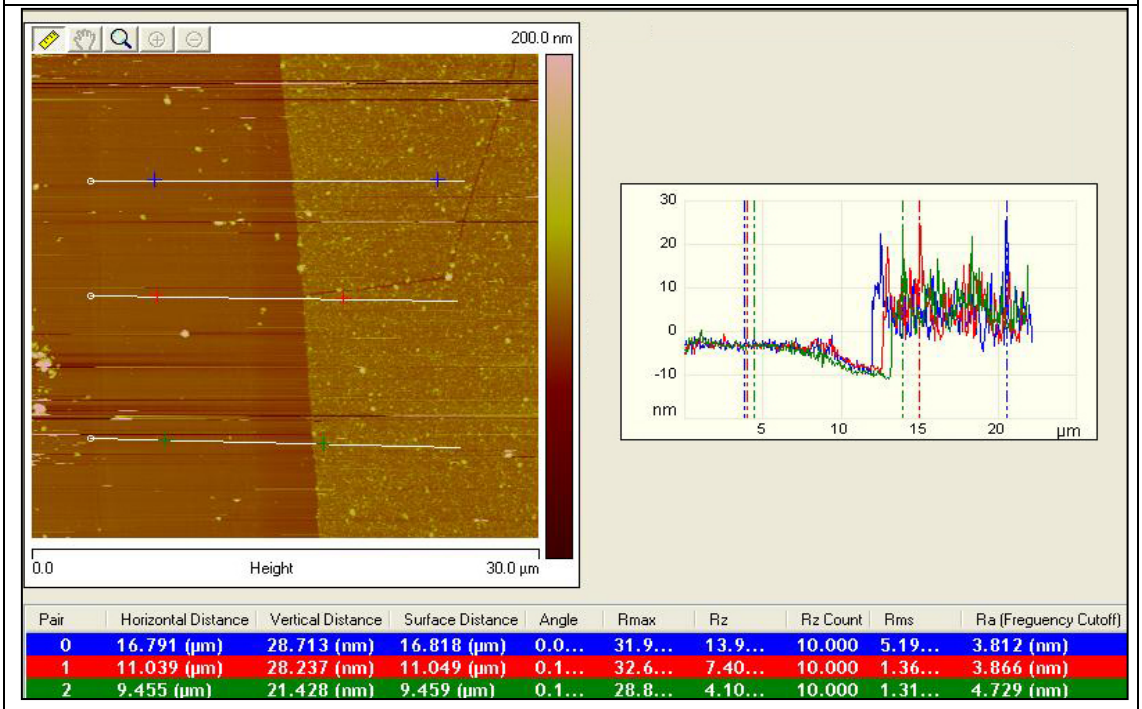

Pair	Horizontal Distance	Vertical Distance	Surface Distance	Angle	Rmax	Rz	Rz Count	Rms	Ra (Frequency Cutoff)
0	16.791 (µm)	28.713 (nm)	16.818 (µm)	0.0…	31.9…	13.9…	10.000	5.19…	3.812 (nm)
1	11.039 (µm)	28.237 (nm)	11.049 (µm)	0.1…	32.6…	7.40…	10.000	1.36…	3.866 (nm)
2	9.455 (µm)	21.428 (nm)	9.459 (µm)	0.1…	28.8…	4.10…	10.000	1.31…	4.729 (nm)

Figure 5.3: AFM image of the interface between the scratched and non-scratched region (left) showing line scans. The line scans information is plotted on the right.

Figure 5.3 shows the AFM image obtained when imaging the scratched and non scratched area. The silicon surface is clearly visible on the left hand side of the image, albeit with a few scattered remaining particles. Information from three line scans was obtained, shown in the blue, red and green rows. Although there are some peaks in the data, overall the heights fluctuate around the 10 nm point. Given the ND particle size is ~5 nm, this corresponds to a layer of roughly two particles height in thickness.

The next sample was deposited with the same colloid concentration; however, upon removal from the solution the excess colloid on the surface was not removed. The sample was placed on a heater to dry, thereby evaporating the water and leaving behind the NDs. The AFM image is shown in figure 5.4. It is difficult to distinguish individual particles as there appears to be a high degree of agglomeration.

Preparation conditions	**Sample 2**
Colloid Concentration:	3.33 g/L (0.2 ml ND colloid in 2.8ml DI water)
Post Sonication:	Excess colloid left to dry on sample.

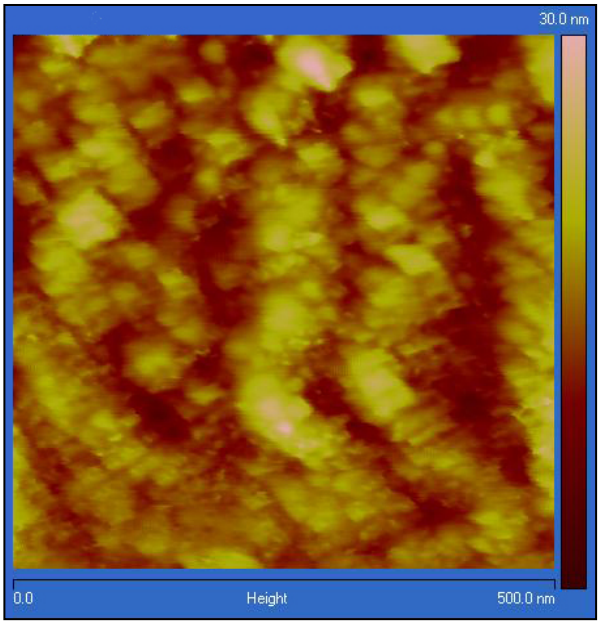

Figure 5.4: AFM image of ND layer on silicon using a colloid of concentration 3.33g/L. The image size is 500 nm x 500 nm. The height scale is given by the gradient scale on the right hand side of the image.

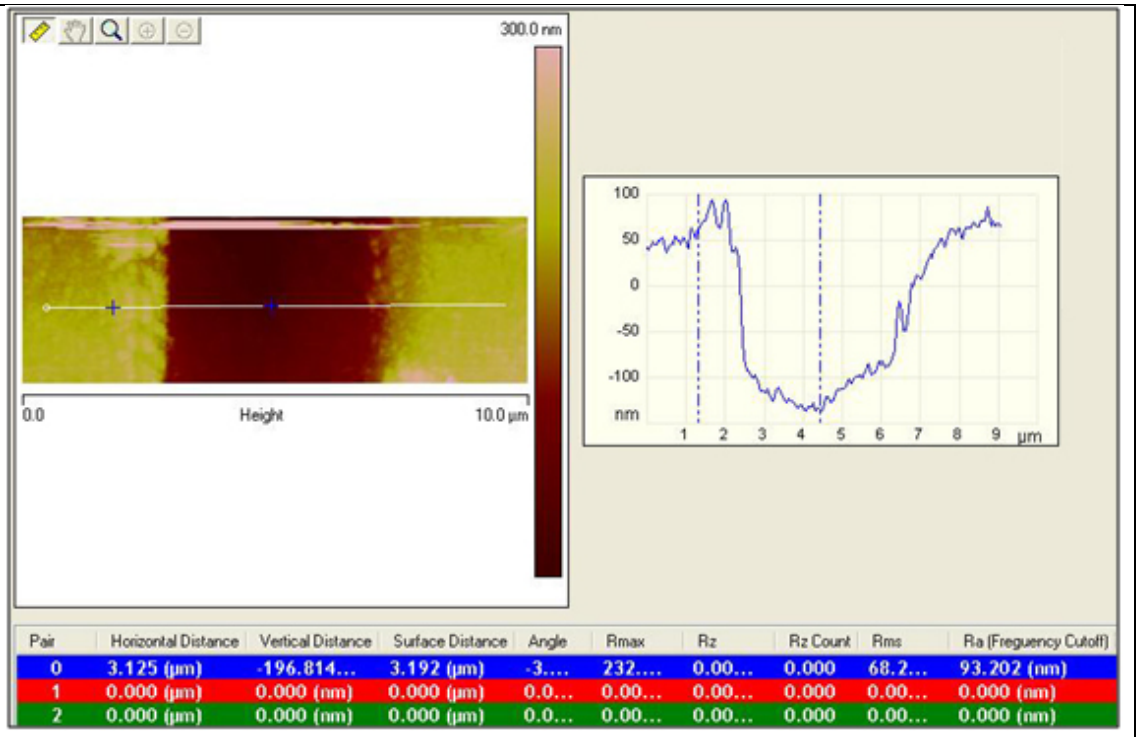

Figure 5.5: Sample 2 - AFM image of the interface between the scratched and non-scratched region (left) showing line scans. The line scans information is plotted on the right.

Figure 5.5 shows the AFM of the scratched area of sample 2. The dark trench that can be seen in the middle of the image corresponds to where the NDs have been scratched away. The single line scan obtained shows that there is a depth of about 175 – 200 nm between the silicon substrate and the top of the ND layer, making this a very thick and dense layer of particles.

Figure 5.6 shows the AFM image obtained from sample 3. This sample was deposited using a colloid concentration of 0.05 g/L. Upon removal, the sample was rinsed in DI water to remove the excess colloid from the surface and then dried using pressurised nitrogen. Individual particles are visible and they have a much more even distribution. The line scans which are not shown here revealed a layer height corresponding to single particles; a so-called 'monolayer'.

Preparation conditions	Sample 3
Colloid Concentration:	0.05 g/L (0.2 ml ND colloid in 2.8ml DI water)
Sonication:	10 minutes
Post Sonication:	Dipped in DI water and dried with pressurised nitrogen.

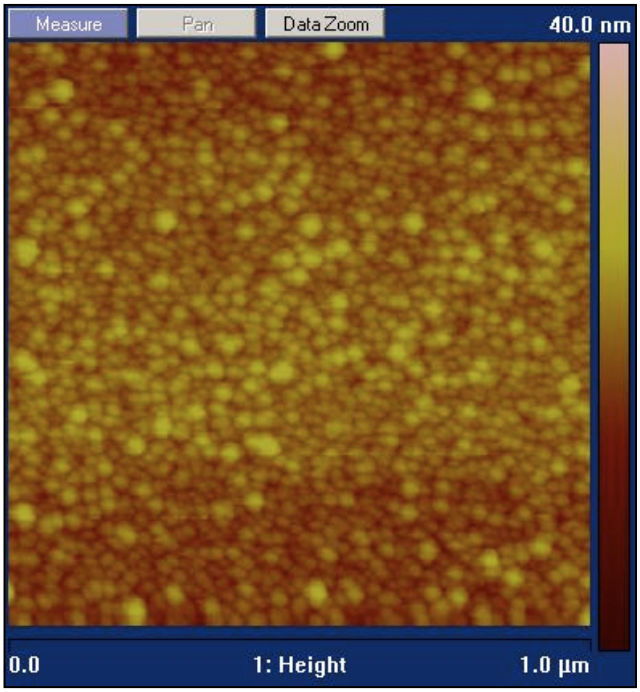

Figure 5.6: AFM image of ND layer on silicon using a colloid of concentration 0.05 g/L. The image size is 1.0 µm x 1.0 µm. The height scale is given by the gradient scale on the right hand side of the image.

Figure 5.7 shows the AFM image obtained when a very low colloid concentration of 0.001 g/L was used. Additionally, no sonication was applied and instead the sample was dipped into the colloid for 60 seconds. The reasoning behind this was that the agitation is likely to cause more interaction between the particles and the surface of the sample, leading to more particle attachment. The surface coverage is low, however all the visible particles seem to be agglomerations on the surface, of a few tens of nanometres in diameter.

Preparation conditions	**Sample 4**
Colloid Concentration:	0.001 g/L (0.2 ml ND colloid in 2.8ml DI water)
Sonication:	None. Dipped in colloid for 60 seconds.
Post Sonication:	Dipped in DI water and dried with pressurised nitrogen.

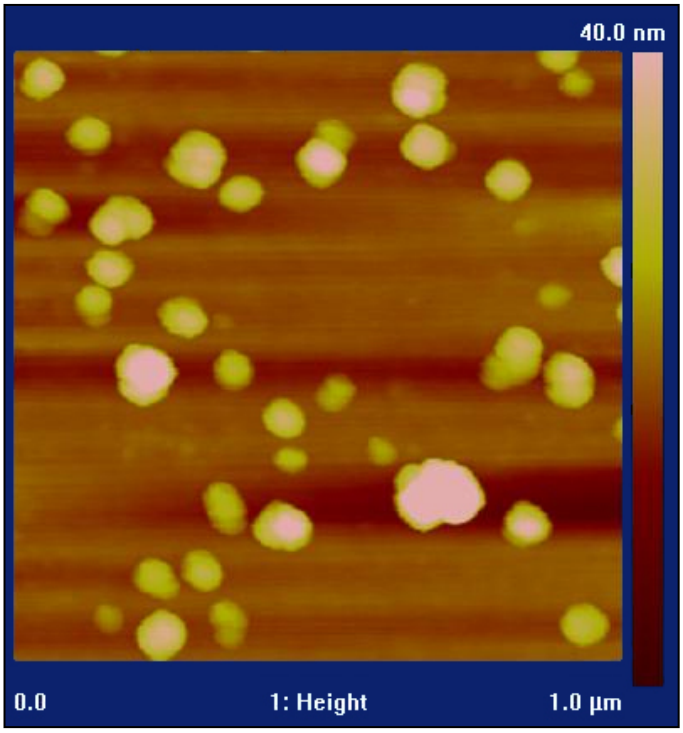

Figure 5.7: AFM image of ND layer on silicon using a colloid of concentration 0.001 g/L. The image size is 1.0 µm x 1.0 µm. The height scale is given by the gradient scale on the right hand side of the image.

Protocols for the deposition of different types of nanodiamond layers have been presented. Most critically, for the seeding of diamond growth, the concentration and procedure for creating a densely packed 'monolayer' of nanodiamonds (sample 3) has been established. As well as the typical concentration by which there are insufficient NDs in the colloid to cover the surface of a substrate. The results displayed in this section are representative images of numerous repeat experiments. AFM has been identified as a powerful tool in the investigation of particle size and particle height.

5.3 Raman spectroscopy of nanodiamond layers

Raman spectroscopy provides valuable insights into the phase composition of carbon materials. Although Raman spectra of nanodiamonds are presented in the literature, there is no general "Raman spectrum of ND" as it varies for different ND grades. It is therefore important to investigate the specific NDs used throughout this work.

Visible Raman spectroscopy was carried out with a Renishaw Invia Raman Spectrometer was used with a laser wavelength of 514.5 nm. It was not possible to obtain a signal from an approximate monolayer of NDs due to the strong Raman signal from the silicon substrate. To overcome this problem, a thick layer of NDs was deposited on a silicon substrate. The procedure used to create the sample was the same as that described in chapter 5.2, sample 2.

Figure 5.8 shows an image of the sample through the optical microscope of the spectrometer. This area was chosen for the study for the apparent thickness of the deposited ND layer. Attempts were made to obtain Raman spectra at different points on the sample but the silicon peak was too strong to allow identification of the diamond peak.

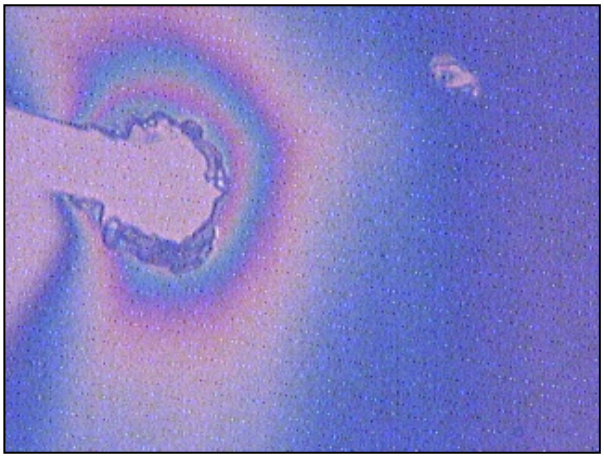

Figure 5.8: Optical image of the region of the sample selected for the study.

Figure 5.9 (a) shows the Raman spectrum obtained from this sample. The rising background slope due to strong photoluminescence from nitrogen vacancy defects has been removed from this spectrum. For comparison, the spectrum of a natural diamond (Figure 5.9 (b)) is presented in the same figure. As expected, the natural diamond displays the strong, sharp, diamond peak at 1332 cm^{-1}, and the absence of any graphitic peaks. Figure 5.9 (a) shows four small peaks between 1100 cm^{-1} – 1700 cm^{-1} and a large peak at approximately 1000 cm^{-1}. This peak due to the silicon substrate is the second-order band related to crystalline silicon, located at 925-1060 cm^{-1}.

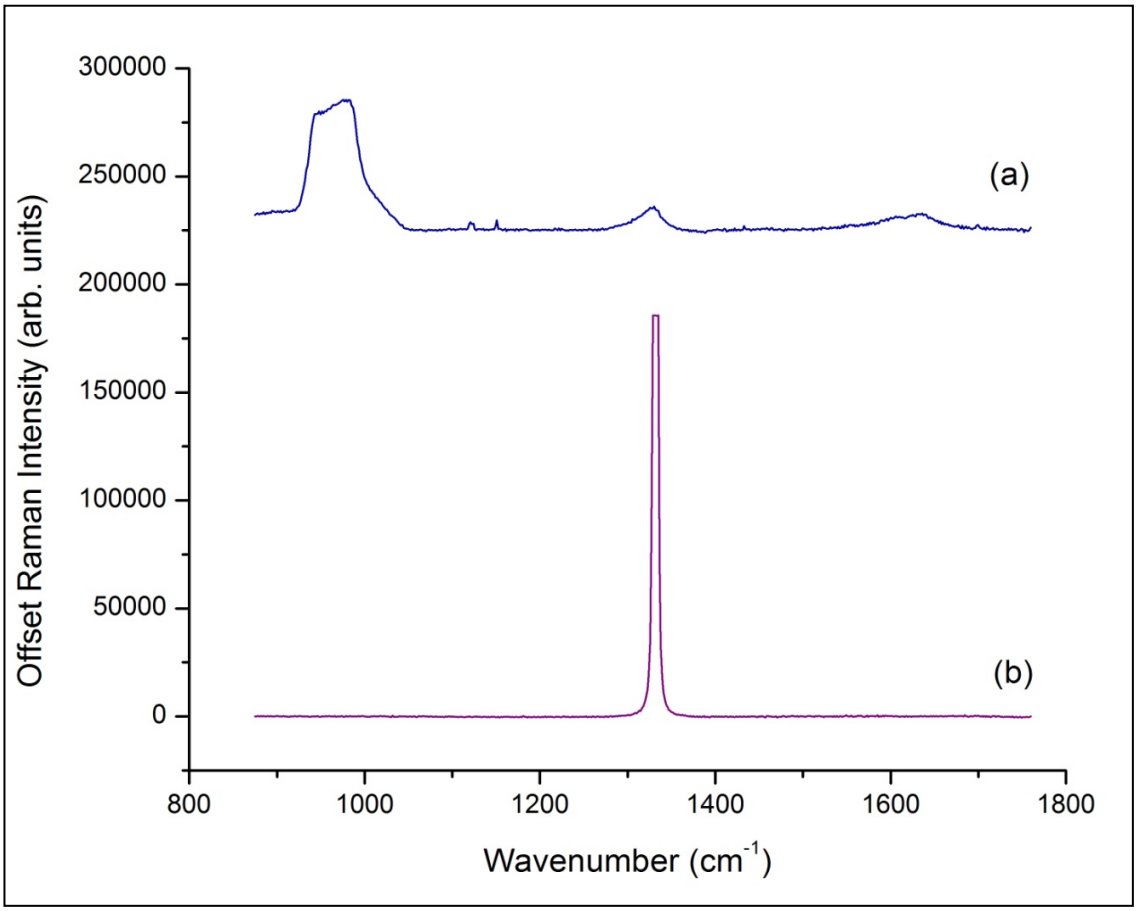

Figure 5.9: (a) Raman spectrum of a thick layer detonation nanodiamond deposited on a silicon substrate compared to (b) bulk natural diamond. Offset for illustration purposes only.

Figure 5.10 displays the Raman spectrum of the nanodiamonds in more detail. The silicon peak has not been included so that the nanodiamond peaks are more apparent. The peaks were fitted, giving peaks centered at 1120 cm^{-1}, 1150 cm^{-1}, 1325 cm^{-1} and 1622 cm^{-1}.

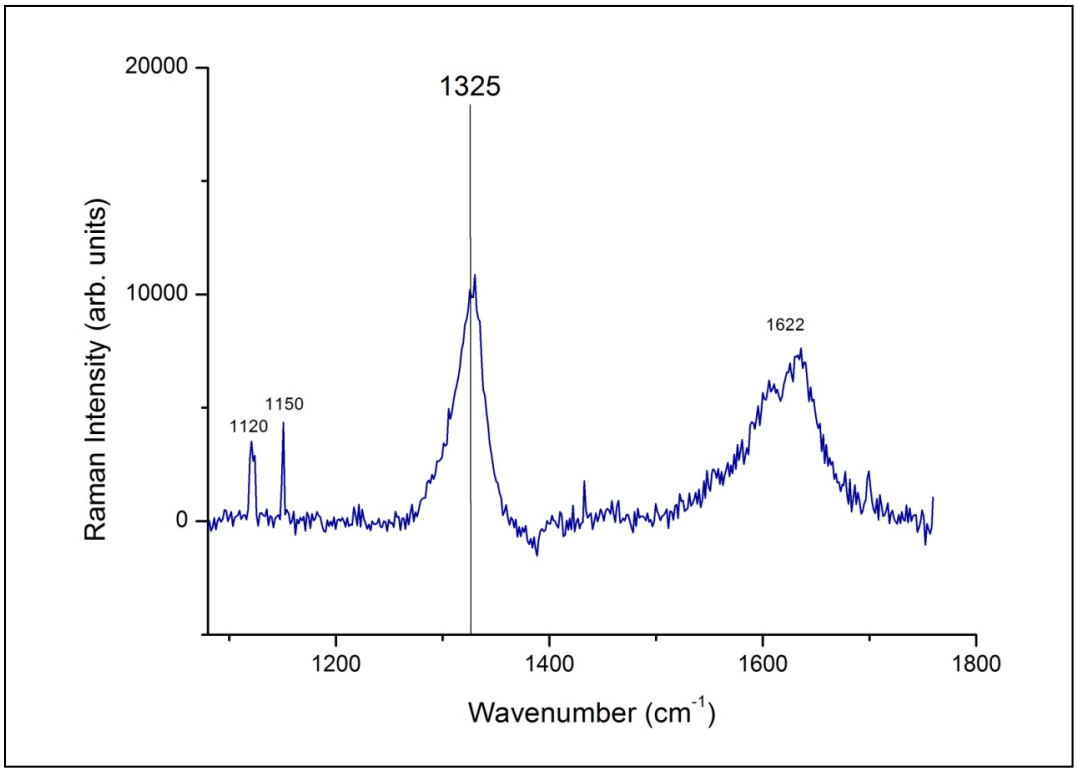

Figure 5.10: Raman spectrum of a thick layer of monodispersed detonation nanodiamond on a silicon substrate, showing the 1120cm^{-} , 1150cm^{-1} 1325cm^{-1} and 1622cm^{-1} peaks.

The origin of the 1150 cm^{-1} peak in nanocrystalline diamond was reported in 2001 by Ferrari *et al.*[5.5] The authors argue that this peak arises from segments of trans-polyacetylene at the grain boundaries and surface of nanocrystatalline diamond.
The peak at 1325 cm^{-1}, with some tailing towards lower frequency, is the first-order Raman mode of the cubic diamond lattice which is broadened and red-shifted compared to bulk diamond. The bulk crystal produces a single sharp peak at 1332 cm^{-1}, due to the zone-centre optical mode. As the crystallite size is reduced to a few hundred nanometres, this peak starts to broaden and shift to a lower frequency due to the relaxation of selection rules. The calculated results for a 5 nm diamond crystallite, reported by Yoshikawa *et al,.*[5.6] predict that the sp^3 Raman peak shows a red-shift of 13 cm^{-1} in energy and a FWHM of 38cm^{-1}. Ager *at al.*[5.7]

reported that when the confinement length reduced from infinite to 5 nm, there is an energy shift of ~6 cm^{-1}, asymmetric line shape, and larger broadening of the calculated Raman line.

This sample shows the peak at 1325cm^{-1} to have a red-shift of 7 cm^{-1} and a FWHM of 32 cm^{-1}, which is in good agreement with the predicted values for 5 nm nanodiamonds.

The Raman signal at approximately 1600 cm^{-1} is due to sp^2 bonding. This Raman signal (the D and G bands as reported in Ref. 5.8) originates from a thin graphite layer on the surface of the nanodiamond. Referring to the result that Raman scattering cross section of diamond is about one-fiftieth of graphite,[5.9] it can concluded that the nanodiamond particles only slightly contain sp^2 material.

Mochalin *et. al.*[5.10] report that it is not possible to obtain a diamond signal using visible Raman. The authors argue that because of the small Raman cross-section of diamond in the visible light and the shielding effect of graphitic and amorphous carbon around the diamond core UV lasers with excitation energy close to the band-gap of diamond (5.5 eV) are needed to amplify the Raman signal of ND. However, although delivering more energy per quantum, the UV lasers heat up samples much more strongly than visible ones, and may lead to thermal damage and changes in sample composition. The spectrum presented here show that the diamond peak is clearly visible for NanoAmando nanodiamonds. This is likely to be as a result of the purification and processing that these nanodiamonds have undergone, resulting in monodispersed particles that have been shown here to have low sp^2 content.

5.4 Concluding remarks

Protocols for the deposition of a densely packed monolayer of ~5nm nanodiamonds have been developed. Substrate choice and the surface condition of the NDs used (chapter 7) mean that attractive zeta potentials lead to a well-adhered layer, in terms of routine laboratory handling. This is a promising result for the potential use of this form of ND in applications where a thin diamond coating on a 2- or 3-D non-diamond substrate would be advantageous. The fact that they can be deposited from a water-based solution at room temperature using

a simple sonication process means that a wide range of substrates can be employed, including those comprising materials that would not be resilient within a standard thin film diamond growth system, which typically operates at 850 °C with a high partial pressure of (chemically active) atomic hydrogen.[511] Such materials could include glass and plastics. The use of Raman spectroscopy has led to the conclusion that the ND particles are indeed crystalline diamond, with little sp^2 content within a densely packed (multilayer) sample. This observation means that these particles can indeed be explored for diamond coating applications, without re-course to conventional thin film diamond growth procedures.

References

5.1 J. Hees, A. Kriele, O.A. Williams, *Chemical Physics Letters*, 509:12–15 (2011).

5.2 A. Chaudhary, J.O. Welch, R.B. Jackman, *Applied Physics Letter*s, 96, 242903, (2010).

5.3 A. Thalhammer**,** R. J. Edgington, L. A. Cingolanic, R.Schoefer**,** *Biomaterials*, 31 (8):2097 (2010).

5.4 E. Osawa, *Pure Applied Chemistry,* 80 (7):1365 (2008).

5.5 A. C. Ferrari, J. Robertson, *Physical Review B*, 63, 121405 (2001).

5.6 M. Yoshikawa, Y. Mori, M. Maegawa, G. Katagiri, H. Ishida, and A. Ishitani, *Applied Physics Letters,* 62, 3114 (1993).

5.7 J. W. Ager III, D. Kirk Veirs, and G. M. Rosenblatt, *Physical Review B*, 43, 6491 (1991).

5.8 M. Yoshikawa, N. Nagai, M. Matsuki, H. Fukuda, G. Katagiri, H. Ishida, and A. Ishitani, *Physical Review B,* 46, 7169 (1992).

5.9 N. Wada, and S. A. Solin, *Physica B,* 105, 353 (1981).

5.10 V. Mochalin, S. Osswald and Y. Gogotsi, *Chemistry of Mateials,.* 21: 273-279, (2009).

5.11 O.A. Williams, M. Nesladek, M. Daenen, S. Michaelson, A. Hoffman, E. Osawa, K. Haenen, R.B. Jackman, *Diamond and Related Materials*, 17: 1080 (2008).

Chapter 6 Electrical properties of detonation nanodiamonds

6.1 Introduction

The various forms of nanometer-scale structured diamonds have been discussed in detail in chapter 2. Detonation nanodiamond (DND) is a powder compromised of 5-10 nm diamond crystals aggregated to the micron scale. Processing techniques which are also discussed in chapter 2 can be applied break apart these aggregates to the 5-10 nm primary particles; the so-called "monodispersed" DND which forms a stable water colloid. DNDs are becoming an increasingly important class of materials being investigated for a diverse range of applications such as, biological cell attachment and growth,[6.1] carriers for *in-vivo* drug delivery,[6.2] fluorescent markers within biological systems,[6.3] additives to oil-based compounds for friction reduction,[6.4] electrodes for electrochemistry,[6.5] and for cold-cathode fabrication through electron field-emission.[6.6]

However, to date the electronic properties of DNDs have not been well characterised. Bevilacqua *et al*.[6.7] studied the electronic properties of micron sized aggregated DNDs using impedance spectroscopy. Only one form of electrical conduction was observed, which was grain-interior-like at temperatures below 350 °C, but may have been due to surface/interface conduction at higher temperatures. The aggregated DND powder also displayed a low dielectric loss tangent (0.004 – 0.008), suggesting it had good dielectric properties. These properties are difficult to explain using the model for DND aggregates that has been proposed whereby the "core" diamond particles are surrounded by sp^2 soot-like phase.[6.8] To better understand the electronic properties of DND material, particularly "core" nanodiamonds, this chapter describes the measurements performed on "monodispersed" DND.

The electrical characterization technique used is impedance spectroscopy (IS), which has been review in chapter 4. IS has been previously deployed to study the properties of single crystal and polycrystalline diamond films to some effect as well as being the technique utilised to study aggregated DND. [6.7, 6.9, 6.10, 6.11, 6.12, 6.13]

6.2. Experimental Method

Sample preparation

The monodispersed DND colloid used throughout this work was purchased from NanoAmando (New Metals & Chemicals Corporation, Japan). This material has been de-aggregated by a process of wet-milling with zircona beads,[6.14] which, along with any additional pretreatment, has been discussed in detail in chapter 2.

In order to measure the monodispersed DND with impedance spectroscopy, it was necessary to coat a smooth, conductive substrate which would act as the electrodes, with DND. For this purpose, one side polished, arsenic doped silicon (resistivity = 0.001 Ωcm) was used. The experiment required the measurements to be conducted through a layer of nanodiamonds, rather than across. Therefore, a sandwich structure was devised, for which two square silicon samples were coated with DND. These would then be placed with the polished DND covered sides, touching each other.

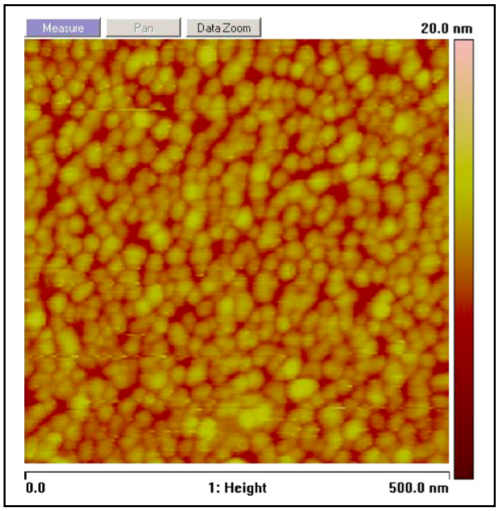

Figure 6.1: AFM image of detonation nanodiamonds on a silicon substrate. The image size is 500 nm x 500 nm. The height scale is given by the gradient scale on the right hand side of the image.

The samples were coated with DNDs using the method described in chapter 5, sample 3. The original solution of DND (50g/L) was diluted to 0.05g/L. The silicon substrate was sonicated in this diluted colloid for 10 minutes. On removal from the colloid, it was immediately rinsed with de-ionised water and dried with

pressurised nitrogen. AFM of the samples revealed a dense monodispersed layer with nanodiamond sizes in the range 5–15 nm (Figure 6.1).

Electrical measurement

For the measurements, one piece of DND coated silicon substrate acted as the bottom electrode while a similar piece of coated silicon was pressed against the topside to act as the other, allowing the measurements to be taken through a layer of DND.

The measurements were carried out using a Solartron 1260 Impedance system with Solartron 1296 Dielectric Interface. The sample structure was placed on a heater in a chamber; the chamber being connected to the Solatron system. Two adjustable probes were used to make contact with both the top and bottom DND coated silicon pieces (Figure 6.2).

Impedance measurements were carried out from room temperature upwards. Each measurement was performed over the frequency range 0.1 Hz–10 MHz. At the point where a significant change in the Cole-Cole plot was recorded, the sample was cooled and a new room temperature measurement was recorded. If little change was observed between this new room temperature measurement and the initial room temperature measurement, the sample was heated to the next highest temperature. This process continued until the room temperature measurement also showed a permanent change. Control experiments using silicon electrodes alone were used to confirm that the electrical measurements recorded were due to the nanodiamond layer alone.

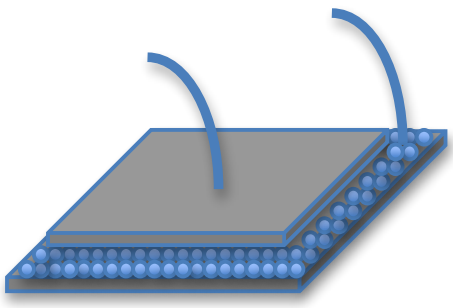

Figure 6.2: Illustration showing the sample set up and probe placement. The grey rectangles depict the silicon substrate, the blue spheres are the nanodiamond particles. One probe is in contact with the back of the top silicon substrate and the other probe is in contact with the bottom substrate.

6.3 Results and Discussion

Figure 6.3 shows the real Cole-Cole plots for the measurements taken at room temperature (23 °C), 75°C, 100 °C, 125 °C and 150 °C. The points represent the experimental data obtained and the solid lines represent the best semicircular fits to the data points using the RC equivalent circuit model described in chapter 4.6. A single semicircular response is apparent, indicating only one significant conduction path is present through the sample.

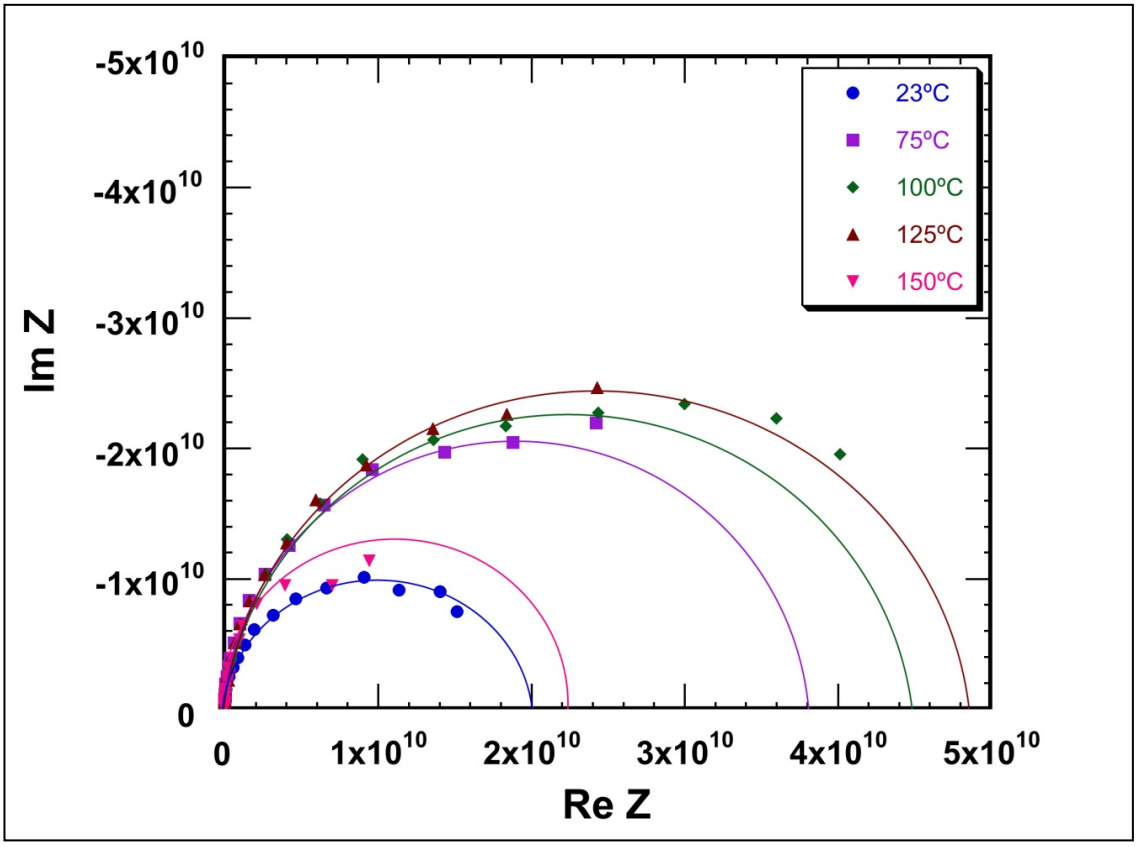

Figure 6.3: Cole–Cole plots (real value of the impedance plotted against the imaginary component as a function of frequency) of the monodispersed nanodiamond layers for temperatures 23 – 150° C. The solid lines are fits to the data points.

Figure 6.4 shows the Bode plot for this same data, where a straight line with a negative slope is apparent at all temperatures. This trend was maintained until samples were heated above 400 °C. At this point no Cole-Cole plots could be recorded and the Bode plot becomes flat with respect to frequency (Figure 6.5). Room temperature measurements recorded after the sample was heated to 425 °C

did not recover their original shape, with the Bode plot remaining flat, although displaying higher resistance values.

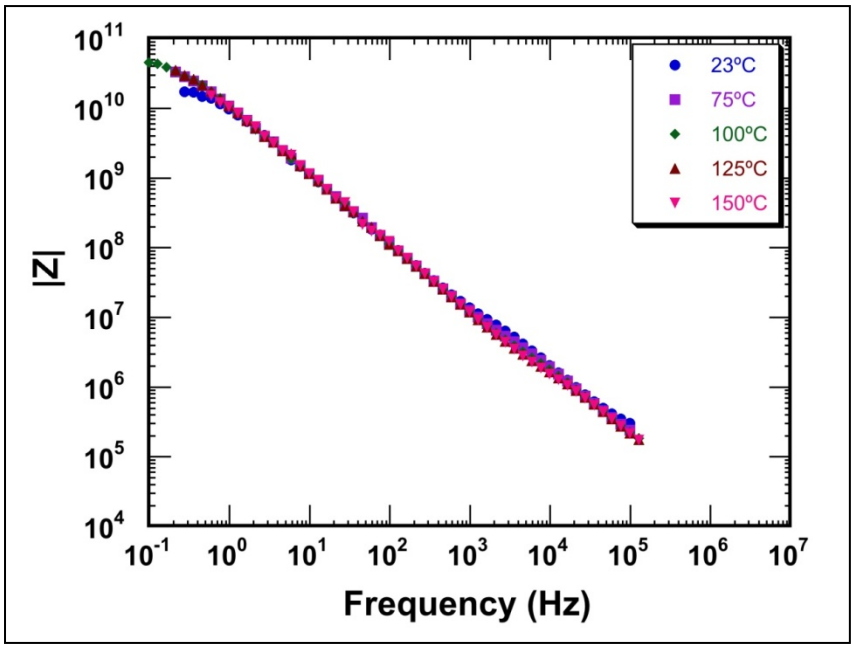

Figure 6.4: Real impedance plotted against measurement frequency (Bode Plot) for the monodispersed nanodiamond layers for temperatures 23-150 °C.

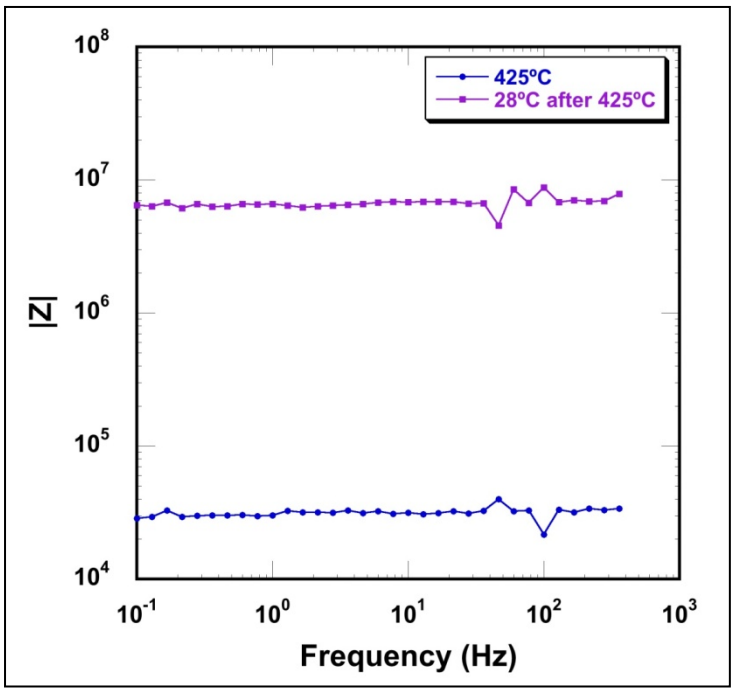

Figure 6.5: Real impedance plotted against measurement frequency (Bode Plot) for the monodispersed nanodiamond layers for temperatures recorded at 425 °C, and at 28 °C following the 425 °C treatment.

The semicircles shown in figure 6.3 can be fitted to extract the RC components of the conduction path responsible for them. This data is shown in table 6.1 as a function of temperature.

Temperature (°C)	**Resistance (x10^{10} Ω)**	**Capacitance (pF)**
23	1.9	11
75	3.9	15
100	4.5	13
125	4.9	9
150	2.2	7

Table 6.1: Resistance and capacitance values derived from the fits to the data shown in Figure 6.3, tabulated against temperature.

Under all conditions the capacitance is seen to be in the picofarad range, which, in polycrystalline material, indicates conduction through grains, rather than grain boundaries that more often display higher capacitance levels (~ nanofarad).[6.15] In the present case, the measurements are being made in the form of a "sandwich" (across the grains attached to the substrate), not through a continuous film. Therefore, this single semicircular response indicates that multiple conduction paths (through the nanodiamond particle and around its shell) are not being observed. The resistance values obtained are greater than 10^{10} Ω which are more typical of diamond than of any *sp^2-like* material surrounding the nanodiamond. This is an indication that any non-diamond carbon present in electrically inactive.

It can be observed that there is an initial increase in resistance, by around a factor of two, with increasing temperature prior to its decrease again at 150 °C. The most likely explanation for this is the desorption of water from the mDND surface, given the high surface area.

Although too few data points exist for an accurate measurement of the activation energy of this process to be determined, an Arrhenius plot of the available data suggests the value is in the range of a few tens of milli-electron-volt; a value that may be expected for removal of moisture from the samples. The Bode plot shown in figure 6.4 is typical for a good quality dielectric material, where effective resistivity declines with measurement frequency. Extrapolation of the line

displayed in figure 6.4 towards zero frequency enables the dc resistivity of the film to be determined, revealing a value greater than 10^{12} Ω/ sq. This value is only around an order of magnitude lower than that determined for high quality polycrystalline CVD material[6.16] and is a remarkable result given that this is nanostructured detonation powder, which has often been considered to comprise a composite of sp^3, sp^2, and impurity species.[6.17, 6.18] An important characteristic of an insulating film is the dielectric loss tangent (tan δ), determined as a function of ac frequency. tan δ is the imaginary part of the complex dielectric constant as a ratio with its real component; it can be shown that the value is equal to the ratio of the real part of the complex impedance (Z') divided by its imaginary component (Z").[6.15] For the data shown in figure 6.2, tan δ is around 0.5 at 0.1 Hz, falling to ~0.05 at 1MHz.

It should be remembered the function tan δ is a measure of the ratio of the power dissipated in the dielectric to the power stored, implying low numbers are desirable. Ibarra and co-workers [6.19] measured a dielectric loss tangent of around 0.01 falling to around 0.001 at 10 MHz for commercially available thick CVD polycrystalline diamond films. The values measured here are only around one order higher, further underlining that the DND samples are showing high quality dielectric characteristics. In a previous study,[6.20] on aggregated DND material, the dielectric loss values ranged from 0.4 to 0.02, suggesting any change to the dielectric properties of the DND created by monodispersing them are not significant.

At higher temperatures, measurements became increasingly noisy to record and by 400 °C the dielectric character of the samples is essentially lost (Figure 6.5). This change was not reversible by subsequently cooling the samples, which indicates a structural change has occurred. Diamond graphitization in a vacuum involves temperatures in excess of 1000 °C,[6.21] although in air diamond burns at temperatures considerably lower than this.[6.22] Given that the resistivity is considerably reduced in the current case, and the impedance measurements lose any dependence on measurement frequency, this suggests the nanodiamonds have irreversibly transformed to a non-diamond carbon state. Such a catastrophic loss of diamond character was not observed in previous studies of aggregated DND,[6.20]

although there was evidence for the onset of some grain-boundary-like electrical conduction at temperatures above 350 °C. Further studies are required to be able to identify the nature of the transformation that has taken place in the current study. However, theoretical studies have suggested individual nanodiamonds, with a diameter of around 5 nm, will support a fullerene-like outer shell, and have been called "bucky-diamonds;"[6.23,6.24,6.25] it could be speculated that transformations within these phases are responsible for the loss of diamond characteristics, or that the nanometer size of the DND particles enables graphitisation to occur at considerably lower temperatures than in the case of bulk-crystalline diamond. Graphitisation (or otherwise) of the DND particles can be investigated by performing Raman spectroscopy on the sample after heating to 425 °C in air.

6.4 Concluding remarks

The electrical properties of monodispersed detonation nanodiamonds have been studied; a resistivity of the order of 10^{12} Ω/sq has been determined, with only one significant conduction pathway being observed. This suggests either the nanodiamonds support little in the way of sp^2-like material on their surfaces, or any such material is electrically inactive, presumably through depletion. The dielectric character of the detonation nanodiamond particles is also good, with dielectric loss tangent values in the range 0.05 – 0.5 being recorded. These combined observations suggest DNDs behave in electrical terms similar to thin film diamond, and that electrical applications for DNDs are worthy of pursuit. Since the simple room temperature sonication process used here is capable of coating a wide-range of three-dimensional objects with DND layers this is an exciting result. A limitation on the electrical use the monodispersed DNDs, at least in the untreated, as-deposited from solution form used here, is the catastrophic loss of diamond like character at temperatures above 400 °C.

References

6.1 A. Thalhammer, R. J. Edgington, L. A. Cingolani, R. Schoepfer, and R. B. Jackman, *Biomaterials* 31, 2097 (2010).

6.2 K. V. Purtov, A. I. Petunin, A. E. Burov, A. P. Puzyr, and V. S. Bondar, *Nanoscale Res. Lett*. 5, 631 (2010).

6.3 L. C. L. Huang and H. C. Chang, *Langmuir* 20, 5879 (2004).

6.4 V. Yu. Dolmatov, *Journal of Superhard Materials,* 32, 14 (2010).

6.5 J. B. Zang, Y. H. Wang, S. Z. Zhao, L. Y. Bian, and J. Lu, *Diamond Related Materials*, 16, 16 (2007).

6.6 D. He, L. Shao, W. Gong, E. Xie, K. Xu, and G. Chen, *Diamond Related Materials*, 9, 1600 (2000).

6.7 M. Bevilacqua, A. Chaudhary, R.B. Jackman, *Journal of Applied Physics*, 106, 12: 123704 (2009)

6.8 A. Krüger, F. Kataoka, M. Ozawa, T. Fujino, Y. Suzuki, A. E. Aleksenskii, A.Y. Vul' and E. Ōsawa, *Carbon* 43, 1722 2005.

6.9 H. Ye, O. A. Williams, R. B. Jackman, R. Rudkin, and A. Atkinson, *Phys. Status Solidi A* 193, 462 (2002).

6.10 H. T. Ye, R. B. Jackman, and P. Hing, *Journal of Applied Physics*. 94, 7878 (2003).

6.11 H. T. Ye, O. Gaudin, R. B. Jackman, P. Muret, and E. Gheeraert, *Physica Status Solidi A,* 199, 92 (2003).

6.12 S. Curat, H. Ye, O. Gaudin, R. B. Jackman, and S. Koizumi, *Journal of Applied Physics*, 8, 073701 2005.

6.13 L. L. Hench and J. K. West, *Principles of Electronic Ceramics* Wiley, New York, 1989, Chap. 5.

6.14 E. Osawa, *Pure Applied Chemistry*, 80 (7): 1365 (2008).

6.15 L. L. Hench and J. K. West, *Principles of Electronic Ceramics* Wiley, 225 New York, 1989, Chap. 5.

6.16 J. R. Brandon, S. E. Coe, R. S. Sussmann, K. Sakamoto, R. Sporl, R. Heidinger, and S. Hanks, *Fusion Engineering and Design*, 53, 553 (2001).

6.17 O. A. Shenderova, V. V. Zhirnov, and D. W. Brenner, *Critical Reviews in Solid State and Materials Sciences,* 27, 227 (2002).

6.18 T. Hamilton, E. Z. Kurmaev, S. N. Shamin, P. Y. Detkov, S. I. Chukhaeva, and A. Moewes, *Diamond Related Materials*, 16, 350, (2007).

6.19 A. Ibarra, M. Gonzalez, R. Vila, and J. Molla, *Diamond Related Materials*, 6, 856 (1997).

6.20 M. Bevilacqua, S. Patel, A. Chaudhary, H. Ye, and R. B. Jackman, *Applied Physics Letters*, 93, 132115 (2008).

6.21 M. Seal, *Nature*, 185, 522, (1960).

6.22 J. K. Lee, M. W. Anderson, F. A. Gray, P. John, J. Y. Lee, Y. J. Baik, and K. Y. Eun, *Diamond Related Materials*, 13, 1070 (2004).

6.23 J. Y. Raty and G. Galli, *Computer Physics Communications*, 169, 14 (2005).

6.24 J. Y. Raty and G. Gallia, *Journal of Electroanalytical Chemistry*, 584, 9 (2005).

6.25 A. S. Barnard, *Diamond Related Materials,* 15, 285 (2006).

Chapter 7 Modification of nanodiamond layer surfaces

7.1 Introduction

The as-received detonation nanodiamond is covered with surface functional groups dependent on the post detonation treatments for cleaning and deaggregation, as discussed in chapter 2.1.4. Mainly due to oxidising post-synthesis treatments, DNDs are covered by a wide variety of oxygenated functions: hydroxyl, ether, ketones or carboxylic acid groups.[7.1] This variation in surface chemistry prevents an efficient and homogenous functionalisation due to different reactivity of these various oxygenated groups.

By analogy with diamond films, another promising way to homogenise the nanodiamond surface is by hydrogenation. By reducing all oxygenated terminations into C–H groups, this treatment ensures a reproducible and versatile surface for further functionalisation. This has previously been attempted by MWPCVD hydrogenation.[7.2] This chapter will report on the results obtained by using a hydrogen gas treatment to successfully reduce the surface to C-H groups. In addition to this, how the surface can be oxidised using ozone to provide a platform for metallisation.

To obtain an NEA surface of the nanodiamond layer, two approaches can be used. The first is to simply hydrogen terminate the entire surface, which is not considered to be a particularly stable NEA as oxidation of the surface can readily lead to hydrogen loss. The second is to deposit a metallic layer such as caesium. For electron emission applications, a caesium submonolayer adsorbed on the oxygenated diamond surface has been investigated extensively due to the extremely low work function induced by the large Cs—O dipole, reducing the work function of the bare diamond surface from 5.5–6 eV to around 1.25 eV.[7.3, 7.4] Another particularly important question is how strongly the Cs atoms are bound to the surface; if the bonding is weak the system would not be robust. Geis found the oxygenated diamond surface after caesiation to be very stable.[7.5] It is therefore important to investigate treatments that will render the nanodiamond surface

terminated with oxygen groups to provide a platform for caesium deposition resulting in enhanced NEA. The carbonyl (or ketone) structure, consisting of a double bond between carbon and oxygen above every surface site, has been calculated to be slightly higher in energy than the ether bridging structure where oxygen atoms bond between and across atomic sites.[7.6] The aim of this investigation is to not only establish a protocol for successful oxidation but also to establish a method of preferential termination with ketones.

FTIR is a useful technique to identify the chemical bonding. FTIR has been extensively used to investigate the presence of various functional groups on the surface of NDs.[7.7, 7.8, 7.9, 7.10] It was therefore chosen as the analytical technique for this work due and has been described fully in chapter 4.
Many authors report the use of KBr pellets to perform FTIR of nanodiamonds.[7.11] However, since the treatments in this work were conducted on nanodiamond layers deposited from a colloid, KBr discs were not a suitable medium for two reasons. The first being the exposure to water from the nanodiamond containing colloid (KBr is water soluble) and the second, the high temperatures of some of the treatments. Silicon was also not a suitable substrate due to phonon creation and the unpolished surface causing infrared scattering. Calcium fluoride windows (15mm discs) were found to be an appropriate alternative. However, with the FTIR equipment available it was not possible to obtain a spectrum from DND monolayers, so the windows were coated with a thick layer of DNDs.

7.2 Method sample of preparation

A small volume of the original nanodiamond colloid of concentration 50 g/L was used to create a dilution of concentration 3.33 g/L. The CaF_2 window was placed on a heater at a temperature of approximately 100°C. The diluted colloid was picked up using a micropipette and dropped onto the window. The water evaporated, leaving a coating of nanodiamonds on the window (Figure 7.1).

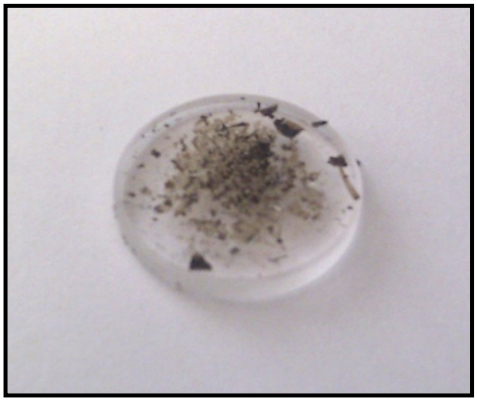

Figure 7.1: CaF_2 window with dried nanodiamond particles.

List of ND treatments for FTIR spectroscopy

The FTIR spectrometer was purged with nitrogen to reduce the effect of moisture in the spectra. The spectra were obtained in transmission mode.

Spectra obtained :

CaF_2 uncoated (background).

CaF_2 nanodiamond untreated.

CaF_2 nanodiamond, treated with the hydrogen process.

CaF_2 nanodiamond, treated with the ozone process.

CaF_2 nanodiamond, treated with hydrogen followed by ozone.

CaF_2 nanodiamond treated with an oxygen reactive ion etching (RIE) plasma.

7.2.1 Hydrogen treatment

To hydrogenate the ND surface, the sample was heated in an atmosphere of hydrogen for 5 hours at 500 °C. This treatment was conducted in a custom built chamber with a heating plate. The nanodiamond coated CaF_2 window was placed on the heater in the centre of the chamber.

Treatment steps

- The chamber was pumped down to 10^{-5} torr using the turbo pump. Once this pressure was reached the turbo pump was turned off.
- The hydrogen gas values were opened and flow of hydrogen entered the chamber until the pressure in the chamber reached 10 torr. To maintain this pressure, the valve on the rotary pump was adjusted accordingly.
- The temperature controller for the heating plate was set to 500 °C and the sample heated. The sample was left in these conditions (10 torr of H_2 and 500 °C) for 5 hours.
- Once the 5 hours had elapsed, the heating plate was cooled whilst still maintaining the 10 torr of H_2 pressure. When the heating plate had reached room temperature, the hydrogen flow to the chamber was stopped and all the gas line valves were closed.
- The chamber was pumped down to a rough vacuum to remove the hydrogen before bringing it up to atmospheric pressure to open. The sample was then immediately transferred to the FTIR for measurement or to the equipment for oxidation using ozone.

7.2.2 Ozone treatment

This treatment was carried out for 30 minutes at 200 °C using ozone gas. The ozone was produced by the Ozonia TOGC2-100201. The TOGC2 is a corona discharge type ozone generator with variable ozone output. Producing up to 4g/h using dry air and 10g/h using oxygen.

Treatment steps

- The sample was placed on a heater inside the custom built chamber.
- The chamber was pumped to low 10^{-2} torr, using the rotary pump but through the turbo pump connection. Whilst pumping, the chamber was open to a flow of oxygen via a valve fitted connection and through the TOGC2. The flow duration was 30 seconds. The valve was then closed and the chamber again pumped to low 10^{-2} torr. The purpose of this step was to flush the lines with oxygen gas prior to treating the sample. The turbo pump

was then started and the chamber was pumped down to 10^{-5} torr. The sample was then heated to 200°C and this temperature was maintained.

- The oxygen gas line is connected to the chamber via the TOGC2. Oxygen was introduced into the chamber by opening the required valves, allowing the pressure to rise slowly, the turbo pump was turned off and the valve connecting the chamber to the turbo pump was closed. The valve connecting the chamber directly to the rotary pump was opened. Using a combination of the oxygen variable area flow meter and the rotary pump valve, a chamber pressure of 50 mbar was established and maintained.
- The ozone production was started by turning on the TOGC2 unit and continued for 30 minutes. After 30 minutes, the sample was cooled down in ozone. Once the sample had reached room temperature, the TOGC2 ozone production was stopped, the oxygen flow to the chamber was shut off and the chamber was pumped down to remove gases before venting. The sample was immediately transferred to the nitrogen purged FTIR.

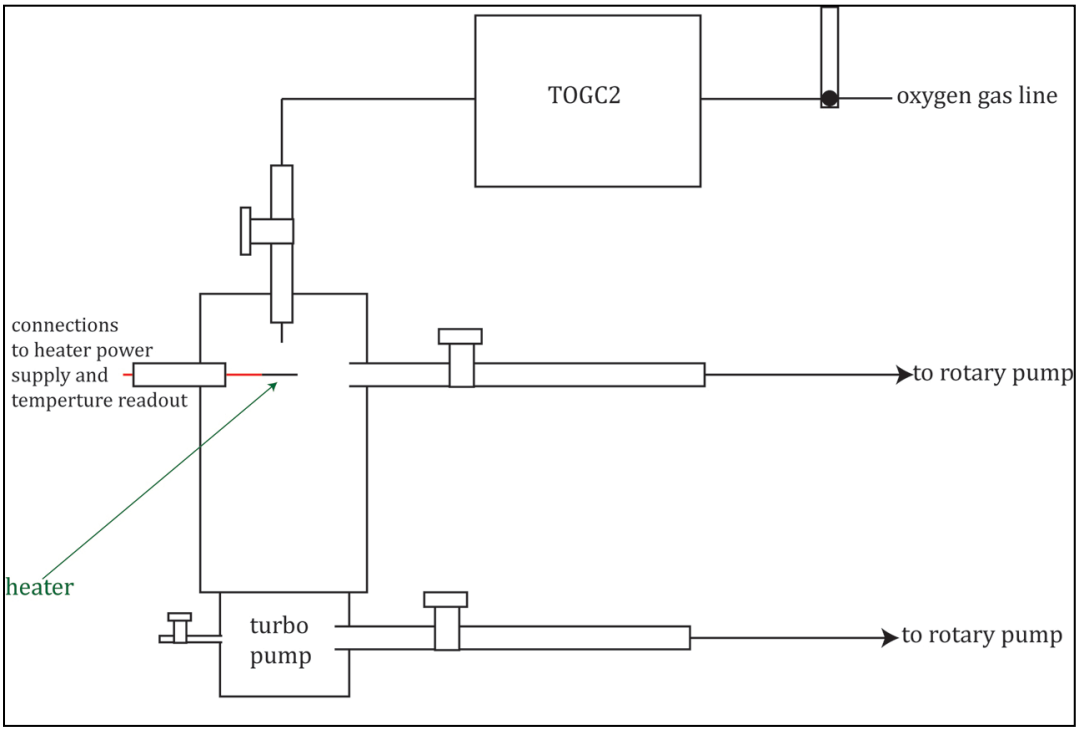

Figure 7.2: Schematic diagram of the ozone treatment chamber, showing the heater on which the sample is placed, with the gas line directly above.

7.2.3 RIE treatment

Another approach used for the oxidation of the DND surface is the use of reactive ion etching, using 100 % oxygen gas plasma. The equipment used was an Oxford Plasma Technology RIE80 with parallel plates. RIE is generally used as an etching technology, using a chemically reactive plasma to remove material deposited on wafers. The plasma is initiated in the system by applying a strong RF (radio frequency) electromagnetic field to the wafer platter. The field is typically set to a frequency of 13.56 MHz applied at a few hundred watts. The oscillating electric field ionises the gas molecules by stripping them of electrons, creating a plasma. In each cycle of the field, the electrons are electrically accelerated up and down in the chamber, sometimes striking both the upper wall of the chamber and the wafer platter. At the same time, the much more massive ions move relatively little in response to the RF electric field. When electrons are absorbed into the chamber walls they are simply fed out to ground and do not alter the electronic state of the system. However, electrons stripped from the wafer platter cause the platter to build up charge due to its DC isolation. This charge build up develops a large positive voltage on the platter, typically around a few hundred volts. The plasma itself develops a slightly negative charge due to the higher concentration of negative ions compared to free electrons. Because of the large voltage difference, negative ions tend to drift toward the wafer platter, where they collide with the samples to be etched. The ions react chemically with the materials on the surface of the samples, but can also sputter some material by transferring some of their kinetic energy. In this case, surface oxidation is desired through the oxygen species created in the plasma react with the sample surface.

The sample is placed on the wafer platter, and the air is evacuated from the process chamber using a system of vacuum pumps. The process gas (oxygen) is then introduced at low pressure, until the process pressure is reached. The plasma is then initiated by applying the RF potential. For this particular equipment, it was not possible to initiate the plasma at different conditions and thus the only variable was the process time.

Process Parameters

Process pressure = 200 mtorr; RF power = 350 W; Treatment time = 15 mins

7.3 Results and discussion

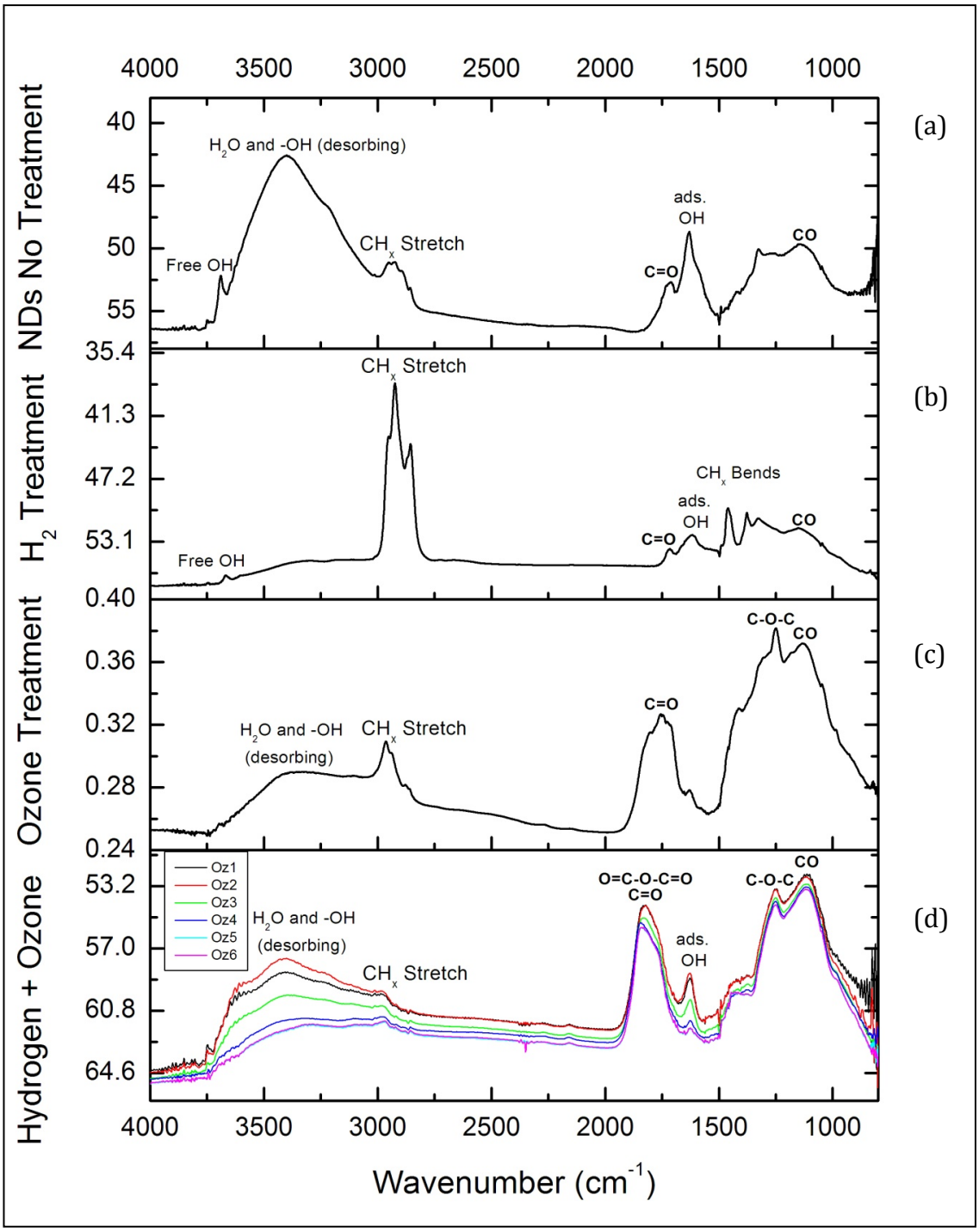

Figure 7.3: FTIR spectra of (a) untreated nanodiamonds, (b) nanodiamonds with hydrogen treatment, (c) nanodiamonds with ozone treatment and (d) nanodiamonds treated with ozone following hydrogen treatment.

The FTIR spectrum of the as-received NDs is shown in figure 7.3 (a). The band observed at 1726 cm^{-1} is characteristic of the C = O stretching band involved in carboxylic acid groups and anhydride functionalities.[7.12] This band is less intense after hydrogen treatment. The wide peak in the 3000-3600 cm^{-1} range is attributed to OH of adsorbed water. In the 1000–1500 cm^{-1} range, complex mixed peaks characteristic of nanodiamond surface groups such as C–OH, COO^-, C–O–C, C–H, etc. are observed.[7.13]

The hydrogen treated FTIR (Figure 7.3(b)) spectrum shows a strong peak at 2923 cm^{-1}, this band has previously been assigned to the C–H stretching of the hydrogenated ND surface.[7.14] This is coupled with the CH_x bends at 1461 cm^{-1} (CH_2) and 1377 cm^{-1} (CH_3) which are not observed in the untreated DND spectrum. The free and adsorbed –OH peaks are also much less intense after hydrogen treatment and there appears to be little moisture on the sample.

Figure 7.3 (c) shows nanodiamonds with ozone treatment only. The CH_x stretch is still quite prominent but there does seem to be a level of oxidation taking place. There appears to be a C=O stretching band at 1755 cm^{-1} superimposed on the anhydride peak. It is difficult to distinguish peaks in the fingerprint region but the peaks at 1249 cm^{-1} and 1141 cm^{-1} can be attributed to C-O-C and C-O respectively.

Ozone treatment following hydrogenation (Figure 7.3 (d)) has reduced the CH_x significantly so that it is only just observable. The main band is at 1801 cm^{-1} which is attributed to cyclic acid anhydride structures. This is coupled with the peaks at 1123 cm^{-1} attributed to C-O and 1256 cm^{-1} of C–O–C, of carboxylic acids and anhydrides. These peaks are stronger and more defined than with ozone treatment only. In addition the spectrum suggests that to fully oxidise the surface of the nanodiamonds, previous hydrogen treatment is necessary. There also appears to be more water adsorbed on the nanodiamonds in the hydrogen plus oxygen spectrum, which can be seen desorbing over time in the nitrogen purge, as witnessed by the decreasing intensity of the band in the region 3000 – 4000 cm^{-1}. This suggests that the layer should be well dried before use.

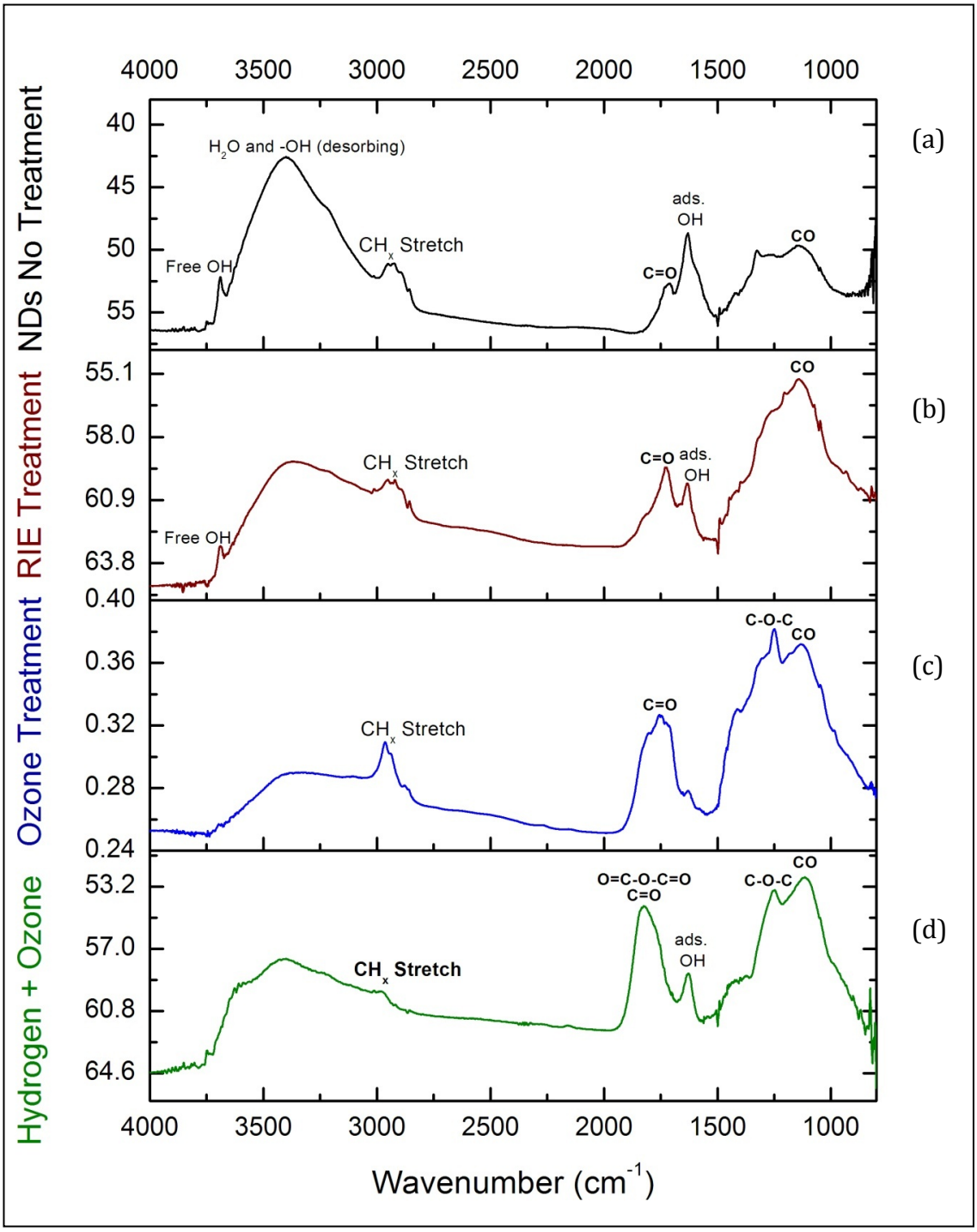

Figure 7.4: FTIR spectra of (a) untreated nanodiamonds, (b) nanodiamonds after RIE oxygen plasma treatment, (c) nanodiamonds with ozone gas treatment and (d) nanodiamonds treated with ozone gas following hydrogen treatment.

Figure 7.4 shows the spectra obtained from the two ozone treatments compared to oxygen plasma (RIE) treatment. Interestingly, the only significant change compared to the pre-treatment spectrum is that the C=O stretch of carboxylic acid

and C-O peaks are more intense after oxygen plasma treatment. There is no strong evidence for cyclic acid anhydride structures.

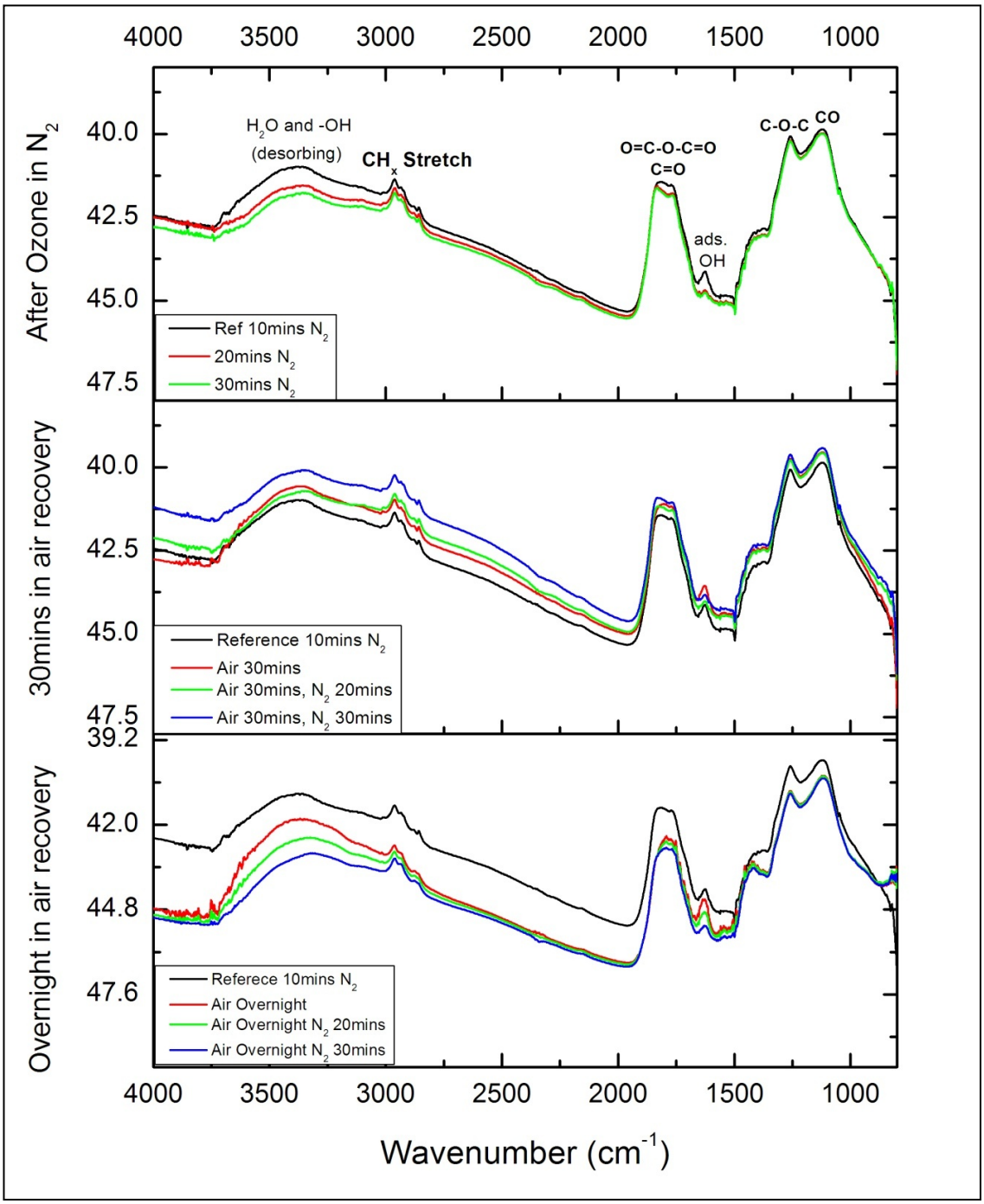

Figure 7.5: Spectra of hydrogen plus ozone treated nanodiamonds and their stability when exposed to air and recovery in the FTIR under nitrogen.

Figure 7.5 shows water desorbing from a hydrogen plus ozone treated nanodiamond sample under a nitrogen atmosphere. We can observe that even overnight in normal atmospheric conditions does not change the spectrum. The moisture that adsorbs on the nanodiamonds is readily desorbed under nitrogen once again. We can conclude that samples treated in this way do not need to be stored in special conditions but they do need drying under vacuum before a reaction with caesium or any measurement.

Figure 7.6 displays the FTIR spectra of untreated NDs compared to MWPCVD hydrogen plasma treated ND's from the study by Arnault *et al*.[7.2] Two points of note are that (1) the CH_x peak is not as large and sharp as the peak displayed in this work (Figure 7.3 (b)) and (2) a large band of superimposed peaks in the range 1000 – 1500 cm^{-1} characteristic of nanodiamond surface groups such as C–OH, COO^-, C–O–C, C–H are still present. These groups are greatly reduced by the hydrogen annealing treatment described in this chapter.

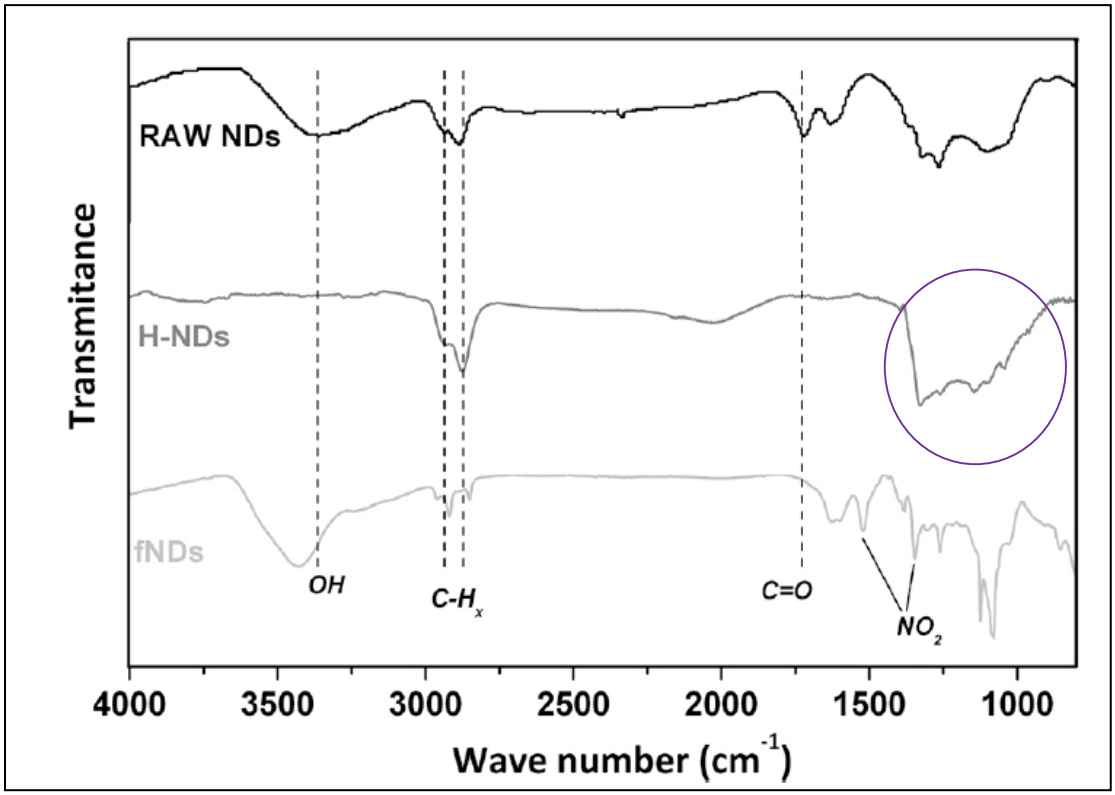

Figure 7.6: FTIR spectra of raw, whole-surface hydrogenated (H-NDs) and functionalised diazonium (fNDs) detonation nanodiamond (taken from Ref. 7.2). The circle highlights the peask in ths 1000 – 1500 cm^{-1}range.

The authors also mention that the efficiency of such plasma to remove carbon–oxygen bonds at the ND surface was demonstrated for a temperature higher than 700 °C and that a part of the initial oxygen content remained for lower surface temperatures (i.e. T = 520 °C). The hydrogen treatment shown in this chapter is effective at lower temperatures (500 °C) to remove many of the surface oxygen containing groups and there is a strong presence of the CH_x peak. Since this treatment is conducted on the ND surface to air, after deposition, it is expected that the remaining oxygen containing groups displayed in the FTIR are on parts of the ND surfaces that the hydrogen gas could not reach.

An alternative for the oxidation of nanodiamond ("carboxylated" nanodiamond) is based on strong acid treatments (wet chemistry). This technique is now quite common and carboxylated nanodiamonds can also be purchased in colloid form. However, these nanodiamonds have a negative zeta potential and will not electrostatically attach onto substrates in the manner described in this work. The gaseous method described in this chapter, allows nanodiamonds to be deposited with ease and then subsequently treated for the desired outcome; hydrogenated or oxidised NDs.

Shenderova *et al.*[7.15] report on the use of ozone purification to oxidise nanodiamonds, concluding that carboxylic anhydride groups prevail on the surface. The authors used ozone purification on larger sized (80 nm), aggregated nanodiamonds and compared this treatment with air oxidation (NDS). The obtained FTIR spectrum (NDO) in figure 7.7 looks remarkably similar to the hydrogen+ozone treated nanodiamonds in figure 7.3. However, whereas the authors treated their nanodiamonds at 150 – 200 °C for 72 hours, in this work it was achieved in 30 minutes at 200 °C which we can conclude is as a result of the prior hydrogen treatment.

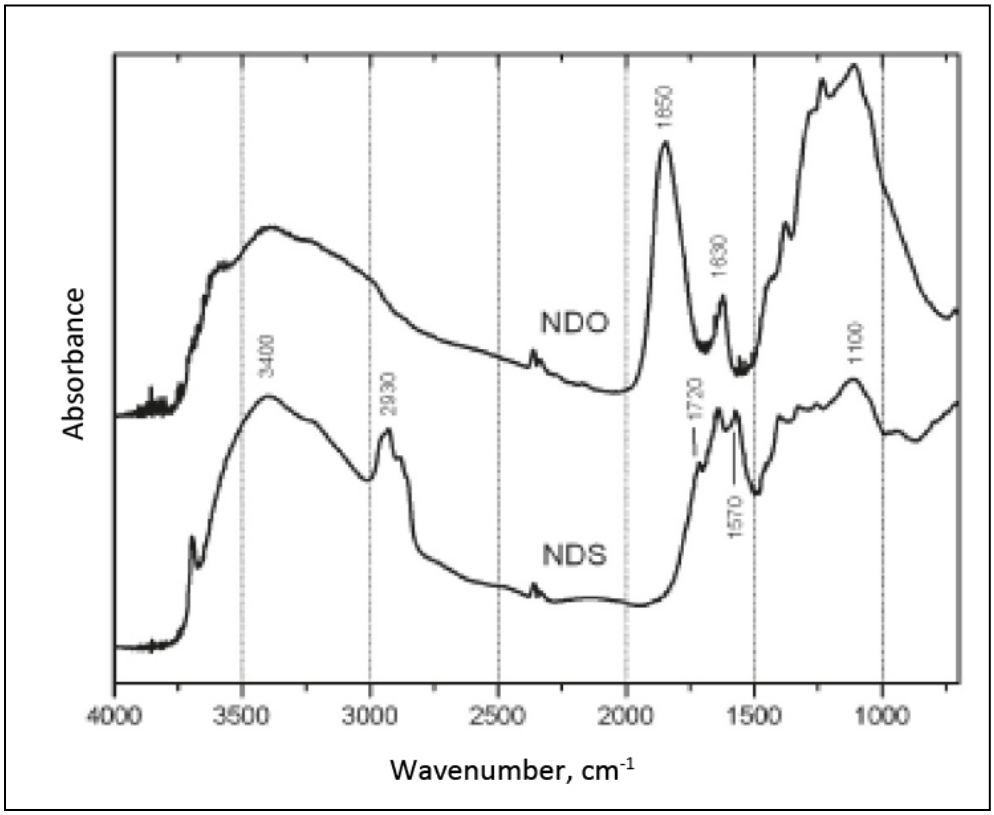

Figure 7.7: FTIR spectra of NDO and NDS (taken from Ref. 7.15).

7.4 Concluding remarks

In summary, initial hydrogenation is important to homogenise the nanodiamond surface by removing oxygen containing groups and replace them with hydrogen terminations. Ozone treatment following this is successful in removing the hydrogen terminations and replacing them with oxygen containing groups, more so than ozone treating nanodiamonds directly. Additionally the ozone treatment post-hydrogenation displays the presence of more of the important ketone groups. An efficient protocol for the oxidation of nanodiamond surfaces has been established.

Further work is required to study these treatments on nanodiamond layers, especially for monolayer coatings on silicon. We are investigating the possibility of doing this with attenuated total reflection FTIR. These measurements can be complemented by X-ray photoelectron spectroscopy.

References

7.1 A. Kruger, Y. Liang, G. Jarre and J. Stegk, *Journal of Materials. Chemistry,* 16. 2322 (2006).

7.2 J-C. Arnault, T. Petit, H. Girard, A. Chavanne, C. Gesset, M. Sennourb, M. Chaigneauc, *Physical Chemistry Chemical. Physics,* Advanced Online Publication DOI:10.1039/c1cp20109c

7.3 K. P. Loh, J. S. Foord, R. G. Egdell, and R. B. Jackman, *Diamond Related. Mateials*, 6, 874 (1997).

7.4 W.E. Picket, *Physical Review Letters*, 73, 12, 1664 (1994)

7.5 M. Geis, J. Twichell, J. Macaulay, and K. Okano, *Applied Physics Letters,* 67, 1328 (1995).

7.6 K. M. O'Donnell, T. L. Martin, N. A. Fox and D. Cherns, *Physical Reveiw B*, 82 115303 (2010).

7.7 D. Mitev, R., Dimitrova, M., Spassova, Ch. Minchev, S., Stavrev, *Diamond and Related Materials*, 16, 776 (2007).

7.8 B.V. Spitsyn, J.L. Davidson, M.N. Gradoboev, T.B. Galushko, N.V. Serebryakova, T.A. Karpukhina, I.I. Kulakova, N.N. Melnik, *Diamond & Related Materials*, 15, 296 (2006).

7.9 A. Krueger and T. Boedeker, *Diamond and Related Materials*, 17, 1367 (2008).

7.10 M.A. Ray, O. Shenderova, W. Hook, A. Martin, V. Grishko, T. Tyler, G.B. Cunningham, G. McGuire, *Diamond and Related Materials*, 159, 1809 (2006).

7.11 O. Shenderova, I. Petrov, J. Walsh, V. Grichko, T. Tyler, G. Cunningham, *Diamond & Related Materials,* 15, 1799 (2006).

7.12 P. Chung, E. Perevedentseva, J. Tu, C. Chang, C. Cheng, *Diamond & Related Materials,* 15, 622 (2006).

7.13 C.D. Chu, E. Perevedentseva, V. Yeh, S.J. Cai, J.S. Tu, C.L. Cheng, *Diamond and Related Materials*, 18, 76 (2009).

7.14 C. Cheng, C. Chen, W. Shaio, D. Tsai, K. Chen, *Diamond & Related Materials*, 14, 1455 (2005).

7.15 O. Shenderova, A. Koscheev, N. Zaripov, I. Petrov, Y. Skryabin, P. Detkov, S. Turner, and G. Van Tendeloo, *The Journal of Physical Chemistry C,* 115, 9827 (2011).

Chapter 8: Secondary electron emission from nanodiamond layers

8.1 Introduction

As discussed in chapter 3, improvement of an image intensifier would rely on the ability of the microchannel plate (MCP) to create a higher number of secondary electrons per input electron, particularly at the input stage of the MCP where any incident electrons that do not create secondary electrons mean that the photon that created them has effectively been 'lost' to the device. Thus, increasing the secondary electron yield at the entrance of the MCP, the first interaction, would improve the signal to noise ratio and the efficiency of light capture.

One approach could be to grow diamond all over the MCP, however the temperatures required for diamond growth are not compatible with the MCP material. A temperature above 400 °C would begin to cause warping of the MCP which is made from a proprietary silicon dioxide based material. The last few chapters have shown that surfaces can be easily coated with a layer of nanodiamonds, which exhibit good diamond characteristics. If the MCP can be coated with a layer of nanodiamonds, treated to maximise the secondary electron yield, the performance of an image intensifier would be greatly increased in terms of better signal to noise ratio thereby increasing image contrast and resolution. The premise of this chapter is the investigation of the secondary electron yield from the most simple surface; untreated nanodiamonds, followed by the investigation into various surface treatments to enhance the SEY.

8.2. Experimental method

The secondary electron yield of the nanodiamond layers was measured by bombardment with a continuous electron beam from an electron gun (Kimball Physics EGG-301), i.e. primary electrons. A negative voltage was applied to the sample in order to prevent the emitted secondary electrons (SEs) from returning to the sample. The energy of the primary electrons (E_p) was varied by controlling the kinetic energy of the incident electrons emitted from the electron gun and also by varying the sample bias (V_b) in the negative regime. The primary electron

energy (E_p) is defined as E_a + eV_b, where E_a is the initial kinetic energy of the primary electrons from the electron gun. The magnitude of the primary electron current (I_p) as a function of primary electron energy was measured by applying +500 V to the sample holder before the measurement of SEE yield (δ).

The electron gun was set-up in a custom built high vacuum chamber (base pressure 1×10^{-7} mbar), with the sample stage perpendicular to the beam line.

Prior to sample measurements, the electron gun operating characteristics were obtained. A phosphor coated silicon wafer was placed on the sample stage in the beam line. This allowed calibration of the electron gun focus voltage, grid voltage and x-y deflection at each required beam energy to obtain a 2 mm diameter beam spot in the centre of the wafer. This is shown in figure 8.1 where the left hand image shows the luminescence from a focussed spot used for the experiments performed here, whilst the right hand image shows luminescence from a defocussed beam.

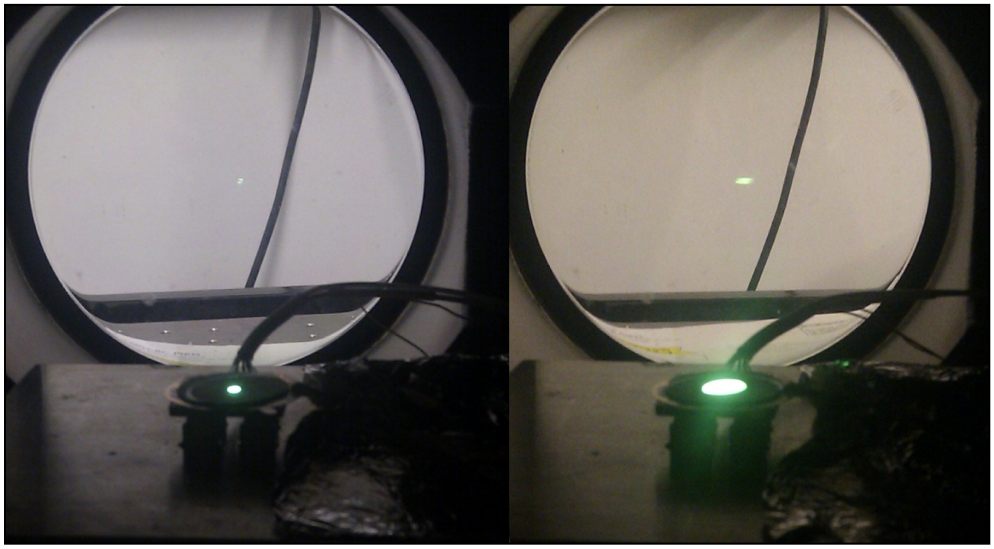

Figure 8.1: A phosphor coated wafer was used to determine the E-gun operating parameters for the size and positioning of the beam.

The sample stage consisted of copper grid electrode on a heater. The sample to be measured was mounted in the centre of the sample stage with silver paste to ensure good electrical contact. A small amount of silver paste was coated around the sides of the sample to prevent any possible charging of the surface. The sample stage was positioned in the chamber and the chamber was pumped down to 10^{-7}

mbar. The sample could then be heated under vacuum to remove adsorbed moisture, which quenches the negative electron affinity of a surface thereby inhibiting secondary electron emission,[8.2] before measurements were taken. Heating of the samples was for approximately 1 hour at 150 °C. The sample was then left to cool to approximately 35 °C before the measurements were taken. The back electrode (copper grid) was connected in series to a voltage source (Keithley 487 picoammeter/voltage source), picoammeter (Keithley 6485 Picoammeter) and then to ground as illustrated in figure 8.2.

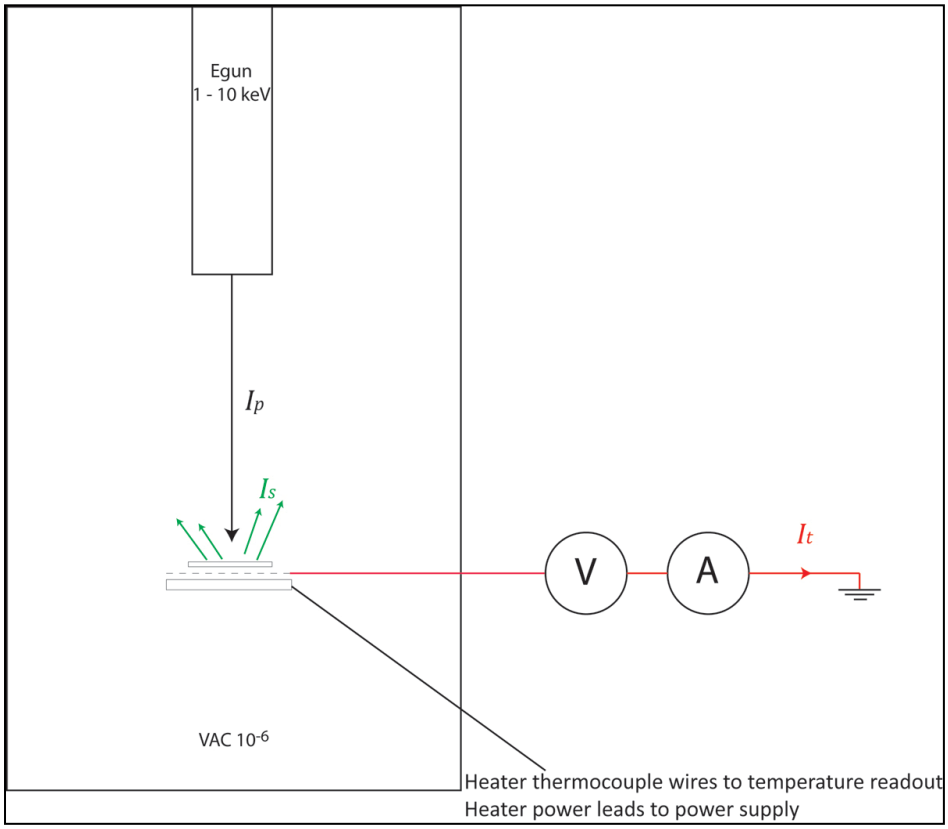

Figure 8.2: Schematic depicting the experimental set-up. The border depicts the chamber (under vacuum conditions), the blue rectangle is the sample, the dashed line is the copper grid which acts as an electrode and below this a heater. Connections are made to the equipment outside the chamber.

Figure 8.3 shows the realisation of this sample arrangement, which is placed in the vacuum system. The E-gun was powered to the desired operating conditions with the attached faraday cup in the closed position to monitor the beam current at the exit of the electron gun. Once the faraday cup was put into then 'open' position

(whereby it is moved out of the beam line, so that the beam impinges on the sample, inducing emission of SEs) the measurements were promptly started.
The current from the sample to ground was measured at bias voltages intervals from -500 V to +500 V. This was done for electron beam energies ranging from 500 eV to 2 keV.

To determine the gain i.e, the secondary electron emission (SEE) yield vs the primary beam current, the sample was biased negatively, then positively, whilst the current to ground was monitored at each interval. To understand the basis for the SEE yield measurements being made, it is important to consider the terms in equation 8.1, where (I_s) denotes the current from the emitted secondary electrons. The target current (I_t) flows to replenish electrons to the positively charged surface in the case where more electrons are emitted from the target sample than the input primary electrons (δ> 1). (I_s) is the current of all electrons leaving the surface, so including both the elastically and inelastically scattered electrons. This is different from some definitions used in literature, where (I_s) often is defined as the current of the 'true' secondaries. In the case of this device, the exact origin of the secondary electrons in unimportant, it is the emitted electron flux that is important. Given that,

$$\begin{aligned} +ve;\quad & I_p = I_t \\ -ve;\quad & I_p - I_s = I_t \end{aligned} \qquad \text{(eq 8.1)}$$

Then;

$$\text{SEE Yield} = \frac{I_s}{I_p} \qquad \text{(eq 8.2)}$$

i.e.,

$$\text{SEE Yield} = \frac{I_{t(-hv)} + I_{t(+hv)}}{I_{t(+hv)}} \qquad \text{(eq 8.3)}$$

$I_{t(-hv)}$: The target current under negative bias (calculated for each negative voltage interval)

$I_{t(+hv)}$: The target current under positive bias (+500 V)

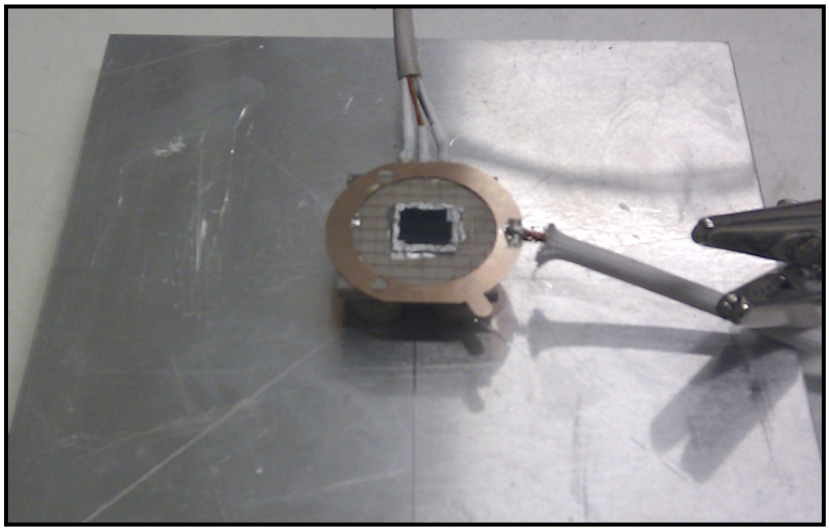

Figure 8.3: Sample stage consisting of a ceramic heater, a back electrode (copper grid) and a typical nanodiamond covered silicon substrate. Silver paste has been used to form a contact between the electrode and sample.

8.3 Aluminium oxide thin film

Other materials are capable of supporting NEA whilst being stable in thin film form, such that their application within the MCP technology can be considered in competition to nanodiamonds. Whilst it is beyond the scope of the current work to carry out an exhaustive study of such materials it is informative to select one such sample so that a comparison with nanodiamonds can be made. The collaborators in the current activity have an in-house program studying aluminium oxide (Al_2O_3) as this material can be conveniently deposited by atomic layer deposition (ALD), a process considered compatible with the (fragile) microchannel plate technology.

The sample used for secondary electron yield measurements consisted of a layer of aluminium oxide, deposited by atomic layer deposition on a silicon wafer, received from the collaborators laboratory.

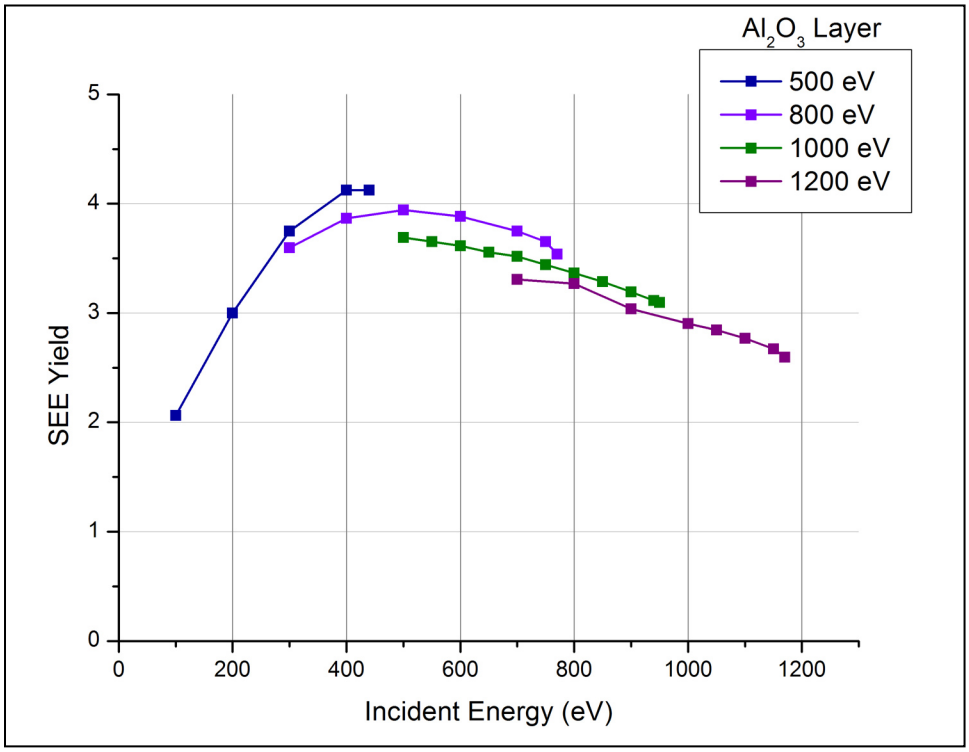

Graph 8.1: Measured SEE yield curves for an ALD deposited layer of Al_2O_3 for electron beam energies, 500 eV, 800 eV, 1000 eV, 1200 eV.

Graph 8.1 shows the obtained SEE yield curves (absolute values) against incident beam energy from 0 eV to 1200 eV. SEE yield curves were obtained for four electron beam energies (500, 800, 1000 and 1200 eV). The curves for each energy were obtained by varying the sample bias at intervals from -50 to -500 V, thereby changing the incident energy at which the electrons impinge on the sample surface as described in the experimental method. The curves do not match exactly as a result of experimental errors introduced by changing conditions in refocusing the beam at subsequent electron beam energies.

Aluminium oxide gives a maximum SEE yield of approximately 4 at 400 eV. This value is consistent with the values obtained by the collaborators for this material. Although this is an improvement upon the existing technology, a SEE yield of 4 means that there is still a significant probability that an interaction event will be lost, as explained in chapter 3.1.4.

8.4 Boron doped microcrystalline diamond (µCD)

Nanodiamonds deposited from solution at room temperature represent the most tangible method of introducing a diamond coating to the fragile three-dimensional structure that is the microchannel plate. However it is known from the Raman spectrum in chapter 5 that the nanodiamonds comprise non-diamond carbon material and a wide range of functional terminating groups (chapter 7). In order to benchmark the performance of nanodiamond layers against a potentially more pure (less sp^2 contaminated) form of nanodiamond, continuous µCD has been studied. To ensure sufficient conduction through the film from the back electrode exists (essential for SEE) boron doped material was selected.

An as received 1" boron doped microcrystalline diamond sample, grown on silicon is characterised using SEM imaging and Raman spectroscopy. The secondary electron emission yield curves were obtained using the method described at the beginning of this chapter.

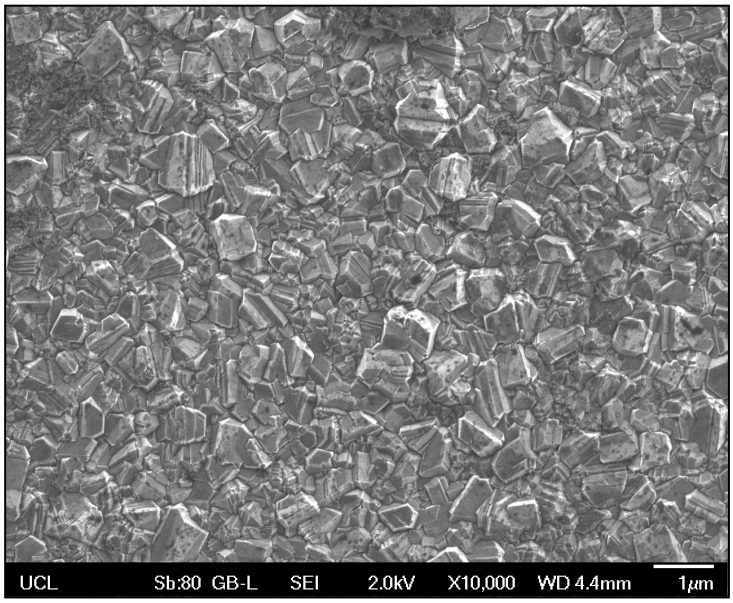

Figure 8.4: SEM image of the boron doped µCD sample showing crystallites with a variety of sizes, the larger crystallites are in the region of 1 µm.

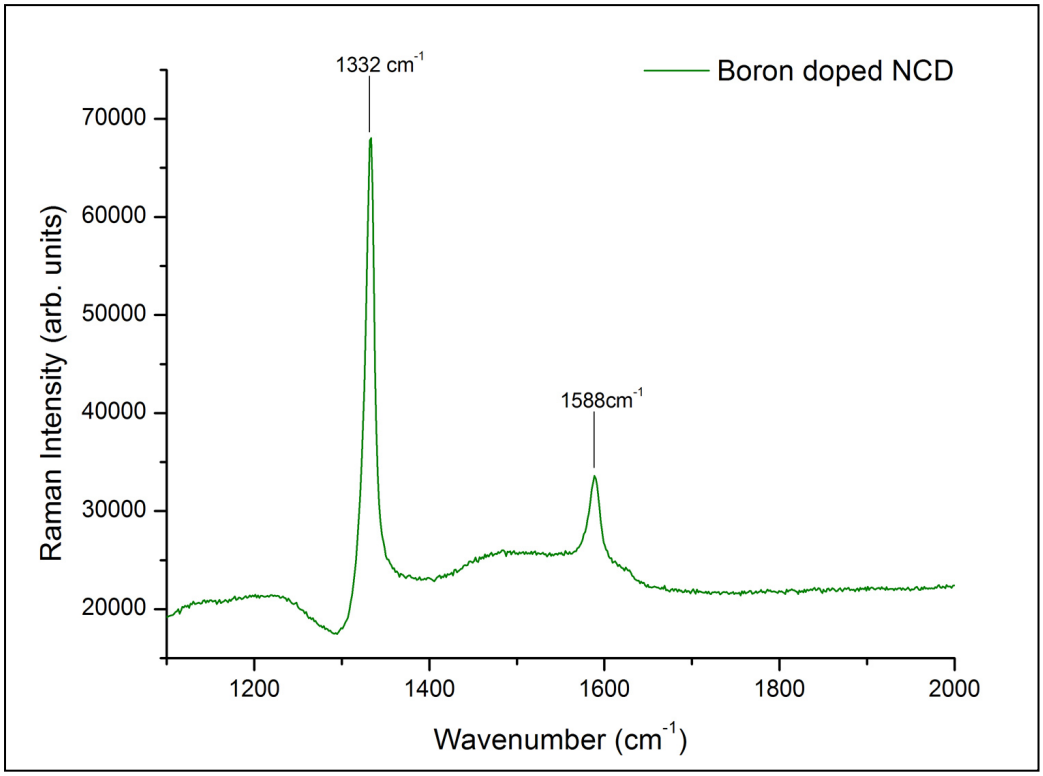

Figure 8.5: Raman spectrum of the boron doped µCD sample, showing peak assignments.

Figure 8.4 shows the SEM image obtained for this sample with grain sizes less than 1 µm. The thickness of this sample is approximately 1 µm. The Raman spectrum of this sample (Figure 8.5) shows a sharp diamond peak at 1332 cm^{-1}. The asymmetry of the peak (a Fano line shape) is observed; this is attributed to the Fano-type interference between the discrete zone-centre phonon and the continuum of electron states induced by the presence of the dopant (boron). Pruvost and Deneuville (2001)[8.1] show that the Fano appears above a critical percolation threshold which corresponds to the onset of metallic conductivity (i.e. ca. 2 x 10^{20} B cm^{-3}). The defined peak at approximately 1580 cm^{-1} is the 'G' (graphitic) peak of amorphous carbon.

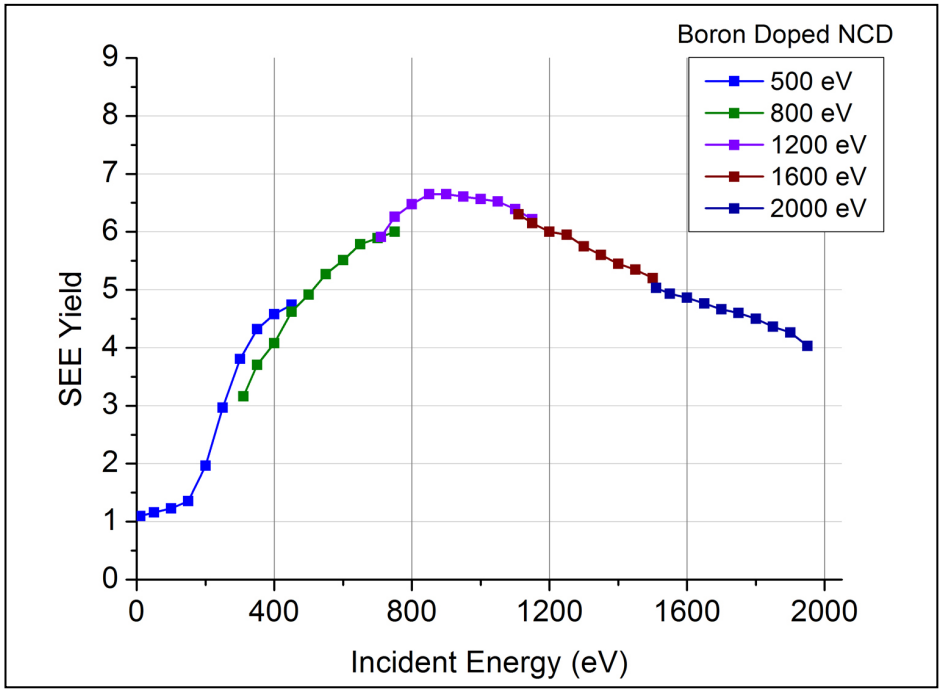

Graph 8.2: Measured SEE yield curves for boron doped microcrystalline diamond for electron beam energies, 500 eV, 800 eV, 1000 eV, 1200 eV, 1600 eV and 2000 eV.

Graph 8.2 shows the obtained SEE yield curves (absolute values) against incident beam energy from 0 eV to 2000 eV. SEE yield curves were obtained for five electron beam energies (500, 800, 1200, 1600 and 2000 eV). The curves for each energy were obtained by varying the sample bias at intervals from -50 to -500 V, thereby changing the incident energy at which the electrons impinge on the sample surface. The curves do not match exactly as a result of experimental errors introduced by changing conditions in refocusing the beam at subsequent electron beam energies. Desorption of hydrogen from the surface at the point where the electron beam is impinging may also be a contributing factor.[8.2]

The SEE yield increases with increasing incident energy, as more secondary electrons can be excited, to a maximum of **6.7** ± 0.3 **at 850 eV**. It then begins to decrease at a slower rate as the penetration of the primary electrons becomes higher than the escape depth of the secondary electrons.

Shih *et al.*[8.2] report a value of 10.3 ± 0.5 for the maximum SEE yield at 1160 ± 160 eV from a boron doped diamond film of thickness between 100 – 200 microns.

The value obtained from this boron doped μCD film is promising; if a similar value can be obtained from a nanodiamond layer, both the current technology and other research materials would be outperformed. However, the film surface is hydrogen terminated which is not considered to be stable.[8.2] Although a metallic layer such as caesium could be used as an alternative NEA surface for the diamond film, in the first instance it is worth investigating the stability of the hydrogen surface, with a view to the relative importance of H-termination instability in the night-vision applications.

8.4.1 Stability of the hydrogen surface

As discussed in chapter 3, the negative electron affinity of diamond surfaces is highly dependent on the surface termination. Hydrogenated surfaces are the easiest to produce as any CVD grown diamond material, containing atomic hydrogen in the growth gas mixture, will naturally be terminated with hydrogen. This surface is not generally considered to be stable and most experimental work is conducted using a pulsed electron beam to avoid beam induced surface modification during measurements.[8.3]

In order to investigate the stability of the hydrogen surface in the environment being studied here, we can calculate the desorption cross section. In applications, the lifetime of the device is a crucial aspect and it is of interest to find the electro-positive element with the smallest cross-section for electron stimulated desorption. To calculate the cross section, the experiment was set up in the same way as for SEE yield calculations as described at the beginning of this chapter, but with fixed conditions for the beam energy and beam current. The beam current used was 0.5 μA. The sample current was then monitored over a period of time until substantial decay had occurred. The logarithm of the current decay in the presence of a continuous bombardment with an electron beam against time in minutes is shown in graph 8.3.

The total cross-section σ_{tot}, for stimulated hydrogen desorption can be obtained from the time constant of the exponential decay of the current during constant electron bombardment of a hydrogenated diamond surface without assuming there is no readsorption. The current shows an exponential time dependence;

$$I_D(t) = I_0 \times \exp\left(\frac{-t}{t}\right) \qquad \text{(eq. 8.4)}$$

Fitting $I_D(t)$ to the data of graph 8.3, the total desorption cross section σ_{tot}, including all processes that lead to a hydrogen loss, is obtained from the time constant τ via;

$$\sigma_{tot} = \frac{eA}{I_e \tau} \qquad \text{(eq. 8.5)}$$

where *e* is the electronic charge. For this experiment a defocused electron beam was used. The beam diameter of the electron gun was measured on a phosphorus screen within the vacuum chamber to be 16 ± 1 mm, resulting in an area A = (201 ± 25) mm^2. The electron current (I_e) is determined by means of a Faraday cup with an accuracy of around 10%.*

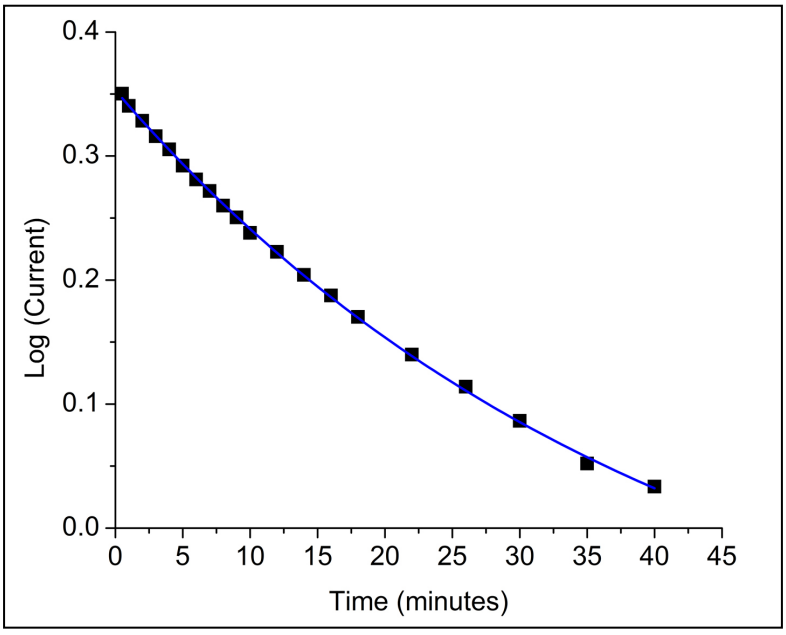

Graph 8.3: Plot of the sample current (measured to ground) against time during continuous bombardment with a 1000 eV electron beam (sample bias -50V).

* This error was obtained experimentally by comparing the current values obtained by the Faraday cup to the beam current measured through the sample when a positive bias is applied.

The resulting cross section is σ_{tot} = 1.3 x 10^{-20}. This value is two orders of magnitude less than quoted in the literature for boron doped polycrystalline diamond.[8.4] Goeden and Dollinger (2002)[8.5] suggest nitrogen defects in the film decrease the desorption cross section. Therefore the significant difference in cross sections could be explained by the possibility of the defect structure of the NCD film suppressing hydrogen desorption. Another contributing factor may be replenishment of surface hydrogen from the bulk through thermal migration through the grain boundaries. Relating this cross section to a device application, involving a 400 mm^2 area and an operating current of 1nA, it would take 667 hours of usage to reduce the secondary electron yield by half. Current image intensifiers have a typical lifetime of 10,000 hours.

8.5 Gas treatments of nanodiamond layers

The promising results from hydrogen terminated boron-doped nanocrystalline diamond prompted investigations into the secondary electron emission of nanodiamond coatings. In chapter 7, it was established that untreated nanodiamonds have a variety of surface functional groups. In order for secondary electron emission, we require an electro-positive surface. The simplest way to achieve this is to hydrogenate the nanodiamond surface.

8.5.1 Hydrogen treatment of nanodiamond coatings

The substrate material, a conductive silicon wafer (arsenic doped, n-type, 0.01 Ωcm) was cut into samples measuring approximately 1 cm^2. The samples were cleaned using the de-greasing protocol described in chapter 4.7. The samples were then coated with nanodiamonds using the methods described in chapter 5; the details are given in the results section. Two types of hydrogen treatment were investigated. First, an annealing procedure was used, involving an atmosphere of hydrogen (the method used in chapter 7). Secondly, a hydrogen microwave plasma treatment in a CVD reactor. The latter treatment is routinely used to hydrogenate diamond films.[8.6] The samples were measured for their secondary electron emission yield using the experimental method described at the beginning of this chapter.

8.5.2 Results and Discussion

Graph 8.4 shows the obtained SEE yield curves (absolute values) against incident beam energy from 50 eV to 960 eV for an untreated nanodiamond coating supported on a conductive silicon wafer. SEE yield curves were obtained for three electron beam energies (500, 800 and 1000 eV). The curves for each electron beam energy were obtained by varying the sample bias at intervals from -50 to -500 V, thereby changing the incident energy at which the electrons impinge on the sample surface. The curves do not match exactly as a result of experimental errors introduced by changing conditions in refocusing the beam at each electron beam energy. Desorption of hydrogen from the surface at the point where the electron beam is impinging is also a contributing factor.

Sample 1 (Control)
Conductive silicon sample with nanodiamond coating using colloid concentration of 5 g/L.
Treatment No treatment. Heating under vacuum prior to measurements at 150 °C for 1 hour to remove adsorbed moisture.

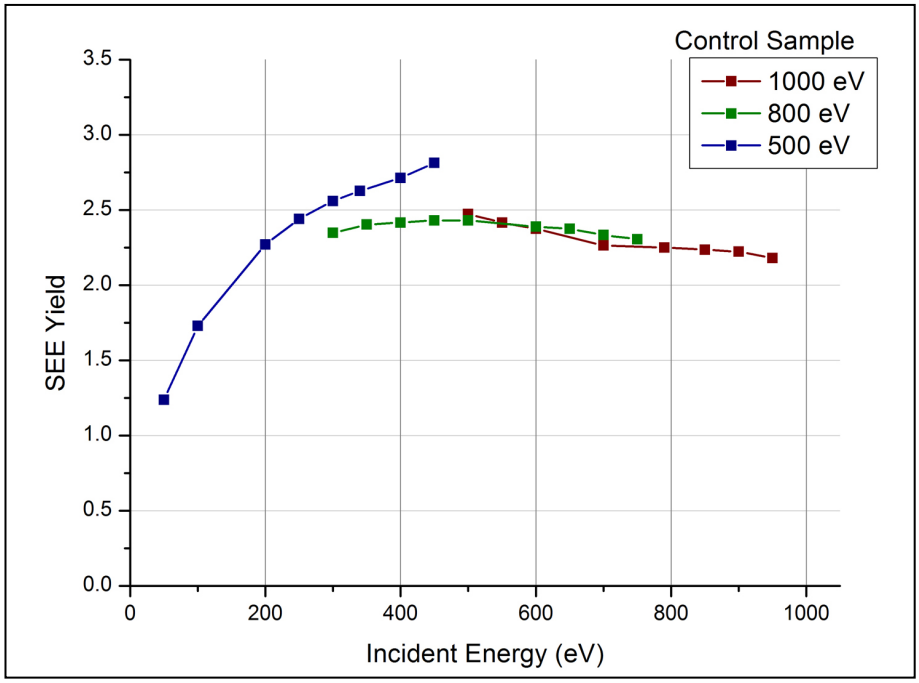

Graph 8.4: SEE yield curves for sample 1 for electron beam energies, 500eV, 800eV and 1000eV.

The SEE yield increases with increasing incident energy, as more secondary electrons can be exited, to a maximum of 2.5 – 2.7 at 450 eV. This energy is 400 eV less than required for the maximum SEY for the boron doped nanocrystalline diamond measured in the previous section. This is expected as this nanodiamond layer is in the order of a few tens of nanometres. A surface with positive electron affinity can also experience emission of electrons as it is a probabilistic process, so the SEE yield of such a surface can still be greater than one. The SEE yield from the nanodiamond layer (**2.5 – 2.7**) is suggestive of a low barrier or negative electron affinity (NEA). It is also possible that some areas of NEA exist as a result in the variation of surface functional groups. This value is lower than that obtained for aluminium oxide (**4 at 400 eV**) but it is promising and with surface homogenisation, may improve.

The next sample (sample 2) consists of 50% surface coverage of nanodiamond particles on a conductive silicon wafer. This sample was then treated in a hydrogen gas, microwave plasma for 5 minutes. The full conditions are described in figure 8.5.

Sample 2
Nanodiamond coating using colloid concentration of 0.5 g/L.
Treatment H_2 MW Plasma at 500 °C, 5mins, 20 torr, 500 W. Heating under vacuum prior to measurements at 150 °C for 1 hour to remove adsorbed moisture.

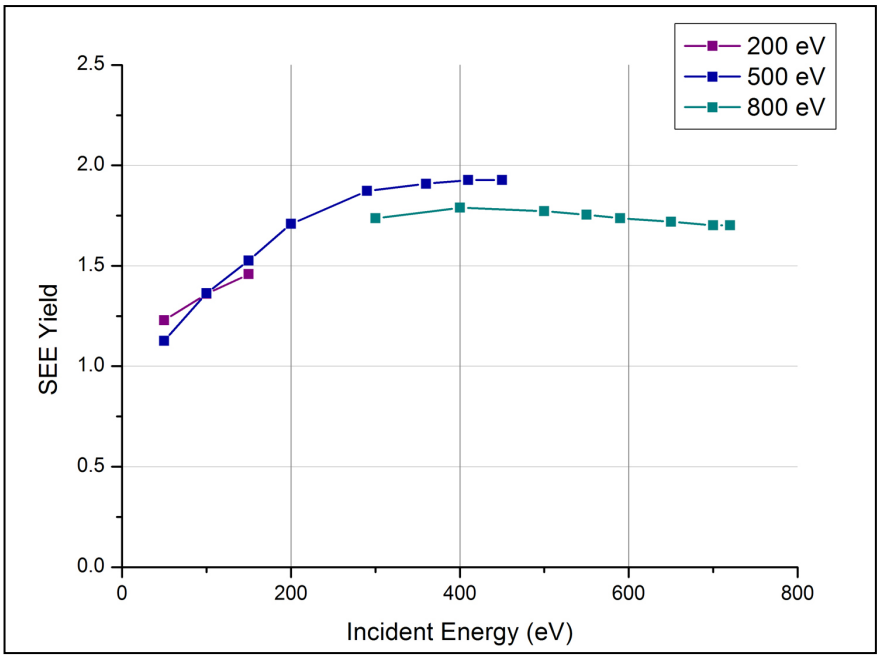

Graph 8.5: SEE yield curves for sample 2 for electron beam energies, 200eV, 500eV and 800eV.

Graph 8.5 follows the same format as the previous graph. The electron beam energies used to investigate this sample were 200 eV, 500 eV and 800 eV. The reduction in surface coverage prompted starting the measurements with a lower electron beam energy. The SEE yield curves show the same increase of SEE yield with increasing incident energy up to the maximum of **1.9** at **450 eV**. This lower maximum SEE yield compared to sample 1 (SEE yield of 2.8) suggests that a continuous film is important for good secondary electron emission characteristics, as might be expected.

Therefore, sample 3 was chosen to have full nanodiamond surface coverage with an approximate layer thickness of 30nm; the experiment conditions used for this treatment and the measured SEE yield curves are shown in figure 8.6.

Sample 3
Nanodiamond coating using colloid concentration of 5 g/L
Treatment H_2 MW Plasma at 800 °C, 750W; 35-40 torr for 1 hour. Heating under vacuum prior to measurements at 150 °C for 1 hour to remove adsorbed moisture.

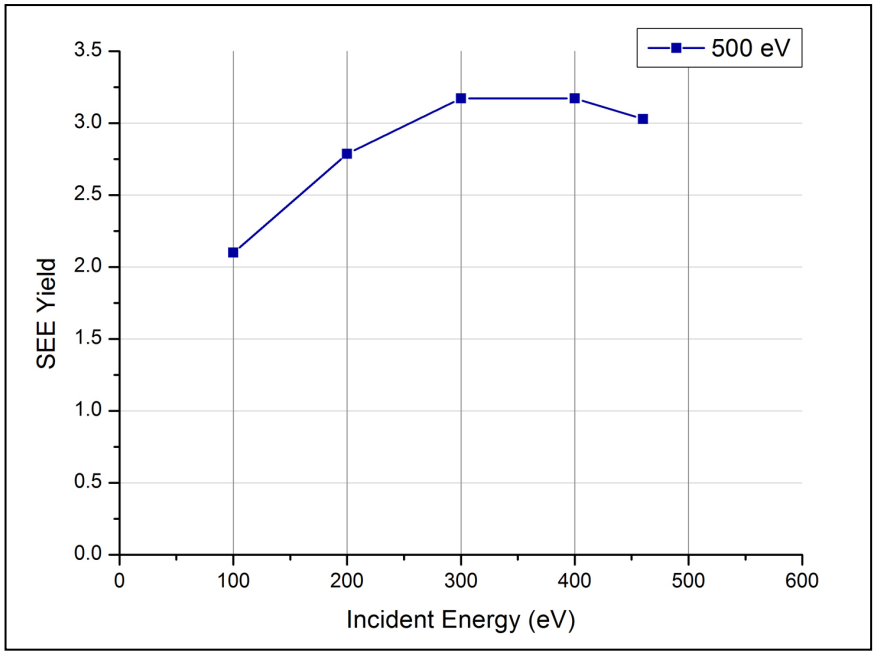

Graph 8.6: SEE yield curves for sample 3 for electron beam energy 500 eV.

Graph 8.6 follows the same format as the previous graph. The electron beam energy used to investigate this sample was 500eV. From the previous two samples, the maximum SEE yield was expected to be at around 400eV, so further SEE yield curves were not obtained. This SEE yield curve shows the same increase of SEE yield with increasing incident energy up to the maximum of **3.2** at **350 eV**. This is a slight improvement on the secondary electron yield of an untreated sample suggesting that the surface is becoming more electro-positive by hydrogenation of the surface.

Sample 4
Nanodiamond coating using colloid concentration of 5 g/L
Treatment H_2 MW Plasma at 800 °C, 750W; 25 torr for 10 hours. Heating under vacuum prior to measurements at 150°C for 1 hour to remove adsorbed moisture.

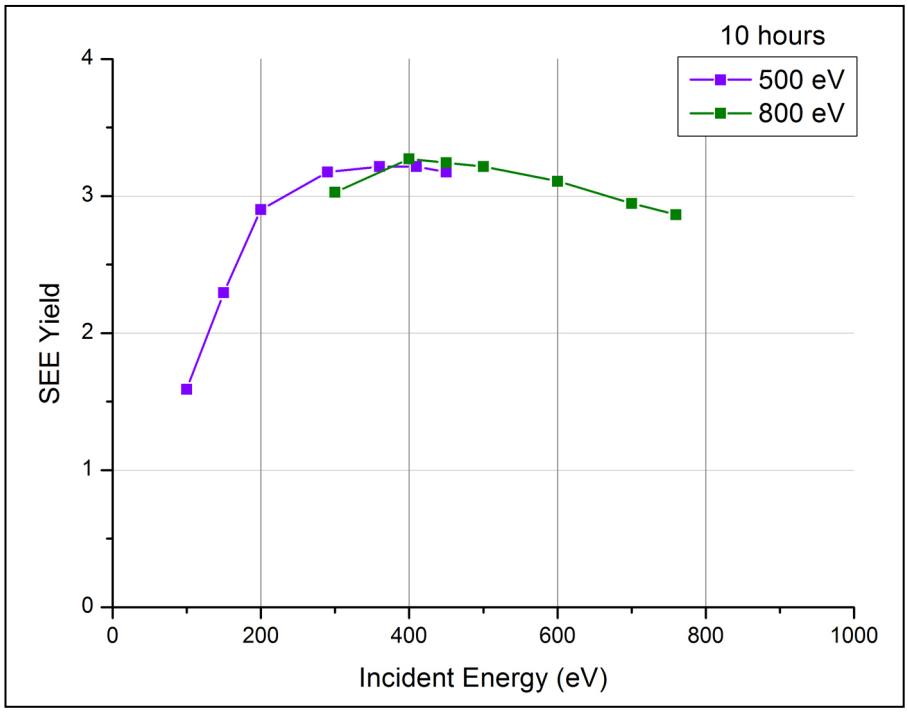

Graph 8.7: SEE yield curves for sample 1 for electron beam energies, 500eV and 800eV.

The results from sample 4 are plotted in graph 8.7. This sample has the same nanodiamond coating and hydrogen gas microwave plasma treatment as sample 3, except that the treatment duration was extended from 1 hour to 10 hours. The graph follows the same format as the previous graphs for this sample set. From this, we can see that the maximum SEE yield is approximately **3.2 at 400 eV**. There is no improvement over sample 3.

These results show that there is little improvement of the SEE yield over an untreated sample with hydrogen gas plasma treatment. In chapter 7, a hydrogen gas anneal was investigated for its suitability to hydrogenate the nanodiamond surface. The FTIR spectrum obtained indicated that this treatment is just as successful as the microwave plasma treatment reported by Arnault *et. al.*[8.6]

Sample 5
Nanodiamond coating using colloid concentration of 5 g/L
Treatment H_2 gas anneal at 300 °C

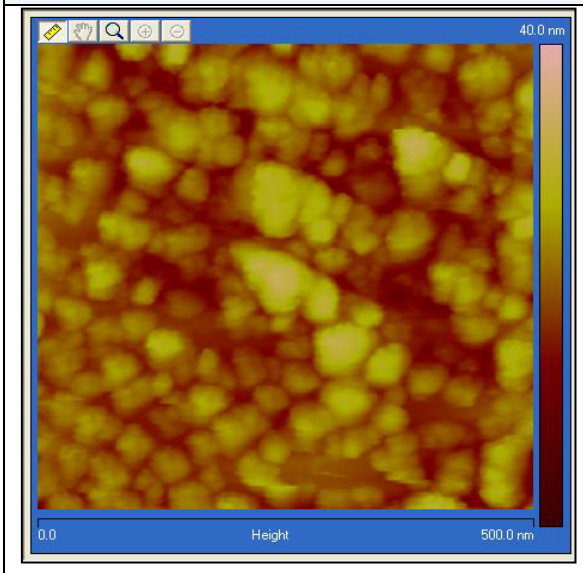

Figure 8.6: AFM image of sample 5 before treatment showing a 500 µm x 500 µm area. The ND particles are tightly packed and agglomerated in some areas.

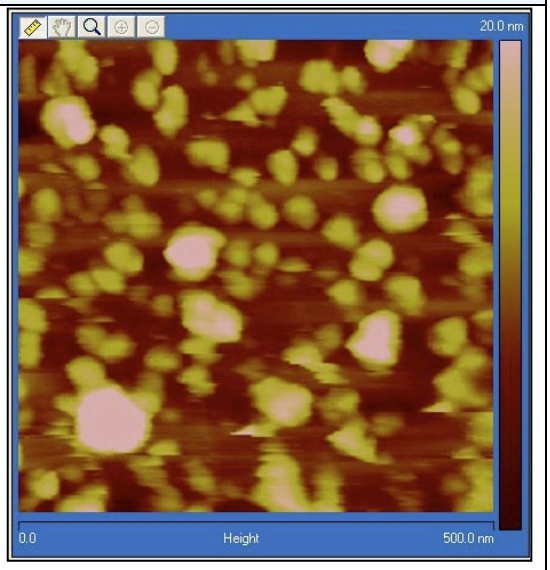

Figure 8.7: AFM image of sample 5 after hydrogen treatment showing a 500 µm x 500 µm area. The dark areas is the surface of the flat silicon substrate.

Figures 8.6 and 8.7 show AFM images of sample 5 before and after a hydrogen gas treatment at 350 °C. This is a lower temperature than the 500 °C used for the FTIR sample in Chapter 7. However, figure 8.7 displays regions where the silicon surface is visible (dark areas) indicating that particles have been removed from the surface by this treatment. The FTIR investigation was carried out with a thick and visible to the naked-eye layer of NDs, as sufficient particles to obtain a FTIR signal were required. Therefore, this phenomenon was not previously observed. In the case of sample 5, the layer thickness before treatment was approximately 30 – 40 nm.

The secondary electron emission measurements for this sample produced a maximum SEE yield of **1.9 at 400 eV**. This value is the same as the maximum SEE yield obtained for sample 2 (H_2 MW plasma treatment of 50% sample coverage). Therefore, whilst the nanodiamond surfaces may have undergone hydrogen termination using this treatment, it has also removed many particles from the substrate, presumably through chemical etching by the hydrogen gas.

8.5.3 Caesium metallisation of nanodiamond coatings

The previous section has shown that while hydrogen microwave plasma treatment of nanodiamond layers gives a slight improvement to the secondary electron yield, the value is still much smaller than for boron doped nanocrystalline diamond (which was around 6 at 400 eV) and slightly smaller than for Al_2O_3 (4 at 400 eV).
Besides hydrogen, many electropositive materials produce NEA of diamond. It is well known that a monolayer of caesium deposited on the diamond surface produces a larger NEA, thereby giving a greater improvement to the secondary electron yield.[8.9] Caesium can be deposited directly onto the diamond surface to create a NEA surface; however, it has been shown that depositing caesium on an oxidised surface creates a more stable and more electro-positive surface.[8.7, 8.8] Therefore, prior to caesium deposition, the nanodiamond layers must be oxidised. In chapter 7, it was concluded that for the most thorough oxidation leading to the required surface functional groups (ketones) the surface must be hydrogen terminated using a hydrogen gas anneal at 500 °C. However, the results in the previous section have shown that this treatment etches the particles.
An alternative treatment for oxidation investigated in chapter 7 is reactive ion etching (RIE) using a pure oxygen gas plasma. This treatment was partially successful in reducing the surface to oxygen containing groups as shown by the FTIR (Figure 7.4 (b)).

Nanodiamond coated, silicon samples were prepared using the standard process described in chapter 5. They were then treated in an Oxford Plasma Labs RIE using pure molecular oxygen as the plasma gas. This treatment process is described in detail in chapter 7. The samples were then sent to our collaborators for deposition of an atomic layer of caesium using thermal evaporation. This was performed in a custom built chamber under vacuum ($1x10^{-8}$ torr) using caesium getters from SAES Ltd. Secondary electron emission yield measurements were conducted using the same method as for the previous samples. SEE yield curves were obtained using electron beam energies of 500 and 800 eV.

8.5.4 Results and Discussion

	Description	Treatment	Maximum SEE Yield
Sample 6 (control)	Nanodiamond coating using colloid concentration of **5 g/L (30nm thick layer)**	Deposition of an atom layer of Caesium, no prior treatment.	**3.7 at 500eV**
Sample 7	Nanodiamond coating using colloid concentration **of 0.5 g/L (10nm thick layer)**	RIE oxygen plasma duration: 7mins. Deposition of an atom layer of Caesium.	**4.5 at 400eV**
Sample 8	Nanodiamond coating using colloid concentration of **5 g/L (30nm thick layer)**	RIE oxygen plasma duration: 7mins. Deposition of an atom layer of Caesium.	**4.5 at 400eV**
Sample 9	Nanodiamond coating using colloid concentration of **5 g/L (30nm thick layer)**	RIE oxygen plasma duration: 15mins. Deposition of an atom layer of Caesium.	**4.5 at 400eV**

Table 8.1: Description of the nanodiamond coatings and treatments for samples 6 – 9 and the SEE yields obtained for each.

Table 8.1 displays information on the nanodiamond coating of each sample, the treatment received by the sample and the maximum SEE yield value obtained from the sample. Sample 6 displays some improvement to SEE yield with caesium deposition over the untreated control sample (1). Samples 7, 8 and 9 all show an improvement of the SEE yield to 4.5, regardless of the initial nanodiamond layer thickness or RIE duration. Although these values are equivalent to the other current research material (Al_2O_3), they are much lower than expected, by reference to the scientific literature. In the case of case of boron doped polycrystalline diamond samples, an increase in the SEE yield amounting to double the value for hydrogen termination has been reported.[8.9] This suggests that the oxidation process being performed is insufficient for completely CsO formation. However, that seems unlikely given the analysis presented in chapter 7. More likely it is a limitation to the SEE Yield created by the poor 'quality' of the nanodiamond layer when compared to the large grain continuous thin film layer being used in the works reported as reference 8.11. This leads to the conclusion that treatments to further modify and/or improve the nanodiamond surface are required before Cs treatments will give rise to optimal SEE yields.

8.6 CVD processing of nanodiamond layers

The previous section has shown that gaseous treatments are only partially successful in improving the secondary electron yield from a DND layer. This section investigates the suitability of using chemical vapour deposition (CVD) with processes similar those of growing nanocrystalline diamond but with much lower temperature regimes, which may be compatible with the micro channel plates. Four samples, with distinct differences in the process parameters, in regards, to power, pressure, treatment time, treatment temperature and methane concentration were investigated for their secondary electron yield. Raman spectroscopy was used to analyse the diamond/sp^2 content of the layers and SEM to investigate the morphology.

8.6.1 Sample preparation

The samples measured in this section were prepared with our collaborators in at the Fraunhofer Institute for Applied Solid State Research in Freiburg, Germany. Silicon wafers with 500 μm thicknesses were used as substrates for all four samples. All samples were cleaned by heating in NH3OH:H2O2:DI H2O (1:1:5) at 75 °C for 10 minutes followed by rinsing in de-ionsied water in an ultrasonic bath. The substrates were seeded with a monolayer nanodiamond particles using the process described in chapter 5, to ensure an evenly spaced out, tight size distribution of particles.

Chemical vapour deposition (CVD) was performed using an ellipsoidal microwave cavity reactor cavity reactor designed to produce uniform plasma discharges over large areas and under a wide range of conditions.[8.10] Deposition from a hydrogen-rich plasma environment ensured complete hydrogen coverage of the sample surface. The treatment conditions for each of the four samples are listed in the results section. The treatment conditions for each sample are followed by the SEM images and Raman spectra obtained. Finally, the secondary electron yield curves, obtained using the method described at the beginning of this chapter are displayed.

8.6.2 Results

Sample ERVII618

Substrate: 1" Silicon

H_2 298.5 sccm ; CH_4 0.5 sccm (0.16% CH_4)

Power: 3000W

Process Pressure: 60 mbar

Temp: 800 °C

Treatment time: 205 minutes

Thickness: 280 nm

Figure 8.8: Sample ERVII618

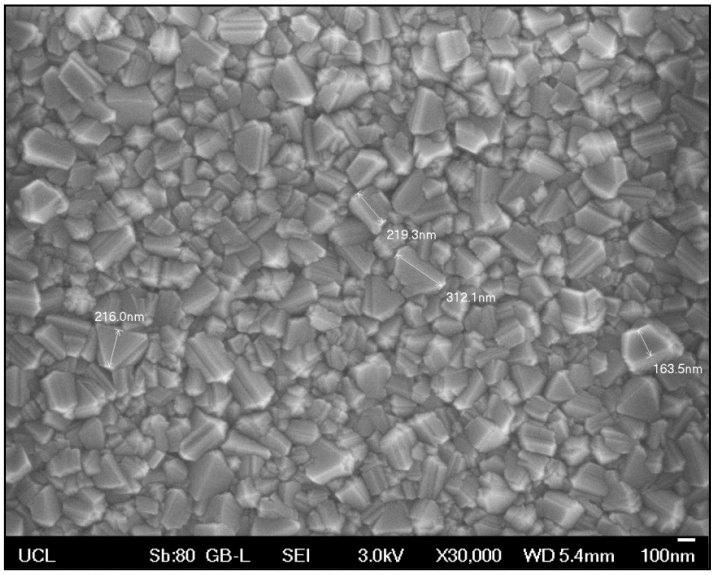

Figure 8.9: SEM image of sample ERVII618 showing crystallites with a variety of sizes, the larger crystallites are in the region of 150 – 250 nm.

The treatment conditions for sample ERVII618 are listed above. Figure 8.8 shows a photograph of this sample; the homogenous colour indicating even growth over the surface. Figure 8.9 displays the SEM image obtained, showing crystallites of a variety of sizes that are in the region of 150 – 200 nm. The obtained Raman spectrum for this sample in shown in Figure 8.10. The spectrum shows a sharp diamond peak at 1332 cm^{-1} and the presence of a number of other peaks; the spectrum is discussed further at the end of this results section.

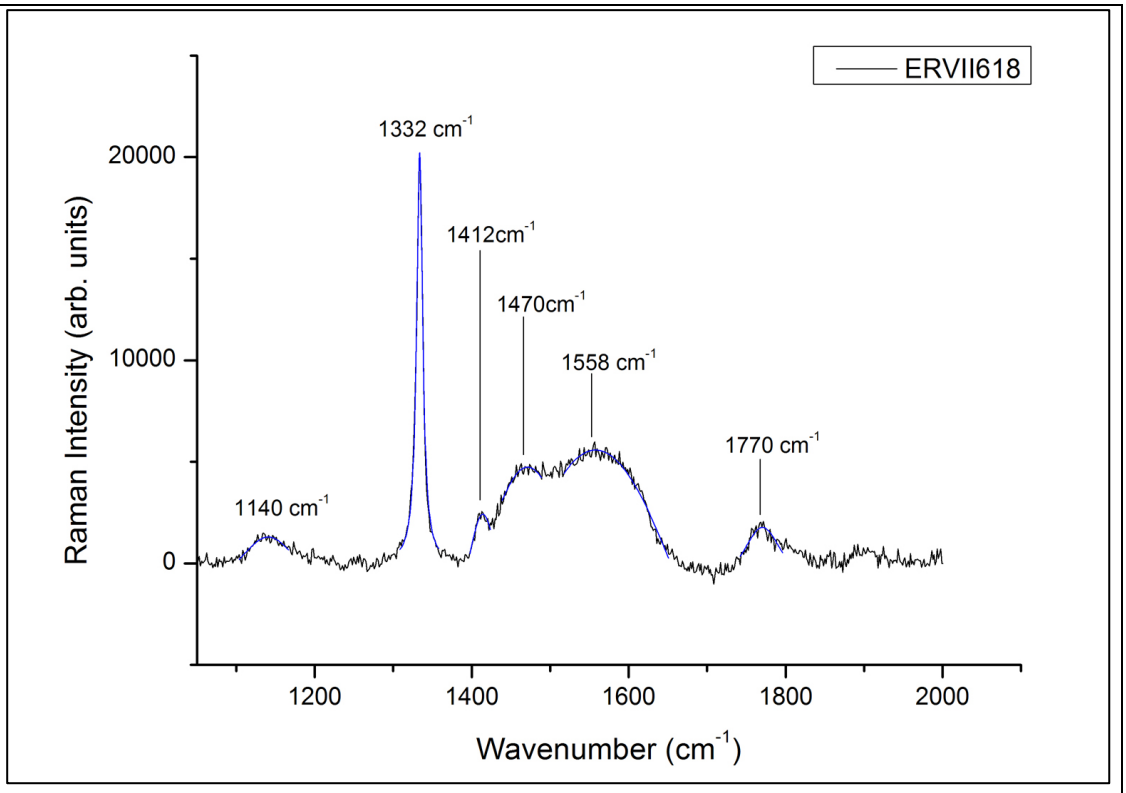

Figure 8.10: Raman spectrum of sample ERVII618 with assigned peaks using Lorentizian peak fitting.

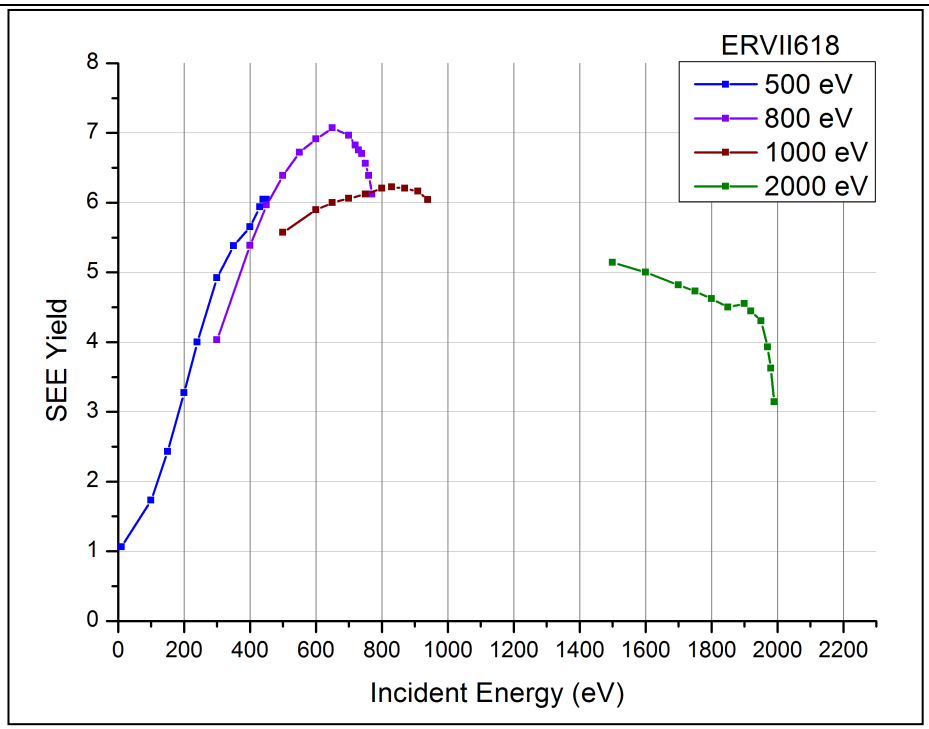

Graph 8.8: SEE yield curves for sample ERVII618, for electron beam energies, 500 eV, 800 eV and 1000 eV. and 2000 eV. The maximum SEE yield of 7 occurs at 620 eV.

Graph 8.8 shows the obtained SEE yield curves (absolute values) against incident beam energy from 0 eV to 2000 eV. SEE yield curves were obtained for four electron beam energies (500, 800, 1000 and 2000 eV). The curves for each energy were obtained by varying the sample bias at intervals from -50 to -500 V, thereby changing the incident energy at which the electrons impinge on the sample surface. The curves do not match exactly as a result of experimental errors introduced by changing conditions in refocusing the beam at subsequent electron beam energies. Desorption of hydrogen from the surface at the point where the electron beam is impinging may also be a contributing factor.[8.2] The SEE yield increases with increasing incident energy, as more secondary electrons can be excited, to a maximum of **7 at 620 eV**. It then begins to decrease at a slower rate as the penetration of the primary electrons becomes higher than the escape depth of the secondary electrons.

The treatment conditions for sample ERVII649 are listed in the results table on the following page. Figure 8.11 shows a photograph of this sample; the colour pattern indicating uneven growth thickness over the sample area. Figure 8.12 displays the SEM image obtained, showing crystallites of a variety of sizes that are in the region of 100 – 280 nm. The obtained Raman spectrum for this sample in shown in Figure 8.13. The spectrum shows a sharp diamond peak at 1332 cm^{-1} and the presence of a number of other peaks; the spectrum is discussed further at the end of this results section. Graph 8.9 shows the obtained SEE yield curves (absolute values) against incident beam energy from 300 eV to 1000 eV. SEE yield curves were obtained for two electron beam energies (500 and 1000 eV). The curves for each energy were obtained by varying the sample bias at intervals from -50 to -500 V, thereby changing the incident energy at which the electrons impinge on the sample surface. This incident energy range was studied as the maximum SEE yield was expected to lie within this. The curves do not match exactly for the reasons explained previously. The SEE yield increases with increasing incident energy, as more secondary electrons can be excited, to a maximum of **8.5 at 780 eV**. It then begins to decrease at a slower rate as the penetration of the primary electrons becomes higher than the escape depth of the secondary electrons.

Sample ERVII649

Substrate: 2" Si 500µm

H_2 298.5 sccm ; CH_4 1.5 sccm (0.5% methane, 5% for the first hour)

Power: 1500 W

Process Pressure: 10 mbar

Treatment Time: 16 hours

Temperature: 440°C

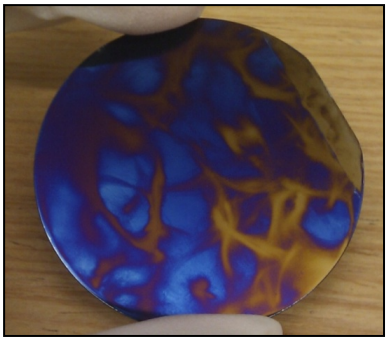

Figure 8.11: Sample ERVII649

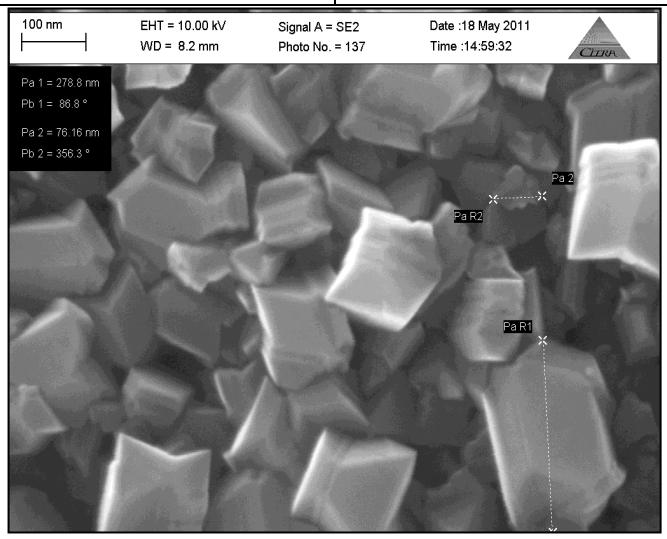

Figure 8.12: SEM of sample ERVII649 showing crystallites with a variety of sizes. The large crystallite has a length of ~280 nm.

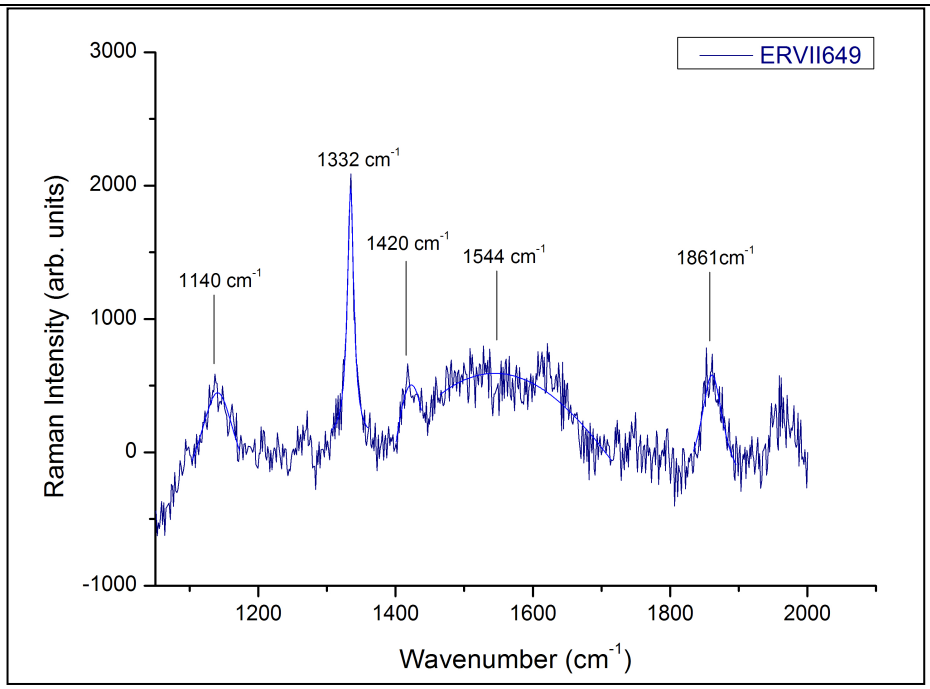

Figure 8.13: Raman spectrum of sample ERVII649 with assigned peaks.

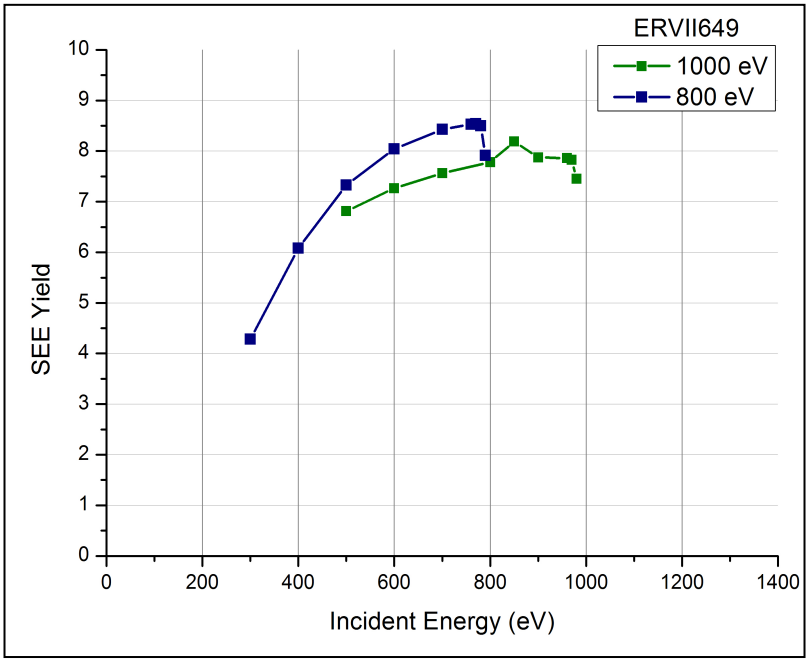

Graph 8.9: SEE yield curves for as-received sample ERVII649 for electron beam energies, 800 eV and 1000 eV. The maximum SEE yield of 8.5 occurs at 780 eV.

The treatment conditions for sample ERVII665 are listed on the next page. Figure 8.14 displays the SEM image obtained, showing crystallites of a variety of sizes that are in the region of 100 nm or smaller. It is interesting to note that although while the power, pressure and treatment time were the same as for ERVII649, the film thickness and grain size is smaller for ERVII665. This suggests that the small difference in methane concentration (0.5% to 0.33%) and substrate temperature affect growth of the film quite significantly. Typically, we would expect the film grown with a higher methane percentage to present with smaller grain sizes as a result of greater re-nucleation.[8.15] In this case, the opposite is observed which can be attributed to the slower rate of reaction because of the lower temperature of ERVII649.

The obtained Raman spectrum for this sample in shown in Figure 8.15. The spectrum shows a sharp diamond peak at 1332 cm^{-1} and the presence of a number of other peaks; the spectrum is discussed further at the end of this results section.

Sample ERVII665

Substrate: 3” Si 500µm

H_2 299 sccm ; CH_4 1.0 sccm (0.33% methane; 5% for the first hour)

Power: 1500 W

Process Pressure: 10 mbar

Temperature: 550°C

Treatment Time: 16 hours

Thickness: 140 nm

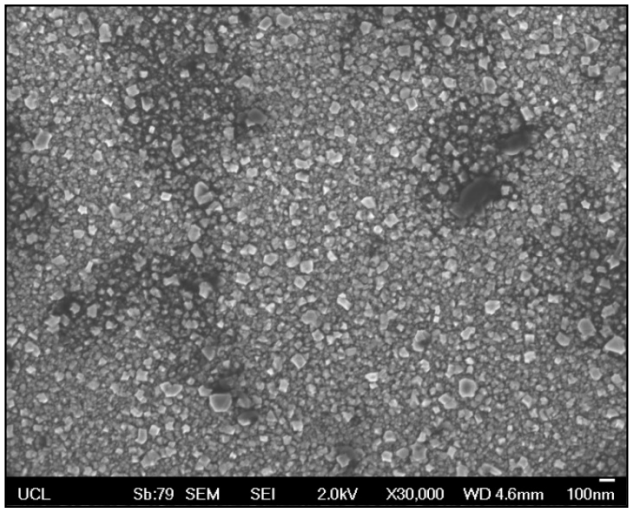

Figure 8.14: SEM image of sample ERVII5665.

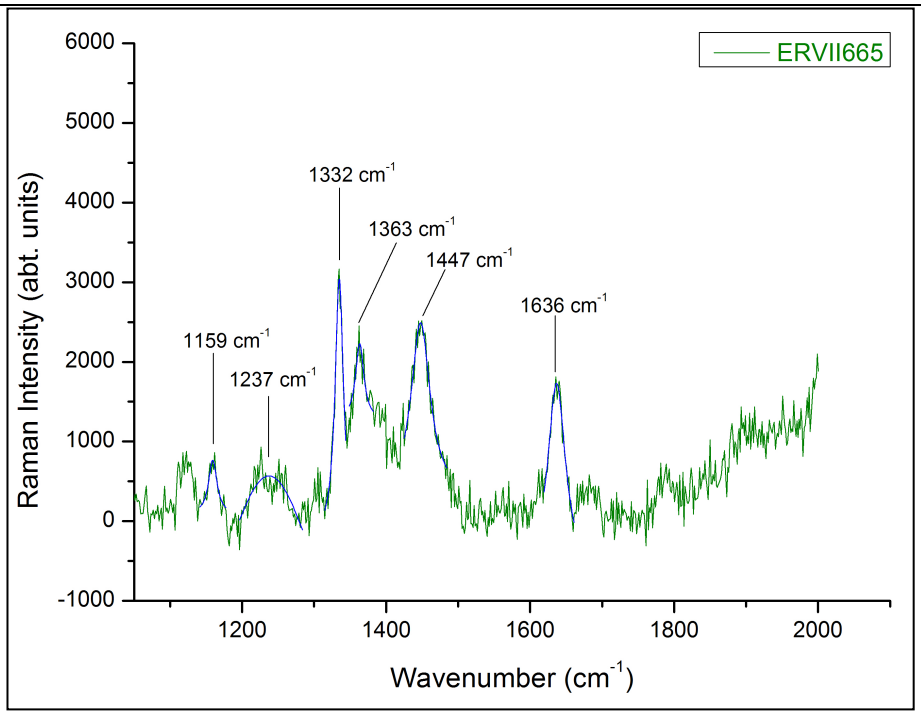

Figure 8.15: Raman spectrum of sample ERVII665 with assigned peaks.

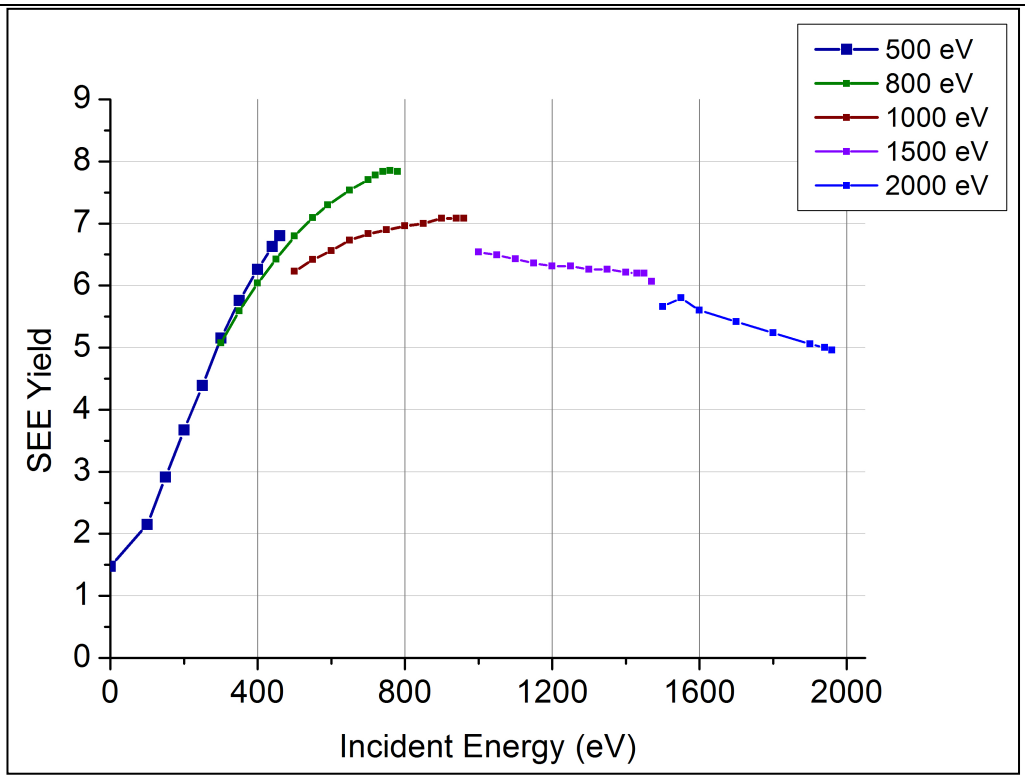

Graph 8.10: SEE yield curves for sample ERVII665 for electron beam energies, 500 eV, 800 eV and 1000 eV. 1500 eV and 2000 eV. The maximum SEE yield of 7.9 occurs at 780 eV.

Graph 8.10 shows the obtained SEE yield curves (absolute values) against incident beam energy from 0 eV to 2000 eV. SEE yield curves were obtained for five electron beam energies (500, 800, 1000, 1500 and 2000 eV). The curves for each energy were obtained by varying the sample bias at intervals from -50 to -500 V, thereby changing the incident energy at which the electrons impinge on the sample surface. The curves do not match exactly for the reasons explained previously. The SEE yield increases with increasing incident energy, as more secondary electrons can be excited, to a maximum of **7.9 at 780 eV**. Which is a similar value to that obtained from ERVII649; in good agreement with the similarity between the two films. It then begins to decrease at a slower rate as the penetration of the primary electrons becomes higher than the escape depth of the secondary electrons.

The results for the last sample ERVII652 are given in figure 8.16 and graph 8.11. This sample had a high power density treatment, at a higher temperature, similar to sample ERVII618, however for a short duration of 5 mins. The aim for this sample was to investigate whether a short, high power density treatment would enhance the nanodiamond coating sufficiently to improve the SEE characteristics. Post treatment, this sample looked the same as pre-treatment, with some cloudy patches.

Sample ERVII652

Substrate: 2" Si 500µm

H_2 299 sccm ; CH_4 1 sccm

Power: 3000 W

Process Pressure: 60 mbar

Temperature: 750°C

Treatment Time: 5 mins

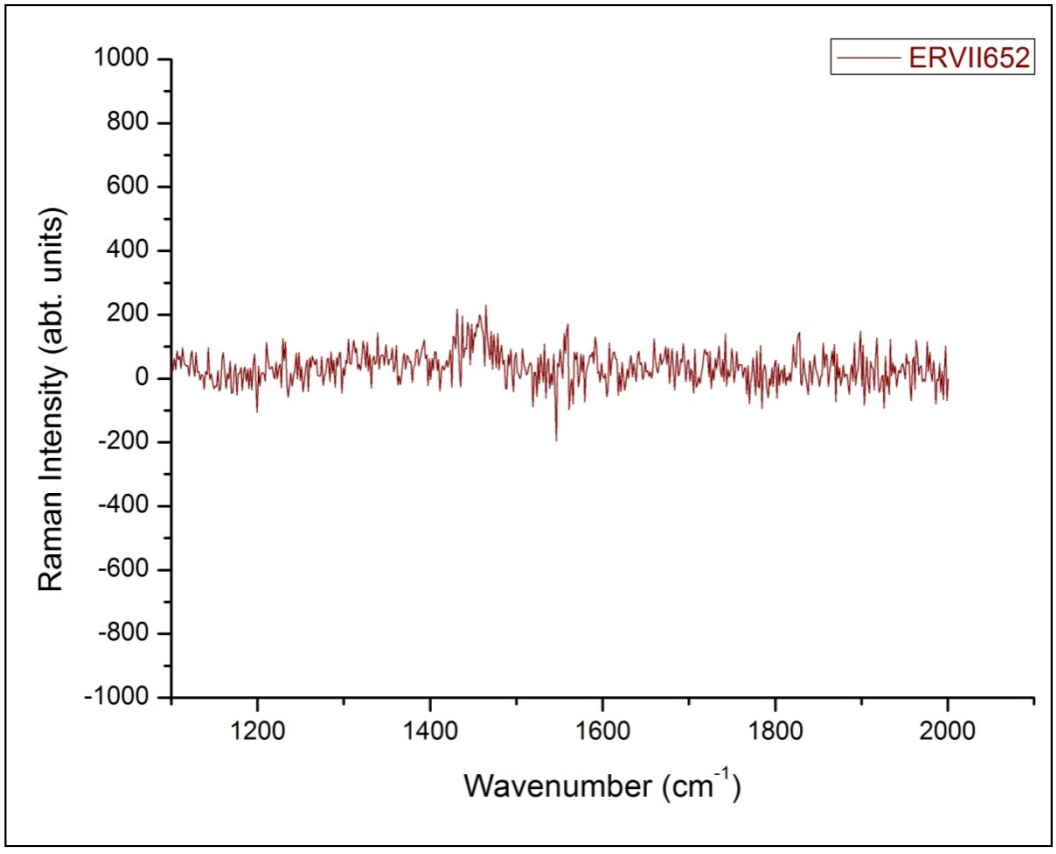

Figure 8. 16: Raman spectrum of sample ERVII652. No peaks are discernable.

The Raman spectrum for sample ERVI652 displays no peaks (Figure 8.16). This is the same result acquired when analysing a nanodiamond seeing layer using Raman spectroscopy, which is known to be too thin to obtain a Raman signal from. Graph 8.11 shows that the maximum SEE yield is **2.25 at 400–500 eV**. This value is similar to that of an untreated nanodiamond layer (sample 1) suggesting these treatment parameters, notably a short treatment time of 5 minutes at a high pressure and power, did not enhance the nanodiamond network.

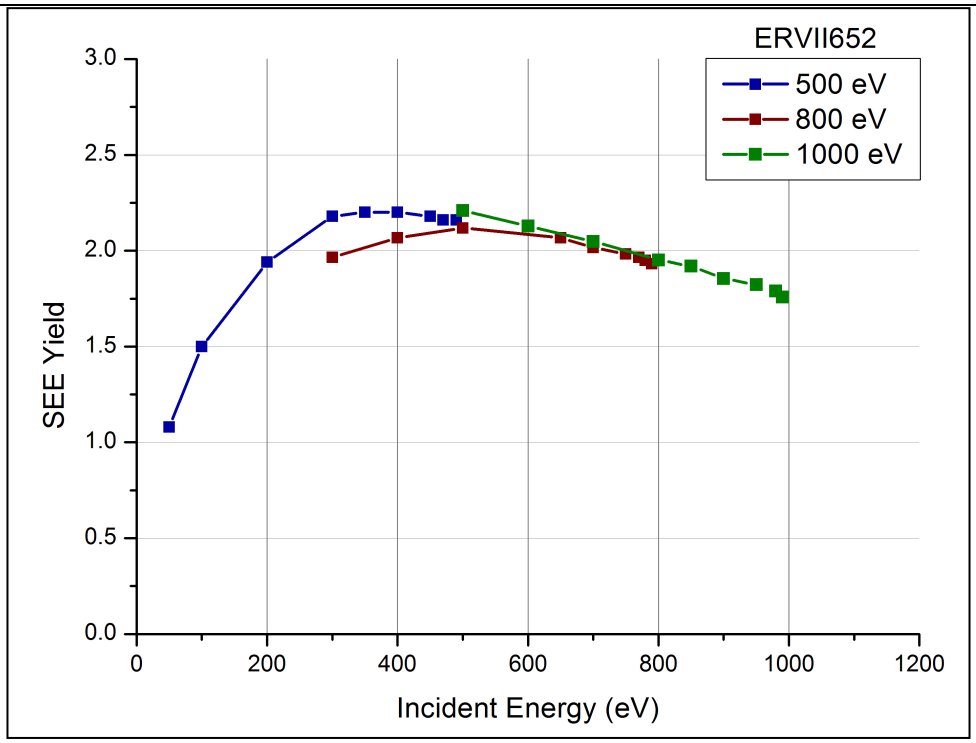

Graph 8.11: SEE yield curve for sample ERVII652 for electron beam energies, 500 eV, 800 eV and 1000 eV. The maximum SEE yield of 2.2 occurs at 350 eV.

8.6.3 Discussion

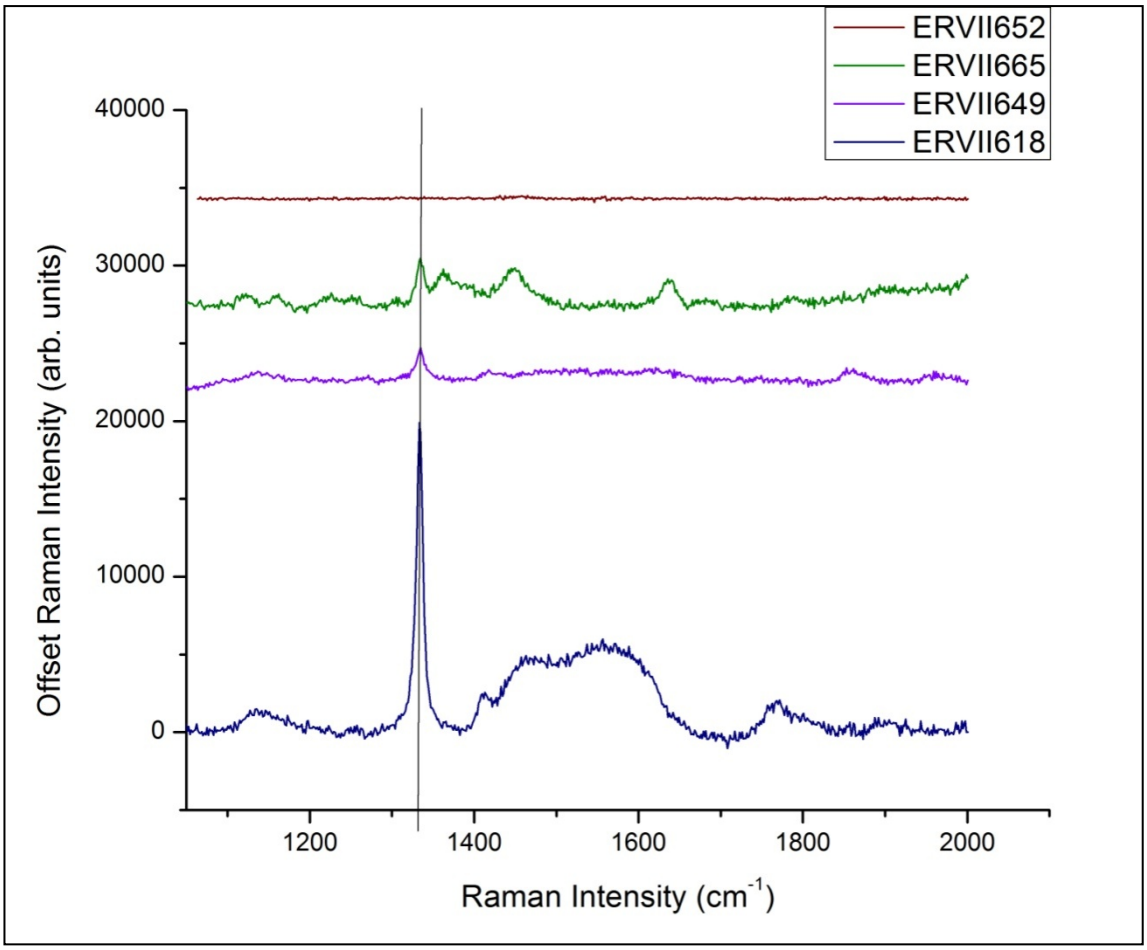

Figure 8.17: Raman spectra, with background correction for all ERVIIxyz samples.

The Raman spectra have been normalised to remove the sloping background due to photoluminescence, thus allowing for the fitting of peaks. Figure 8.17 displays the Raman spectra of all four samples for comparison. The diamond peaks are all centred at 1332 cm^{-1}. The Raman spectrum of sample ERVII618 (Figure 8.10) displays a sharp diamond peak but also the presence of a poorly defined peak at approximately 1560 cm^{-1} due to the 'G'-band emission. The 'G' peak is due to the bond stretching of all pairs of sp^2 atoms in both rings and chains. The peaks at 1140 cm^{-1} and 1470 cm^{-1} are due to transpolyacetalene in the grain boundaries; a fingerprint of nanocrystalline diamond. [8.11]

Samples ERVII649 and ERVII665 have very similar growth conditions, the notable differences being the small difference in the methane concentration (0.5% versus

0.33%) and the temperature (440 °C versus 510 °C). From the Raman spectra (Figure 8.13 and Figure 8.15) it can observed that sample ERVII649 has slightly better film characteristics. Both samples have similar diamond peaks at 1332 cm^{-1} and the presence of the transpolyacetalene peaks. However, while ERVII649 has a poorly defined peak at approximately 1560 cm^{-1} due to the 'G'-band emission, this peak is notably absent in the spectrum for ERVII665. Instead, we observe the presence of a peak at 1636 cm^{-1}; assigned to dumbbell defect of an isolated sp^2 bonded pair of carbon atoms.[8.12] In addition to this, the peak at 1363 cm^{-1} is attributed to the 'D'-band of amorphous carbon.

The Raman spectrum of sample ERVII652 has no discernable peaks and it was not possible to obtain a SEM image. This is consistent with the analysis of a monolayer of deposited nanodiamonds, suggesting that there has been no change to the seeding layer of particles.

Sample ERVII649 has presented with the maximum secondary electron yield of **8.5**, shown in graph 8.9. Followed by sample ERVII665 with a SEE yield of **7.9** and ERVII618 with a SEY of **7**. The "better quality" nanocrystalline film is actually a poorer electron emitter. An important factor in electron emission processes, besides the surface barrier is the electron supply to the surface. Accumulation of positive charge at the upper layer of the emitting sample may slow down the secondary electrons, or even prevent their escape to the vacuum. Previous work has shown experimentally that more conductive diamond films also show much better electron emission properties.[8.13, 8.14]

Higher methane concentrations and lower power density regimes drive the re-nucleation rate, decreasing the crystallite sizes and increasing the surface to volume fraction of the films.[8.15] The grain boundary concentration rises considerably resulting in significantly enhanced sp^2 concentrations. The increase in surface to volume fraction also increases the hydrogen content of the film as it is predominantly located at the grain boundaries. We can observe this comparing the Raman spectrum of ERVII618 (low methane, higher power density) with the spectrum for ERVII649 and ERVII665 (higher methane concentration, lower power density). The SEM images for the samples also show the variation in crystallite sizes. Comparing the Raman spectra of ERVII618 and ERVII649 there is

a decreasing sp^2 relative content with increasing film thickness (according to the 1550 cm^{-1} peak appearance). However, the quality of both films is high because they exhibit a defined diamond peak. Additionally, the type of sp^2 bonding in the films seems to factor in the electron emission properties. Although samples ERVII649 and ERVII665 both have good secondary electron yields, the value is higher for ERVII649 which shows the presence of crystalline sp^2 bonding, opposed to the amorphous carbon of ERVII665, indicating that the type of non-diamond carbon present is important.

The secondary electron yield curves follow what is described as the 'universal curve', i.e., one hump with a monotonic increase (decrease) before (after) the hump. The SEE yield increases as a function of E_p at low primary energy, as more secondary electrons can be excited with increasing beam energy. At a certain beam energy the penetration depth of the primary electrons becomes higher than the escape depth of the secondaries, resulting in a decrease of the SEE yield.

Trucchi *el al*.[8.16] investigated the SEE yield from polycrystalline diamond samples. These samples were grown on p-doped silicon substrates at a temperature of 770 °C and using a $\{CH_4\}/\{H_2\}$ concentration ratio of 0.5%. Samples were produced with the same experimental conditions at increasing times in order to differentiate for the film thickness. The authors found an increase in the SEE yield from 7 to 10 for samples from 2 μm to 15.6 μm, followed by a decrease in the SEE yield for thicker samples. The results of the current sample set has shown that it is possible to obtain similar values to bulk diamond films from nanocrystalline diamond films, grown at lower temperature, with thicknesses in the range of a few hundred nanometers.

Sample ERVII649 presented with the best secondary electron yield in its as-received hydrogen terminated state**: δ = 8.5 at 770 eV**. It was therefore the sample of choice for deposition of a monolayer of caesium. The sample was first treated with ozone using the method described in chapter 7. The SEE yield data was collected by the collaborators of this project. Graph 8.10 displays the acquired data with the sample having a maximum SEE yield of **17 at 1600 eV**. This figure is

almost double that obtained from the hydrogen terminated state which is in good agreement with the literature.

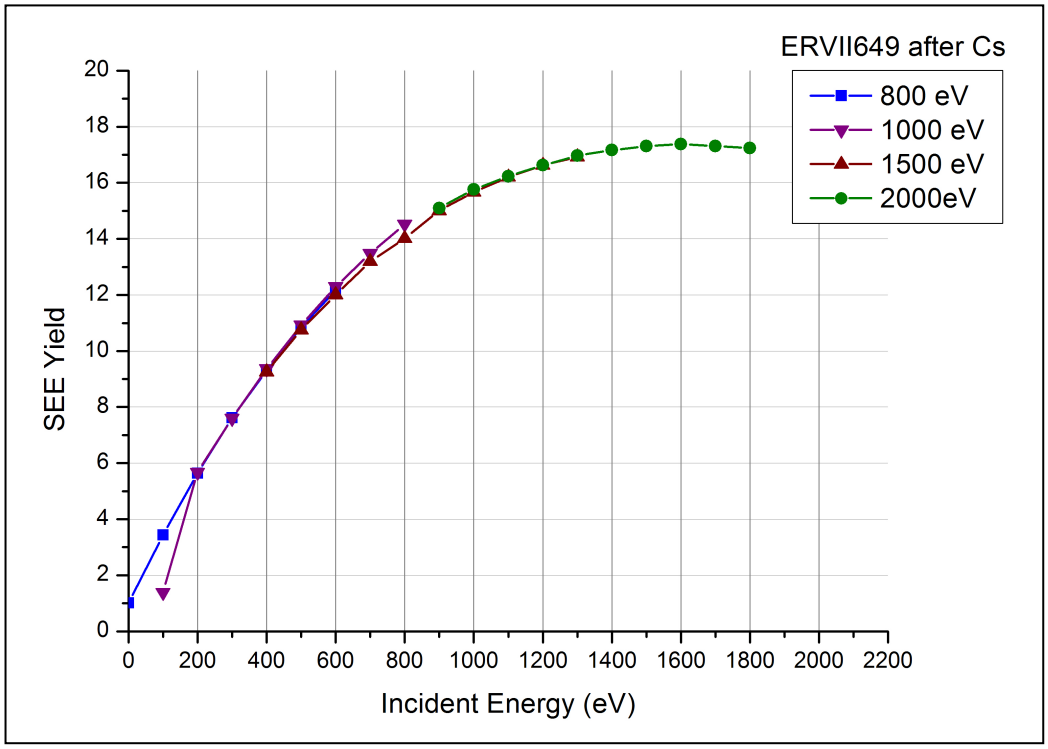

Graph 8.12: SEE yield curve for sample ERVII649 after Caesium deposition for electron beam energies, 800 eV, 1000 eV, 1500 eV and 2000 eV. The maximum SEE yield of 2.2 occurs at 350 eV.

8.7 Low temperature CVD processing of nanodiamond layers

The previous sample set has shown that thin film nanocrystalline diamond grown by a CVD process, with no further treatment produces material with secondary electron yield values much higher than the current technology or materials under investigation (i.e. Al_2O_3, MgO). An enhanced NEA surface via caesium metallisation of the diamond surface almost doubles this initial value from the hydrogen terminated surface.

To process the microchannel plate in this same way requires adjustment of the process; lowering of the operating temperatures. The MCP cannot withstand temperatures higher than 400 °C without warping of its structure. To establish whether successful low temperature processing is possible, the treatments were initially investigated using silicon wafers rather than MCPs.

8.7.1 Sample preparation

1 inch conductive (n-type arsenic doped 0.01ohmcm) silicon wafers were selected as the substrate material. A conductive substrate material is required for the secondary electron yield measurements as the current is measured through the back of the sample. The wafers were "seeded" with nanodiamond particles as described in chapter 5 using a colloid concentration of 0.5g/L to produce, evenly dispersed, tightly packed layers 'monolayers'.

8.7.2 CVD Processing

The samples in this section were treated in a CVD reactor at the UCL Diamond Electronics laboratory. The CVD reactor used to process these samples is by Seki Technotron. This reactor is much smaller than the reactor used to produce the ERVIIXYZ sample set, allowing a maximum wafer size of 1". The maximum power output of the power supply is limited to 1500 W. The substrate holder was modified to allow cooling by connection to a water cooling unit thereby allowing the plasma to be maintained at a substrate temperature of no more than 400 °C.
Deposition from a hydrogen-rich plasma environment ensured hydrogen coverage of the sample surface. The treatment conditions for each of the four treated samples are listed in the following results section. The treatment conditions for each sample are followed by the SEM images and Raman spectra obtained. The Raman spectra were obtained using a 514 nm wavelength. Finally, the secondary electron yield curves, obtained using the method described at the beginning of this chapter are displayed.

8.7.3 Results and Discussion

Sample UCL (a)

Substrate: 1" Si; 500µm thickness

H_2 190 sccm ; CH_4 10 sccm (5% methane)

Power: 450 W

Process Pressure: 13.0 torr

Temperature: 400°C

Treatment Time: 3 hours

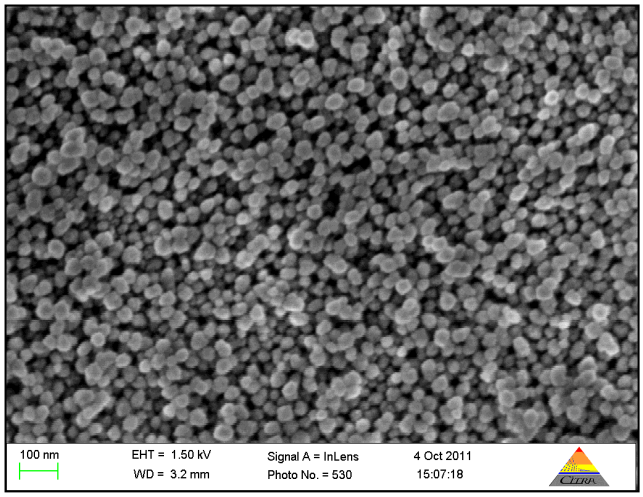

Figure 8.18: SEM image of Sample UCL (a) after processing. This image was taken at the edge of the sample.

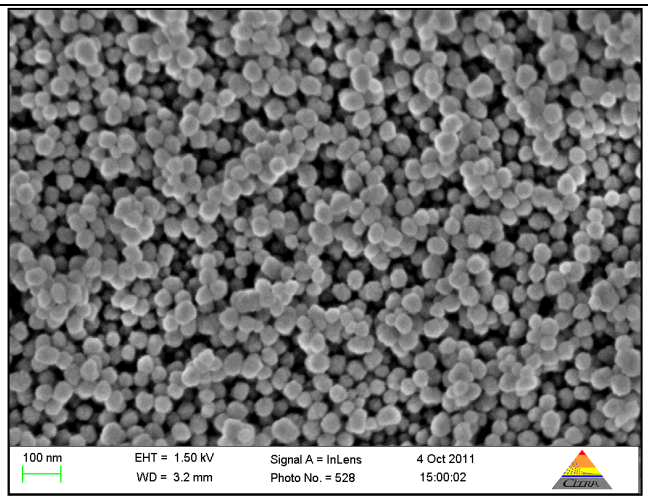

Figure 8.19: SEM image of Sample UCL (a) after processing. This image was taken at the centre of the sample.

Sample UCL (a) was treated with 5 % methane concentration in the gas mixture, for a duration of 3 hours. The plasma power and pressure were adjusted throughout to maintain a temperature of approximately 400 °C. Figures 8.18 and 8.19 display the SEM images obtained from the edge and centre of the 1" wafer post processing. The morphology of the film is still particle-like, with a crystalline structure not visible. There is a clear difference in the size of the particles at the edge and centre. Since the plasma size was small (less than approximately 2" diameter) it can be expected that the sample would not experience equal conditions.

Figure 8.20 shows the Raman spectrum obtained from the centre of sample UCL (a). A reasonably sharp but broadened diamond peak is visible at 1331 cm^{-1}. Comparing this to the Raman spectrum of untreated nanodiamonds (Figure 5.10) the diamond peak is only red-shifted by 1 wavenumber which is expected since the post treatment particles are much larger in size. The broad peak that appears to be centred around 1170 cm^{-1} is most likely due to transpolyacetylene in the film. The broad peak from 1400 – 1650 cm^{-1} is the product of any possible number of peaks, which would require deconvolution to establish. A peak at 1450cm^{-1} would be due to transpolyactylene. The 1520- 1580 cm^{-1} is attributed to the 'G' peak of sp^2 amorphous carbon. It is clear that this layer contains a substantial amount of non-diamond carbon.

Graph 8.13 shows the obtained SEE yield curves (absolute values) against incident beam energy from 0 eV to 1000 eV. SEE yield curves were obtained for three electron beam energies (500, 800, and 1000 eV). The curves for each energy were obtained by varying the sample bias at intervals from -50 to -500 V, thereby changing the incident energy at which the electrons impinge on the sample surface. The curves do not match exactly for the reasons explained earlier in this chapter. The SEE yield increases with increasing incident energy, as more secondary electrons can be excited, to a maximum of **5.5 at 650 eV**.

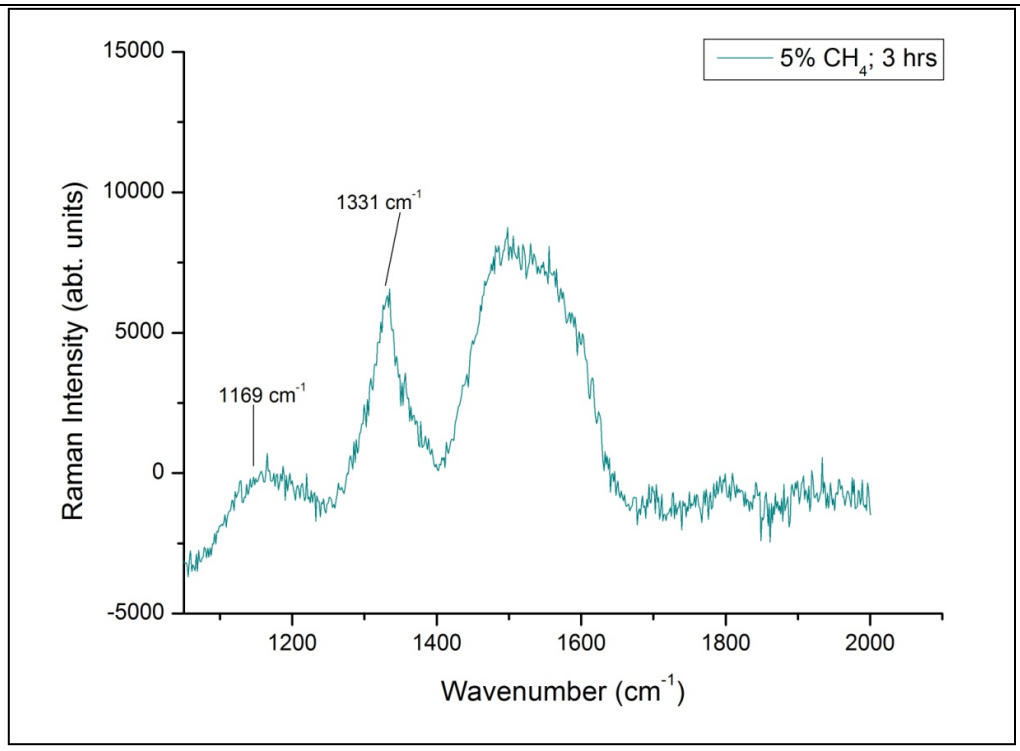

Figure 8.20: Raman spectrum of Sample UCL (a) with assigned peaks.

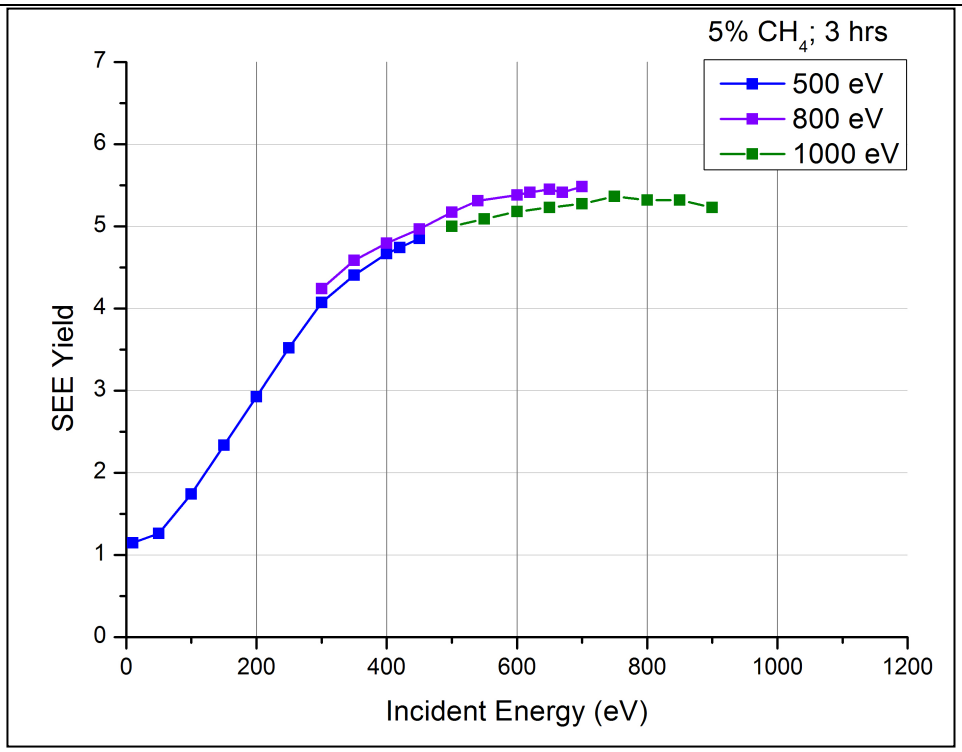

Graph 8.13: SEE yield curves for Sample UCL (a) for electron beam energies, 500eV, 800eV and 1000eV.

Sample UCL (b)

Substrate: 1" Si; 500µm thickness

H_2 190 sccm ; CH_4 10 sccm (5% methane)

Power: 400 – 450 W

Process Pressure: 13.0 torr

Temperature: 400 °C

Treatment Time: 4.5 hours

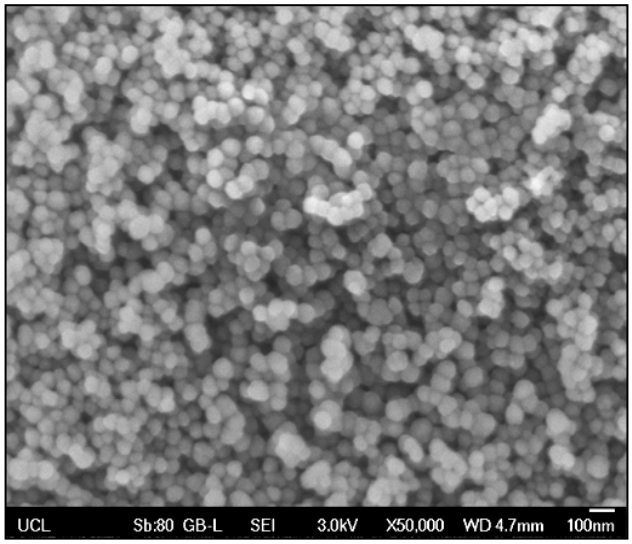

Figure 8.21: SEM image of Sample UCL (b) after processing. This image was taken at the edge of the sample.

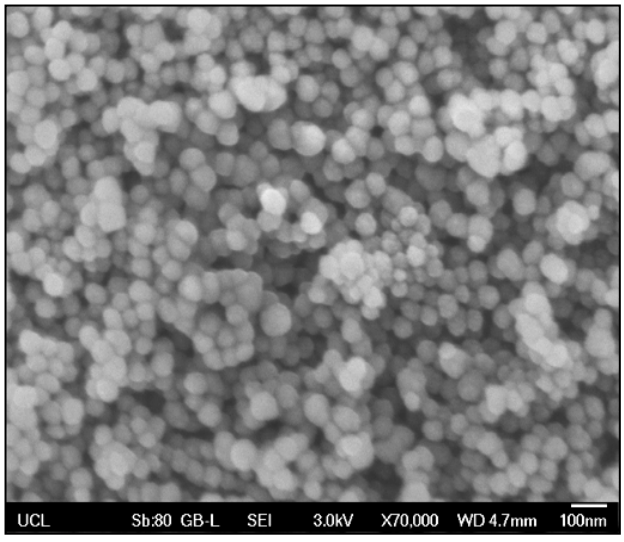

Figure 8.22: SEM image of Sample UCL (b) after processing. This image was taken at the centre of the sample.

Sample UCL (b) was treated with 5 % methane concentration in the gas mixture, for a duration of 4.5 hours. The plasma power and pressure were adjusted throughout to maintain a temperature of approximately 400 °C. Figures 8.21 and 8.22 display the SEM images obtained from the edge and centre of the 1" wafer post processing. The morphology of the film is still particle-like, with a crystalline structure not visible. The sample displays the same difference in particle size between the edge and centre of the wafer as with sample UCL (a). However, the particles do appear slightly bigger than in the SEM images of sample UCL (a). The particles at the centre of the wafer are approximately 80 nm in diameter.
Figure 8.23 shows the Raman spectrum obtained from the centre of sample UCL (b), which is almost identical to sample UCL (a). A reasonably sharp but broadened diamond peak is visible at 1331 cm^{-1}. The origin of the two broader peaks has been discussed for the spectrum of sample UCL (a).

Graph 8.14 shows the obtained SEE yield curves (absolute values) against incident beam energy from 0 eV to 1500 eV. SEE yield curves were obtained for four electron beam energies (500, 800, 1100 and 1500 eV). The curves for each energy were obtained by varying the sample bias at intervals from -50 to -500 V, thereby changing the incident energy at which the electrons impinge on the sample surface. The curves do not match exactly for the reasons explained earlier in this chapter. The SEE yield increases with increasing incident energy, as more secondary electrons can be excited, to a maximum of **5.5 at 650 – 800 eV**. This is the same value as obtained for sample UCL (a).

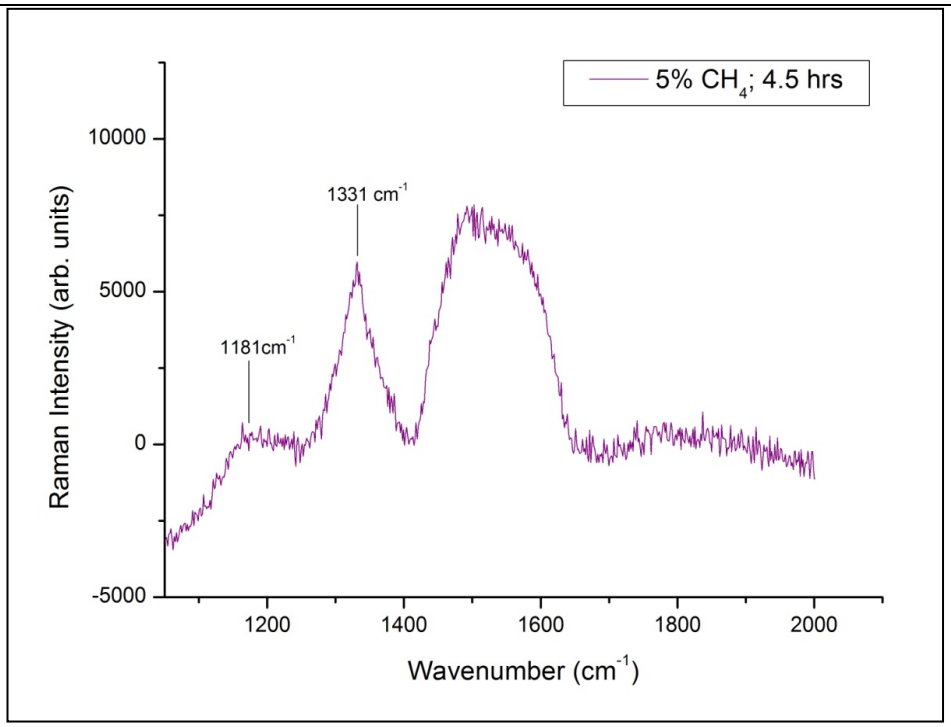

Figure 8.23: Raman spectrum of Sample UCL(b) with assigned peaks.

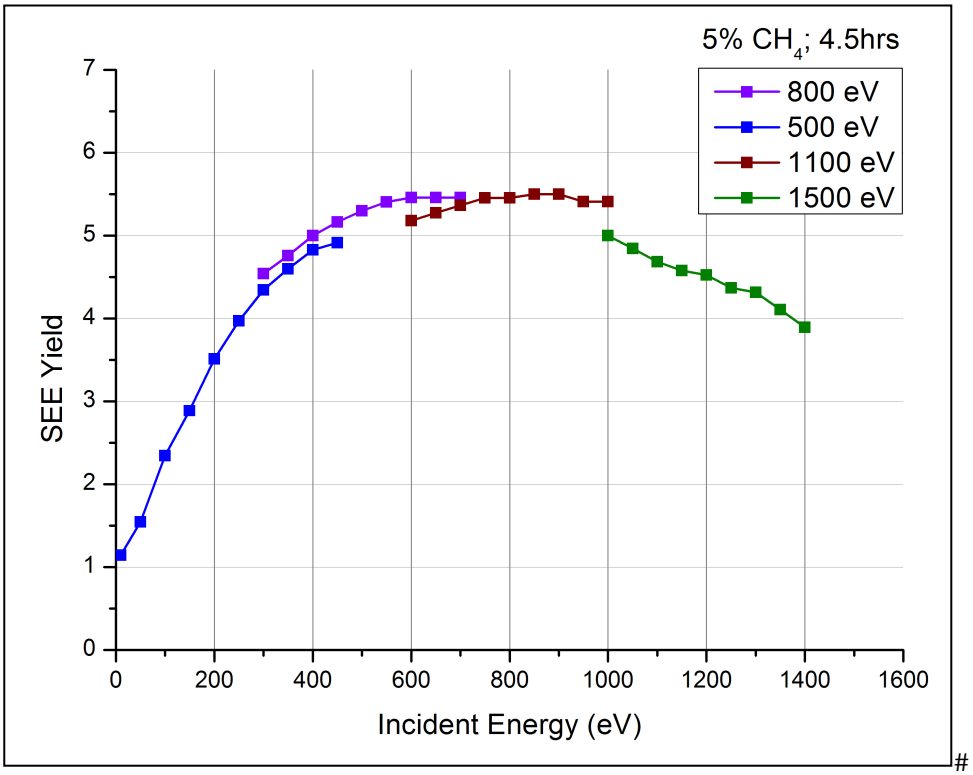

Graph 8.14: SEE yield curves for Sample UCL (b) for electron beam energies, 500eV, 800eV, 1100eV and 1500 eV.

Sample 1(c)

Substrate: 1" Si 500µm

H_2 133 sccm ; CH_4 10 sccm (7.5% methane)

Power: W

Process Pressure: mbar

Temperature: 400°C

Treatment Time: 3 hours

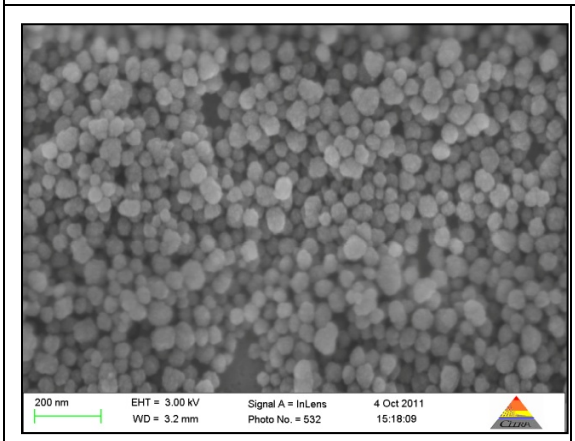

Figure 8.24: SEM image of Sample UCL (c) after processing. This image was taken at the edge of the sample.

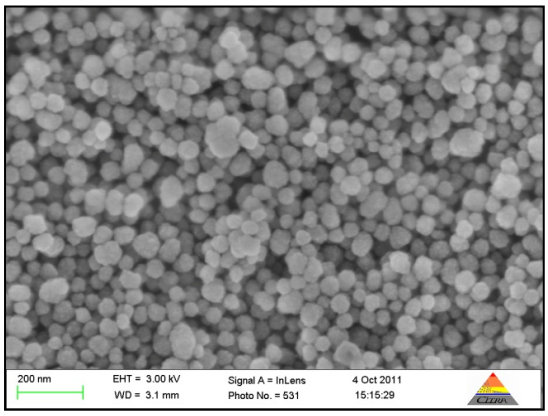

Figure 8.25: SEM image of Sample UCL (c) after processing. This image was taken at the edge of the sample.

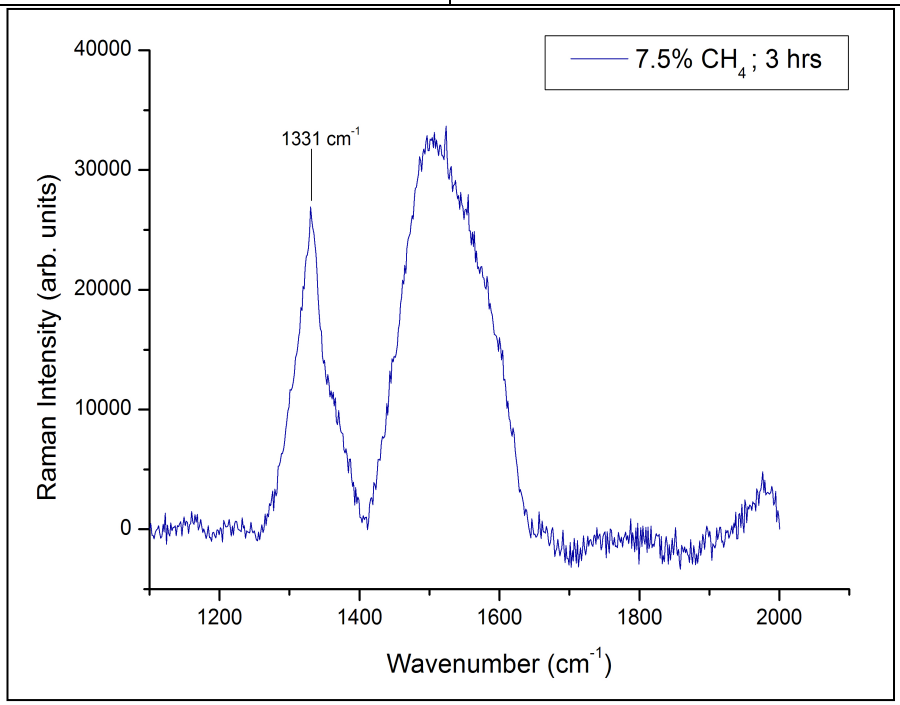

Figure 8.26: Raman spectrum of Sample UCL (c) with assigned peaks.

Sample UCL (c) was treated with 7.5 % methane concentration in the gas mixture, for a duration of 3 hours. The plasma power and pressure were adjusted throughout to maintain a temperature of approximately 400 °C. Figures 8.24 and 8.25 display the SEM images obtained from the edge and centre of the 1" wafer post processing. The morphology of the film is still particle-like, with a crystalline structure not visible. The sample displays the same difference in particle size between the edge and centre of the wafer as with sample UCL (a) and (b). However, the particles do appear slightly bigger than in the SEM images of sample UCL (a). The particles at the centre of the wafer are approximately 80 nm in diameter.

Figure 8.26 shows the Raman spectrum obtained from the centre of sample UCL (c). This spectrum is slightly different compared to sample UCL (a) and UCL (b). A reasonably sharp but broadened diamond peak is visible at 1331 cm^{-1}. The origin of the two broader peaks has been discussed for the spectrum of sample UCL (a). However, the broad peak at approximately 1170cm^{-1} is absent from the spectrum. A higher methane concentration results in a greater renucleation, which could explain the lower concentration of transpolyactylene at this point in the process. The broad peak between 1400 – 1650 cm^{-1} appears to be slightly sharper than that of the preacious two samples. However, it can be expected it is as a result of the same 'D' and 'G' peaks of sp^2 amorphous carbon.

Graph 8.15 shows the obtained SEE yield curves (absolute values) against incident beam energy from 0 eV to 1000 eV. SEE yield curves were obtained for three electron beam energies (500, 800, and 1000 eV). The curves for each energy were obtained by varying the sample bias at intervals from -50 to -500 V, thereby changing the incident energy at which the electrons impinge on the sample surface. The curves do not match exactly for the reasons explained earlier in this chapter. The SEE yield increases with increasing incident energy, as more secondary electrons can be excited, to a maximum of **5.5 – 6.0 at 650 – 800 eV**.

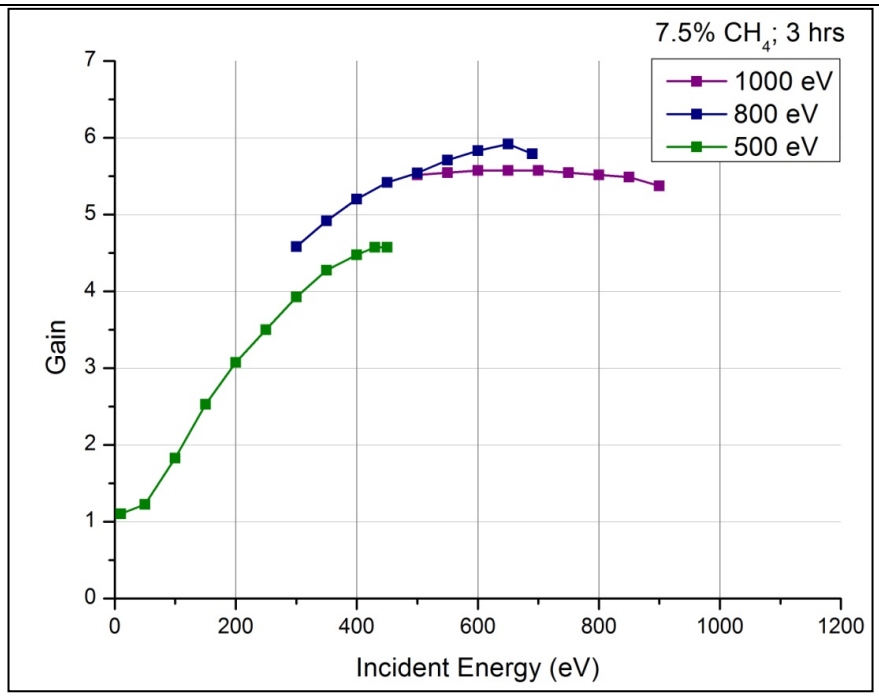

Graph 8.15: SEE yield curves for Sample 1(a) for electron beam energies, 500eV, 800eV, and 1000 eV.

The critical temperature of 400 °C meant that is was not possible to increase the power and pressure of the plasma which limited the samples in this investigation.† The only variables were the methane concentration and the treatment time. A 2.5% increase in methane concentration (sample UCL (c)) is quite significant given that NCD is typically grown with less than 1 % of methane in the growth gas mixture. Below 5 % (sample UCL (a) and UCL (b)) and it is unlikely that a change would have occurred to the seeding layer given the low power densities which were employed. Since an increase from 3 hours to 4.5 hours did not change the composition or structure of the film, a further increase in treatment time was not investigated. Nevertheless the results obtained from this sample set are extremely promising in showing that low temperature CVD processing of nanodiamond seeding layers can produce a network of particles with good secondary electron emission yield characteristics, similar to those obtained from continuous, crystalline films (ERVII sample set). The SEE yield values are double that obtained from an untreated nanodiamond layer (2.5 at 450 eV; sample 1 (control)), indicating a substantial improvement to the structure. Since the conditions being

† Improved cooling would allow for better plasma conditions.

used are insufficient for significant diamond significant diamond growth, as shown by the SEM and Raman analysis, this is clearly attributable to an improvement in the diamond crystalline quality of the (still) ND particles. Consistently good SEE yields have been obtained that exceed those of other materials currently under investigation.

8.8 Concluding remarks

The work described in this chapter has led to the development of processes fully compatible with existing MCP technology used within night vision devices. The development of low temperature plasma methods for the formation of continuous CVD diamond films from ND films (section 8.6) can be considered important. However, it is the realisation of a low temperature process at lower powers and time durations (section 8.7) that effectively turns 'poor' NDs into 'high quality' NDs that can be considered a major step towards realising improved MCPs for this application. This process can be improved by the use of a larger reactor combined with more aggressive cooling. This would allow for a higher power density plasma at 400 °C, with which it should be possible further improve the SEE characteristics of the layers. The next step would then be to replicate this process on a microchannel plate with an aim to create a layer on the top surface and in the top of the channel walls to a depth of a few diameters. The reasoning for this is explained in chapter 3; to insure that first interaction events are not lost to the device. Processing a microchannel plate presents with additional complications. Not only must the temperature not exceed 400 °C but a method of 'back-pumping' must be employed whereby the MCP channels are pumped from the backside of the plate to avoid gas becoming trapped in the channels, causing a build up of carbon. The equipment is undergoing modification to achieve this.Preliminary experiments have been conducted and at the time of writing technology transfer is occurring between the UCL team and Photonis SAS, such that the processes developed in this chapter can be applied to MCPs for device trials in the night vision goggles during summer 2012.

References

8.1 F. Pruvost and A. Deneuville, *Diamond and Related. Materials,* Vol. 10, 531 (2001)

8.2 A. Shih, J. Yater, P. Pehrsson, J. Butler, C. Hor, and R. Abrams, *Journal of Applied Physics*, 82, 1860 (1997).

8.3 J. Yater and A. Shih, *Journal of Applied Physics,* 3057 (2001).

8.4 H.J. Hopman, J. Verhoeven, P.K. Bachmann, *Diamond and Related Materials*, 9 (3-6): 1238. (2000).

8.5 C. Goeden, G. Dollinger, *Applied Physics Letters*, 81 (26):5027 (2002).

8.6 J-C. Arnault, T. Petit, H. Girard, A. Chavanne, C. Gesset, M. Sennourb, M. Chaigneauc, *Phys. Chem. Chem. Phys.* Advanced Online Publication DOI:10.1039/c1cp20109c

8.7 K.P. Loh, J. S. Foord, R. G. Egdell, and R. B. Jackman, *Diamond and Related Materials,* 6, 874 (1997).

8.8 M. Geis, J. Twichell, J. Macaulay, and K. Okano, *Applied Physics Letters*, 67, 1328 (1995).

8.9 J. E. Yater and A. Shih, *Journal of Applied Physics*. **87**, 8103 (2000)

8.10 M. Funer, C. Wild, P. Koidl, *Applied Physics Letters*. 72 (10):1149 (1998).

8.11 A. C. Ferrari and J. Robertson, *Physical Review B*, 63, 121405 (2001)

8.12 S. Prawer, K.W. Nugent, D.N. Jamieson, J.O. Orwa, L.A. Bursill, J.L. Peng, *Chemical Physics Letters Volume*, 32 (1-2): 93 (2000)

8.13 A. Shih, J. Yater, P. Pehrsson, J. Butler, C. Hor, and R. Abrams, *Journal of Applied Physics*, 82, 1860 (1997).

8.14 Y.D Kim, W Choi, H Wakimoto, S Usami, H Tomokage, T Ando, *Diamond and Related Materials*, 9 (3-6): 1096 (2000).

8.15 O.A. Williams, A. Kriele, J. Hees, M. Wolfer, W. Müller-Sebert, C.E. Nebel, *Chemical Physics Letters,* 495 (1-3): 84-89 (2010).

8.16 D.M. Trucchi, C. Scilletta, E. Cappelli, P.G. Merli, S. Zoffoli, G. Mattei, P. Ascarelli, *Diamond and Related Materials*, 15, (4):827 (2006).

Conclusion

Research on the topic of nanodiamond has increased rapidly in the past five years. However, the majority of the published literature has been in the areas of post-detonation processing, chemical functionalisation for biological applications and applications in nanocomposites. The research in the realm of electronics has been fairly limited, with the most common use of nanodiamonds being their use as seeds for thin film diamond growth. This thesis has investigated fundamental aspects of nanodiamonds for their applicability in electronic applications. Important topics such as deposition, electrical characteristics and surface modifications of detonation nanodiamonds have been addressed in this thesis for the realisation of a high secondary electron emission nanodiamond material, outperforming both the current technology and other research materials.

Chapter 5

A protocol for the deposition of a densely packed monolayer of ~5nm nanodiamonds has been developed. Substrate choice and the surface condition of the NDs used (chapter 7) mean that attractive zeta potentials lead to a well-adhered layer, in terms of routine laboratory handling. This is a promising result for the potential use of this form of ND in applications where a thin diamond coating on a 2- or 3-D non-diamond substrate would be advantageous. The fact that they can be deposited from a water-based solution at room temperature using a simple sonication process means that a wide range of substrates can be employed, including those comprising materials that would not be resilient within a standard thin film diamond growth system, which typically operates at 850 °C with a high partial pressure of (chemically active) atomic hydrogen.[9.1] Such materials could include glass and plastics. These results have already been utilised by the UCL diamond electronics group to produce a nanodiamond-coated silicon cantilever array for chemical sensing.[9.2]

The use of Raman spectroscopy has led to the conclusion that the ND particles are indeed crystalline diamond, with little sp^2 content within a densely packed (multilayer) sample. This observation means that these particles can indeed be

explored for diamond coating applications, without re-course to conventional thin film diamond growth procedures.

Chapter 6

The electrical properties of a "monolayer" of nanodiamonds has been studied; a resistivity of the order of 10^{12} Ω/sq has been determined, with only one significant conduction pathway being observed. This suggests either the nanodiamonds support little in the way of sp^2-like material on their surfaces, or any such material is electrically inactive, presumably through depletion. The dielectric character of the detonation nanodiamond particles is also good, with dielectric loss tangent values in the range 0.05 – 0.5 being recorded. These combined observations suggest DNDs behave in electrical terms similar to thin film diamond, and that electrical applications for DNDs are worthy of pursuit. Since the simple room temperature sonication process used here is capable of coating a wide-range of three-dimensional objects with DND layers this is an exciting result. A limitation on the electrical use the monodispersed DNDs, at least in the untreated, as-deposited from solution form used here, is the catastrophic loss of diamond like character at temperatures above 400 °C.

Chapter 7

It has been found that annealing the nanodiamond layers hydrogenates the surface by removing oxygen containing groups and replacing them with hydrogen terminations. The Ozone treatment devised following hydrogenation is successful in removing the hydrogen terminations and replacing them with oxygen containing groups, more so than ozone treating nanodiamonds directly. Additionally the ozone treatment post-hydrogenation displays the presence of more of the important ketone groups. An efficient protocol for the oxidation of nanodiamond surfaces has been established, which is faster and simpler than the methods reported in the literature and also suitable to perform after deposition on to a substrate.

Chapter 8

The work described in this chapter has led to the development of processes fully compatible with existing MCP technology used within night vision devices. The development of low temperature plasma methods for the formation of continuous CVD diamond films from ND films (section 8.6) can be considered important. However, it is the realisation of a low temperature process at lower powers and time durations (section 8.7) that effectively turns 'poor' NDs into 'high quality' NDs that can be considered a major step towards realising improved MCPs for this application.

There are currently two important areas of further research. The first is to investigate the use of lithium as a replacement for metallisation. Lithium is reported to exhibit a large work-function shift relative to a clean diamond surface an effect similar to that seen for Cs-O on diamond, but with a higher binding energy of 4.7 eV per Li atom,[9.3] which would produce a higher stability NEA surface than caesium. The second area, in which research has already commenced, is the use of single crystal diamond (SCD) as a replacement for the MCP. High transmission yields have been measured from SCD[9.4] and thin (5 – 10 μm) plates are now commercially available on request. If the yields can be improved, through the mechanism of photoconductive gain, the potential applications in image intensifiers and electron amplification devices would be significant.

References

9.1 O.A. Williams, M. Nesladek, M. Daenen, S. Michaelson, A. Hoffman, E. Osawa, K. Haenen, R.B. Jackman, *Diamond and Related Materials*, 17: 1080 (2008).

9.2 R.K. Ahmad, A.C. and Parada, S. Hudziak, A. Chaudhary, and R.B Jackman, *Applied Physics Letters*, 97 (9): 093103 (2010).

9.3 K. M. O'Donnell, T. L. Martin, N. A. Fox, and D. Cherns, *Physical Review B*, 82, 115303 (2010).

9.4 J.E. Yater, J.L. Shaw, K.L. Jensen, T. Feygelson, R.E. Myers, B.B. Pate, J.E. Butler, *Diamond and Related Materials*, 20, (5):798-802 (2011)

Publications

R.K. Ahmad, A.C. and Parada, S. Hudziak, A. Chaudhary, and R.B Jackman, (2010) Nanodiamond-coated silicon cantilever array for chemical sensing. **APPL PHYS LETT**, 97 (9), Article 093103

A. Chaudhary, J.O. Welch, and R.B. Jackman, (2010) Electrical properties of monodispersed detonation nanodiamonds. **APPL PHYS LETT**, 96 (24), Article 242903.

M. Bevilacqua, A. Chaudhary, and R.B. Jackman, (2009) The influence of ammonia on the electrical properties of detonation nanodiamond. **J APPL PHYS**, 106 (12), Article 123704.

M. Bevilacqua, S. Patel, A. Chaudhary, H.T. Ye, and R.B. Jackman, (2008) Electrical properties of aggregated detonation nanodiamonds. **APPL PHYS LETT**, 93 (13) , Article 132115.

M. Bevilacqua, N. Tumilty, A. Chaudhary, H.T. Ye, J.E. Butler, and R.B. Jackman, (2008) Nanocrystalline diamond as a dielectric for SOD applications. In: Nebel, CE and Jackman, RB and Nemanich, RJ and Nesladek, M, (eds.) **DIAMOND ELECTRONICS - FUNDAMENTALS TO APPLICATIONS II.** (pp. 235 - 246). Materials Research Society.

List of Figures

Appendices

Appendix 1: Photonis SAS. MCP specification sheet

Appendix 2: List of Abbreviations

DND: *Detonation nanodiamond*

ND: *Nanodiamond*

CVD: *Chemical Vapour Depostion*

HPHT: *High pressure high temperature*

NMR: *Nuclear magnetic resonance*

TPD: *Temperature programmed desorption*

XPS: *X-ray photoelectron spectroscopy*

RIE: *Reactive Ion Etching*

MCP: *Microchannel Plate*

NEA: *Negative Electron Affinity*

SEE: *Secondary electron emission*